Thermoelectric properties of oxide heterostructures

Von der Fakultät Chemie der Universität Stuttgart
zur Erlangung der Würde eines
Doktors der Naturwissenschaften (Dr. rer. nat.)
genehmigte Abhandlung

Vorgelegt von

Stefan Heinze

aus Esslingen

Hauptberichter: Prof. Dr. B. Keimer
Mitberichter: Prof. Dr. Ir. E.J. Mittemeijer
Mitprüfer: Prof. Dr. F. Gießelmann

Tag der mündlichen Prüfung: 11. September 2013

Max-Planck-Institut für Festkörperforschung, Stuttgart
Universität Stuttgart
Stuttgart 2013

Dedicated to my wife Sandra

Content

6

Abstract (English)

The thermoelectric properties and the electrical conductivity of thin films of the high temperature superconductor $YBa_2Cu_3O_{7-\delta}$ and the ferromagnet/paramagnet $La_{2/3}Ca_{1/3}MnO_3$ as well as heterostructures and superlattices of both materials were investigated in this thesis. Since the properties of $YBa_2Cu_3O_{7-\delta}$ and $La_{2/3}Ca_{1/3}MnO_3$ are antagonistic, the simultaneous occurrence of both properties in heterostructures and superlattices and the mutual interactions between both materials are in the focus of interest. The investigations should gain insight into the nature of these interactions and can be seen complementary to the investigations using Hall coefficient and normal resistivity measurements. Also, the studies should lead to information about the properties of the interface between both materials.

The thin films used in this thesis exhibit mainly a total thickness of 2000 Å. They were grown on different substrates ($SrTiO_3$, $(La_{0.27}Sr_{0.73})(Al_{0.65}Ta_{0.35})O_3$, $NdGaO_3$) by pulsed laser deposition (PLD) techniques and studied in different temperature ranges (20 K to 390 K or 320 K to 750 K). The concept was to investigate at first the physical properties of single layer $YBa_2Cu_3O_{7-\delta}$ and $La_{2/3}Ca_{1/3}MnO_3$. In a second step, heterostructures and superlattices of both materials, also with a total thickness of 2000 Å, were fabricated and studied. Using systems with constant total thickness, but with different thicknesses of the single layer materials in the structures and thus varying number of interfaces should lead to knowledge about the mutual influences between both materials and the properties of the interface between both materials.

The investigations of single layer $YBa_2Cu_3O_{7-\delta}$ and $La_{2/3}Ca_{1/3}MnO_3$ thin films lead to findings which were in a good agreement with the results published by different groups before. The measured Seebeck-coefficients of optimally doped $YBa_2Cu_3O_{7-\delta}$ ($\delta = 0.05$) are zero in the superconducting state and nearly zero ($S(T) = \pm 2$ μV/K) up to temperatures of 400 K. The Seebeck-coefficients determined for $La_{2/3}Ca_{1/3}MnO_3$ are nearly zero ($S(T) = \pm 2$ μV/K) in the ferromagnetic regime and negative ($S(T) = - 10$ μV/K to $- 17$ μV/K) in the paramagnetic state.

Both materials were combined in heterostructures and superlattices. The investigated Seebeck-coefficients result always in positive values between 20 K and 390 K. The findings are completely unexpected since they are strongly deviating from a theoretical combination of the physical properties of the single layer materials according to Kirchhoff's law. The calculated values are nearly matching with the Seebeck-coefficients investigated for YBCO. Finally, the findings were addressed to long range interactions nucleated at an electronic and magnetic reconstructed interface between $YBa_2Cu_3O_{7-\delta}$ and $La_{2/3}Ca_{1/3}MnO_3$. Information about the physical properties of the interface could not be gathered directly, because of its high resistivity.

Abstract (Deutsch)

Diese Arbeit befasst sich mit den thermoelektrischen Eigenschaften und der elektrische Leitfähigkeit dünner Schichten des Hochtemperatursupraleiters $YBa_2Cu_3O_{7-\delta}$ und des Ferromagneten/Paramagneten $La_{2/3}Ca_{1/3}MnO_3$ sowie Heterostrukturen und Übergitter beider Materialien. Angesichts der antagonistischen Eigenschaften beider Materialien sind das gleichzeitige Auftreten beider Eigenschaften in Heterostrukturen und Übergittern, sowie die Wechselwirkungen zwischen beiden Materialien von großem Interesse. Die Untersuchungen sollen Einblicke in die Natur der Wechselwirkungen liefern und können als komplementäre Untersuchungen zu den Messungen von Hall Koeffizienten und des elektrischen Widerstandes betrachtet werden. Ebenso sollen die Experimente Informationen über die physikalischen Eigenschaften der Grenzfläche zwischen beiden Materialien ergeben.

Die in der Arbeit untersuchten dünnen Schichten weisen überwiegend eine Dicke von 2000 Å auf. Sie wurden auf verschiedenen Substraten ($SrTiO_3$, $(La_{0,27}Sr_{0,73})(Al_{0,65}Ta_{0,35})O_3$, $NdGaO_3$) mittels Gepulster Laser Deposition (PLD) abgeschieden und in verschiedenen Temperaturbereichen (20 K bis 390 K oder 320 K bis 750 K) untersucht. Als Erstes wurden die physikalischen Eigenschaften der Einzelschichten von $YBa_2Cu_3O_{7-\delta}$ und $La_{2/3}Ca_{1/3}MnO_3$ charakterisiert. Als Zweites erfolgte die Herstellung von Heterostrukturen und Übergitter beider Materialien (Gesamtdicke ebenso 2000 Å) und deren Untersuchung. Durch die Erzeugung von Strukturen mit einer konstanten Gesamtdicke, einer variierenden Dicke der Einzelschichten in den Strukturen und somit einer variierenden Anzahl an Grenzflächen sollten Informationen über die Wechselwirkungen zwischen beiden Materialien und die Eigenschaften der Grenzflächen zwischen beiden Materialien gewonnen werden.

Die Untersuchungen der Einzelschichten von $YBa_2Cu_3O_{7-\delta}$ und $La_{2/3}Ca_{1/3}MnO_3$ führen zu Ergebnissen, die mit den Werten übereinstimmen, die von verschiedenen

Gruppen publizierten wurden. Die gemessenen Seebeck-Koeffizienten von optimal dotiertem $YBa_2Cu_3O_{7-\delta}$ ($\delta = 0.05$) sind gleich null im supraleitenden Temperaturbereich und nahezu null ($S(T) = \pm 2\,\mu V/K$) bis zu Temperaturen von 400 K. Die Seebeck-Koeffizienten, die für $La_{2/3}Ca_{1/3}MnO_3$ bestimmt wurden, sind nahezu null ($S(T) = \pm 2\,\mu V/K$) in der ferromagnetischen Phase und negativ ($S(T) = -10\,\mu V/K$ bis $-17\,\mu V/K$) im paramagnetischen Temperaturbereich.

Die bei den Heterostrukturen und Übergittern gemessen Seebeck-Koeffizienten sind in einem Temperaturbereich von 20 K bis 290 K immer positiv. Dieses Ergebnis ist überraschend, da die Messwerte sehr stark von den theoretisch berechneten Werten abweichen. Die Berechnungen wurden an Hand der physikalischen Eigenschaften der Einzelschichten nach dem Kirchhoffschen Gesetz durchgeführt und liefern nahezu identische Werte zu den bei $YBa_2Cu_3O_{7-\delta}$ Einzelschichten gemessenen Werten. Die Ursache der hohen Seebeck-Koeffizienten wurden langreichweitigen Effekten zugeschrieben, die ihren Ursprung in der Grenzfläche zwischen $YBa_2Cu_3O_{7-\delta}$ und $La_{2/3}Ca_{1/3}MnO_3$ haben. Die Grenzfläche weist elektronische und magnetische Eigenschaften auf, die sich von den Eigenschaften der Einzelschichten unterscheiden. Wegen des hohen elektrischen Widerstands der Grenzfläche war es nicht möglich, die Eigenschaften der Grenzfläche direkt aus den Messungen der Seebeck-Koeffizienten abzuleiten.

Chapter 1

Introduction and motivation

Heat emanating from natural sources such as solar or geothermal as well as waste heat from industrial processes or automotive can be converted directly into electricity by thermoelectric devices without moving parts or environmentally unhealthy emissions. Success in this field, determined by increasing efficiency of all solid thermoelectric generators, will contribute to the ecology – inspired efforts to increase the fraction of renewable energy of the total energy consumption. As an indicator of the usability of thermoelectric devices in practical applications serves the dimensionless figure of merit:

$$ZT = \frac{S^2 \sigma T}{\kappa}$$
Equation 1

with S being the thermopower (frequently called Seebeck-coefficient), σ the electrical conductivity, κ the thermal conductivity and T the temperature. For practical applications, materials should exhibit a ZT > 1. But it is not a trivial task to reach this goal. Conventionally (i.e. in metals and semiconductors), an increase of the Seebeck-coefficient involves a decrease of the electrical conductivity. Also, the electrical conductivity and the electronic part of the thermal conductivity are coupled via the Wiedemann - Franz law:

$$\frac{\kappa}{\sigma} = \frac{\pi^2}{3}\left(\frac{k_B}{e}\right)^2 T$$
Equation 2

with k_B being the Boltzmann constant and e the elementary charge. Consequently modifying one of the parameters also results in a modification of the other parameters. Different approaches were pursued to modify one of the properties separately.

The frequently pursued approach is to modify the thermal conductivity without influencing the electrical conductivity. This goal should be reached by introducing particles into a material or using interfaces as phonon scatterers (for more information see Dresselhaus et al. and references within [1]). The thin film formation is also an important approach to modify ZT. An enhancement of the Seebeck-coefficient due to dimensionality effects was predicted by different groups (for more information see Pichanusakorn et al. and references within [2]). The size effect could be experimentally shown by Ohta et al. for $SrTiO_3$/Nb-$SrTiO_3$ superlattices [3] and Gregori et al. for nanocrystalline $SrTiO_3$ [4].

An alternative approach to overcome the limitations given by the Wiedemann – Franz law is to combine layers with high metallic conductivity and those with high Seebeck-coefficients. These structurally block-by-block layered materials are either natural ones such as the layered cobaltites, or artificial ones generated by thin film technologies.

In general, complex oxides are promising candidates for thermoelectric applications. They exhibit higher Seebeck-coefficients compared to metals and are chemically more robust. Also, complex oxides are stable up to high temperatures in contrast to semiconductors already used in practical thermoelectric energy generators.

Beside the practical benefit of the research of the thermoelectric properties, the investigation of the Seebeck-coefficient can be used to study the physical properties of materials. Since the Seebeck-effect is determined by the entropy transport, it makes it an excellent tool to investigate material properties complementary to standard resistivity and Hall effect measurements. It is very sensitive to the charge carrier type and their concentrations so it can be used as a standard for ion concentrations or ratios. Especially for cuprate superconductors, it can be used as a standard for the charge carrier concentration. Also the ratios between manganese valences in manganese oxides can be estimated using the Seebeck-coefficient. In addition, changes of the temperature dependent Seebeck-coefficient *S(T)* can be an indicator for phase transitions in materials.

The main part of the work deals with the investigation of the physical properties of superconducting $YBa_2Cu_3O_{7-\delta}$ and ferromagnetic $La_{2/3}Ca_{1/3}MnO_3$ and heterostructres and superlattices of both materials. So far, the interactions between both materials were examined by investigating the electrical conductivity [5], the magnetic properties [6-8], the shifts of the transition temperatures [6, 9] and the coupling of the phonon modes [10]. The thermoelectric properties of $YBa_2Cu_3O_{7-\delta}/La_{2/3}Ca_{1/3}MnO_3$ heterostructures and superlattices were not studied until now. The investigation should shine more light on the origin of the interactions between both materials and the occurrence of both antagonistic ground states simultaneously. Also, a superlattice formation of materials with different properties can lead to a tremendous enhancement of the Seebeck-coefficient as shown for $SrTiO_3/Nb\text{-}SrTiO_3$ superlattices by Otha et al. [3].

The thin films used in this thesis exhibit mainly a total thickness of 2000 Å. The concept was to investigate at first the physical properties of single layer $YBa_2Cu_3O_{7-\delta}$ and $La_{2/3}Ca_{1/3}MnO_3$. In a second step, heterostructures and superlattices of both materials were created also with a total thickness of 2000 Å. Creating systems with constant thickness and varying number of interfaces should lead to knowledge about the mutual influences between both materials and the properties of the interface between both materials.

The theoretical description and the background of the three thermoelectric effects are introduced in Chapter 2, including the thermoelectric properties of multilayered thin film systems and the anisotropic materials. An introduction of the physical properties of the materials mainly investigated in this study ($YBa_2Cu_3O_{7-\delta}$ and $La_{2/3}Ca_{1/3}MnO_3$) and a short overview of the interactions between these materials is given in Chapter 3.

Chapter 4 gives an overview over the experimental facilities used in this thesis. At first the preparation of thin films by Pulsed Laser Deposition (PLD) and the thin film growth is described, followed by a description of the physical properties of the substrates used for the studies. The second part of the Chapter 4 introduces the

experimental set-up used for the investigation of the Seebeck-coefficient and the electrical resistivity.

The results of the investigations and their discussions are presented in Chapter 5. The knowledge of the physical properties of the single layer materials is the basis for the discussion of possible effects and interactions between them. Consequently, the properties of single layer $YBa_2Cu_3O_{7-\delta}$ and $La_{2/3}Ca_{1/3}MnO_3$ were studied. The investigations of $YBa_2Cu_3O_{7-\delta}$ (Chapter 5. 1.) were done using samples produced under different preparation conditions and oxygen contents. $La_{2/3}Ca_{1/3}MnO_3$ was studied using different substrates to receive information about possible strain related effects (Chapter 5. 2.). Heterostructures of $YBa_2Cu_3O_{7-\delta}$ and $La_{2/3}Ca_{1/3}MnO_3$ (Chapter 5. 3. 1.) were examined using different systems and preparation conditions, to receive information about the conditions for heterostructures with relatively thick individual layers (thickness of 500 Å to 1000 Å). The results of the superlattices grown on $SrTiO_3$ are shown in Chapter 5. 3. 2. and discussed in the context of the recent investigations in $YBa_2Cu_3O_{7-\delta}/La_{2/3}Ca_{1/3}MnO_3$ superlattices. In addition, heterostructures and superlattices grown on $NdGaO_3$ were investigated using an additional post deposition annealing step (Chapter 5. 4.). Chapter 5. 5. shows the results obtained from $PrBa_2Cu_3O_{7-\delta}/La_{2/3}Ca_{1/3}MnO_3$ heterostructures. These investigations were done to examine possible influences of the contacts on the measurements and the results. The investigations of the anisotropic properties of $YBa_2Cu_3O_{7-\delta}$, $La_{2/3}Ca_{1/3}MnO_3$ and heterostructures and superlattices of both materials are shown in Chapter 5. 6. A summary of the results is given in Chapter 6.

Chapter 2

Theory of thermoelectric effects

This Chapter includes the basic description of thermoelectricity. It also covers the thermoelectric properties of multilayer structures. In addition, the properties of the Seebeck-coefficient of anisotropic materials are described.

2. 1. The thermoelectric phenomena

The thermoelectric effect was discovered by Thomas Seebeck in 1821. Seebeck built a conductor ring consisting of two materials and heated one of the contact points. In between the loop he installed a magnetic needle. He realized an alignment of the needle, that could only be induced by a magnetic field. Seebeck was convinced that the magnetic field was caused by the temperature gradient itself. His conjecture was the existence of a relation between an electrical current and a magnetic field. The quantitative relation between a current and the magnetic field was discovered later (Ampère's law 1826).

The Seebeck-coefficient describes the relation between an electrical current generated by a temperature gradient. Assuming, a metallic wire or a long bar is heated at one side and cooled at the other one. A temperature gradient will be established along the sample. The energy and therefore the mobility of the charge carriers at the heated side of the sample is enlarged in comparison to the cold end. So the charge carriers with a higher mobility will move in the direction of the colder part of the sample. Following, the charge carrier concentration at the cold side of the sample is increased. Subsequently, a potential difference is established between both sides of the sample. The potential difference ΔU across the sample caused by the temperature difference ΔT is directly proportional to ΔT und connected by the Seebeck-coefficient S.

$$\Delta U = S\Delta T \qquad\qquad \textbf{Equation 3}$$

The dependence shown in Equation 3 is just an approximation since the Seebeck-coefficient is temperature dependent. So the Seebeck-coefficient $S(T)$ results from a potential difference generated by infinitesimally small temperature differences:

$$S(T) = \lim_{\Delta T \to 0} \frac{\Delta U}{\Delta T} = \frac{\partial U}{\partial T} \qquad\qquad \textbf{Equation 4}$$

The inversion of the Seebeck-effect was discovered by Jean Peltier in 1835. He applied a direct current at one contact point of a conductor ring consisting of two different materials and discovered that one contact points warms up whereas the second contact point cools down. So heat is absorbed and rejected at the contact points and a heat flux is established. In contrast to the Seebeck-effect, which also emerges in an open circuit, the Peltier-effect is only present in a closed conductor ring. The ratio between the induced current I and the transported heat Q is expressed by the Peltier-coefficient Π and the following expression:

$$\dot{Q} = \Pi * I \qquad\qquad \textbf{Equation 5}$$

The third thermoelectric effect is called Thomson effect, named after William Thomson. Assuming, an electrical current J is applied along a homogeneous conductor with an applied temperature gradient dT. The charge carriers will gain or release energy, in dependence on the migration direction of the charge carriers to the temperature gradient. So the charge carriers adsorb or release heat that is observable in a change of the temperature gradient. The amount of heat transported along the sample $d\dot{Q}$ is given by:

$$d\dot{Q} = \tau J dT \qquad\qquad \textbf{Equation 6}$$

where τ is the Thomson coefficient of the material.

2. 2. Thermoelectric effects in multilayer systems

The thermoelectric properties of multilayer systems (heterostructures and superlattices) consisting of two different materials are depending in a first approximation on a simple combination of the thermoelectric properties of the individual single layers. This assumption only holds, if one can exclude any interaction between both materials. Since the heterostructures and superlattices discussed in this thesis are structures with a repetition of n bilayers of two materials, a bilayer system is a model system for the following considerations. Systems with temperature gradients parallel ($\Delta T_=$) and perpendicular ($\Delta T\perp$) to the thin films are discussed in the following, whereas the resulting Seebeck-coefficients are always regarded to be parallel to the temperature gradient (c.f. see Fig. 1)
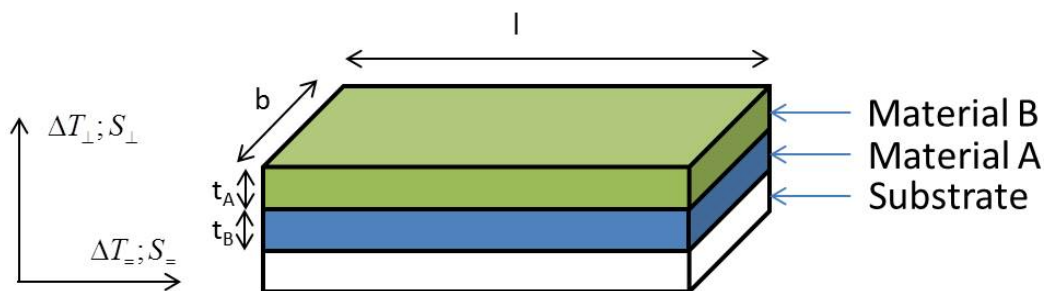
Fig. 1: Schematic view of a bilayer with temperature gradients and Seebeck-coefficients

A system with a temperature gradient parallel to the thin films can be assumed as two parallel electrical conductors according to Kirchhoff's first law:

$$\sum_{k=1}^{n} I_k = 0 \ \text{ or } \ I = I_A + I_B \qquad\qquad \textbf{Equation 7 a and b}$$

where *I* is the current and the index *A* and *B* the material A and B, respectively. Using Ohm's law ($U = R \times I$; R = resistance) and the thermoelectric relation $U = S \times \Delta T$, Equation 7 develops to:

$$\frac{S_{=} \times \Delta T}{R} = \frac{S_A \times \Delta T}{R_A} + \frac{S_B \times \Delta T}{R_B}$$

Equation 8

with

$$\frac{1}{R} = \frac{1}{R_A} + \frac{1}{R_B}$$

Equation 9

The temperature gradients are regarded to be the same over the whole sample thickness, since those are mainly driven by the substrate. The relation between the resistance and the resistivity (Equation 10) leads to Equation 11, whereat the length l and the width b of the materials are always equal and only the thicknesses t differ.

$$R = \rho \times \frac{l}{t \times b}$$

Equation 10

$$S_{=} = \frac{\dfrac{S_A \times t_A}{\rho_A} + \dfrac{S_B \times t_B}{\rho_B}}{\dfrac{t_A}{\rho_A} + \dfrac{t_B}{\rho_B}}$$

Equation 11

Finally, the Seebeck-coefficient of a heterostructure or a superlattice is a simple combination of the properties of the corresponding materials and is given by:

$$S_{=} = \frac{\displaystyle\sum_i \frac{S_i \times t_i}{\rho_i}}{\displaystyle\sum_i \frac{t_i}{\rho_i}}$$

Equation 12

An additional contribution to the Seebeck-coefficient of the substrate at temperatures up to 400 K can be completely neglected because of the insulating behavior of the substrates used in this thesis (STO, LSAT, NGO).

If a temperature gradient is applied perpendicular to the thin films, the resulting Seebeck-coefficients can be calculated following Kirchhoff's second law:

$$\sum_{k=1}^{n} U_k = 0 \ \text{ or } \ U = U_A + U_B$$

Equation 13 a and b

Using the thermoelectric relations, Equation 13 develops to:

$$S_{\perp}\Delta T = S_A \Delta T_A + S_B \Delta T_B$$

Equation 14

Since the thermal conductivity of both materials is different, the temperature gradients in both materials are unlike. So the Seebeck-coefficient of a superlattice perpendicular to the sample surface results to:

$$S_= = \frac{\sum_i \dfrac{S_i \times t_i}{\kappa_i}}{\sum_i \dfrac{t_i}{\kappa_i}}$$

Equation 15

where κ is the thermal conductivity. The development of Equation 15 can be done analog to the development of Equation 12 using the relations between the thermal conductivity κ and the temperature difference ΔT.

2. 3. Anisotropy of thermoelectric effects

Depending on the symmetry of the crystalline structure of a compound, the thermoelectric properties of a material can be anisotropic as shown by Lengfellner et al. [11] and Renk et al. [12]. So the Seebeck-coefficient of an anisotropic material can be written as a tensor:

$$S_{ik} = \begin{pmatrix} S_{aa} & S_{ab} & S_{ac} \\ S_{ba} & S_{bb} & S_{bc} \\ S_{ca} & S_{cb} & S_{cc} \end{pmatrix}$$
Equation 16

Depending on the symmetry of the crystal, the Seebeck-tensor simplifies. The materials investigated in this thesis are the pseudocubic LCMO and the orthorhombic YBCO. In the case of thin films, YBCO can be treated as tetragonal material since there is no preferred orientation of the a- and b-directions in reference to the substrate. The heterostructures and superlatttices are again regarded as a bilayer system because of its periodicity. Since the in plane lattice parameters of YBCO and the lattice parameters of LCMO nearly matching and only the c-axis length of YBCO differ, a bilayer system is regarded to be a tetragonal material. So the Seebeck-tensor reduces to:

$$S_{ik} = \begin{pmatrix} S_{aa} & 0 & 0 \\ 0 & S_{aa} & 0 \\ 0 & 0 & S_{cc} \end{pmatrix}$$
Equation 17

because of the symmetry.

For samples grown on vicinal cut substrates, the crystallopraphic orientation is tilted by an angle α with respect to the measurement directions. The Seebeck-tensor has to be transformed using the transformation matrix Y:

$$Y = \begin{pmatrix} \cos\alpha & 0 & -\sin\alpha \\ 0 & 1 & 0 \\ \sin\alpha & 0 & \cos\alpha \end{pmatrix}$$

Equation 18

and results to:

$$S'_{ik} = \begin{pmatrix} S_{ab}\cos^2\alpha + S_c\sin^2\alpha & 0 & \frac{1}{2}(S_{ab} - S_c)\sin 2\alpha \\ 0 & S_{ab} & 0 \\ \frac{1}{2}(S_{ab} - S_c)\sin 2\alpha & 0 & S_{ab}\cos^2\alpha + S_c\sin^2\alpha \end{pmatrix}$$

Equation 19

The generation of an in plane voltage U by a temperature gradient ΔT perpendicular to the sample surface is shown schematically in Fig. 2:
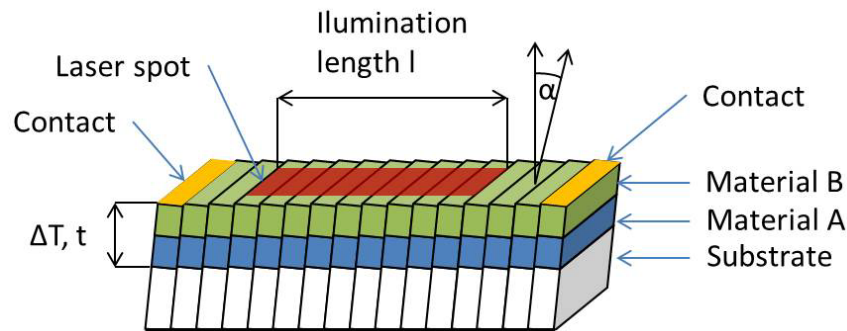
Fig. 2: Off diagonal thermoelectric voltage in multilayer systems

A laser spot with an illumination length l will generate a temperature gradient ΔT from the thin film surface to the substrate over a thickness t. According to Lengfellner et al. [11] a transversal voltage is generated between the contacts. The voltage follows the following expression:

$$U = \frac{l}{2t}(S_{ab} - S_c)\Delta T \sin 2\alpha$$

Equation 20

were S_{ab} and S_c are the in plane and out of plane Seebeck-coefficients of the sample, respectively, and α the off cut angle of the thin film.

Chapter 3

Properties of the investigated materials

This chapter gives a short overview of the physical properties of the materials investigated in this thesis. First, the crystallographic and electronic properties of the high temperature superconductor Yttrium Barium Copper Oxide ($YBa_2Cu_3O_{7-\delta}$) are discussed, especially in dependence of the oxygen content and doping. Second, the properties of the ferromagnetic/paramagnetic $La_{1-x}Ca_xMnO_3$ are introduced. Third, models for the interactions between superconductivity and ferromagnetism are introduced in respect to recent studies by different groups.

3. 1. Physical properties of $YBa_2Cu_3O_{7-\delta}$ ($YBa_2Cu_3O_{6+x}$)

Yttrium Barium Copper Oxide ($YBa_2Cu_3O_{7-\delta}$, $YBa_2Cu_3O_{6+x}$ or YBCO) is a type II superconductor, consisting of three oxygen deficient perovskite-type building blocks stacked on each other. A unit cell of $YCuO_2$ enclosed by two unit cells of $BaCuO_2$ or $BaCuO_{2.5}$, results in perovskite-like structures of tetragonal $YBa_2Cu_3O_6$ or orthorhombic $YBa_2Cu_3O_7$, respectively, as shown in Fig. 3. The unit cell consists of two CuO_2 planes aligned perpendicular to the (001) orientation indicated in Fig. 3. They enclose the Y atom in the center of the unit cell and are aligned as so called bilayers. The CuO_2 planes are surrounded by two BaO layers and one CuO chain. The oxygen content of $YBa_2Cu_3O_{6+x}$ can be varied by changing oxygen content in the CuO chains. YBCO with an oxygen content $x < 0.4$ exhibits a tetragonal structure (space group P4/mmm) and an orthorhombic structure (space group Pmmm) with an oxygen content $x > 0.4$.
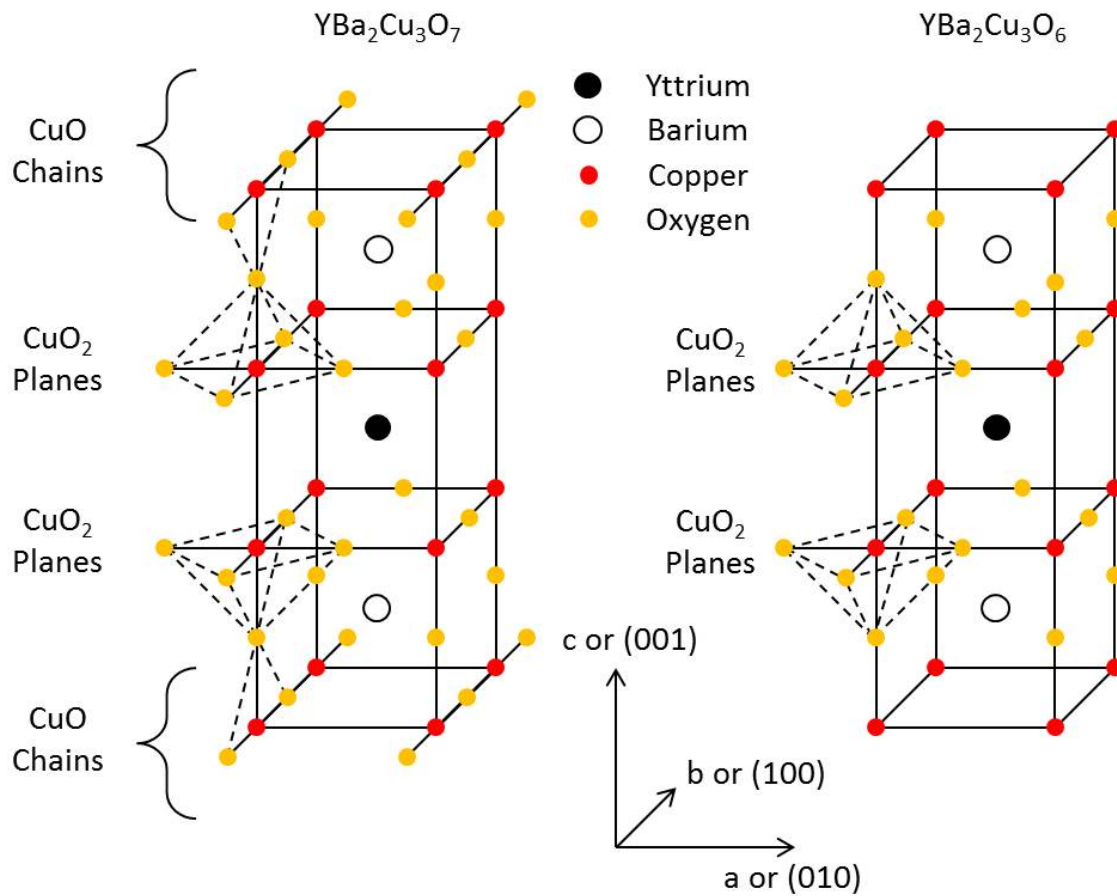
Fig. 3: Crystalline structure of YBa$_2$Cu$_3$O$_7$ with completely filled and YBa$_2$Cu$_3$O$_6$ with empty CuO chains

The physical properties (electrical, magnetic and thermoelectric) of YBCO are strongly dependent on the oxygen content in the CuO chains. The phase diagram of YBCO in dependence of temperature and doping is shown in Fig. 4 schematically. Whereas YBa$_2$Cu$_3$O$_6$ is an insulator, YBa$_2$Cu$_3$O$_{6+x}$ is a hole doped metallic conductor for temperatures $T > T_C$ and T^* (see Fig. 4). With an oxygen content $x < 0.4$ it is insulating and exhibits an antiferromagnetic ground state (below the Néel temperature T_N); for $x > 0.4$ it is metallic and shows superconductivity below the superconducting transitions temperature T_C. Changes of the oxygen content in the CuO chains modify the hole concentration in the CuO$_2$ planes by attracting electrons from the CuO$_2$ planes. The superconducting transition temperature T_C increases with increasing oxygen content to a maximum T_C of 92 K for an oxygen content of $x = 0.95$ and decreases afterwards. In general, YBa$_2$Cu$_3$O$_{7-\delta}$ is used as chemical formula instead of YBa$_2$Cu$_3$O$_{6+x}$ where δ is the oxygen deficiency of YBCO in reference to YBa$_2$Cu$_3$O$_7$. Heating optimal doped YBCO to temperatures higher 92 K,

the superconductivity collapses and YBCO enters the metallic state. It is also called a strange metal due to the linear temperature dependent of the in-plane resistivity. In underdoped superconducting YBCO, the so called pseudogap is observed in a variety of physical quantities before a temperature T^*. The transition between the metallic phase and the pseudogap is not well defined, and it is still not clear if it constitutes a true phase transition or a crossover. The origin of the pseudogap is still strongly debated. One theory describes the pseudogap as precursor state to superconductivity where electron pairs are pre-formed. In contrast, a second model explains the pseudogap as an ordered state which competes with superconductivity. In addition, recent investigations using Hall effect [13] and Seebeck-coefficient [14] measurements identified an additional characteristic temperature T_H inside the pseudogap. This temperature can be related with an onset of a Fermi-surface reconstruction according to LeBoeuf et al. [13]. Ghiringhelli et al. [15] attributed this reconstruction to a charge ordering instability.
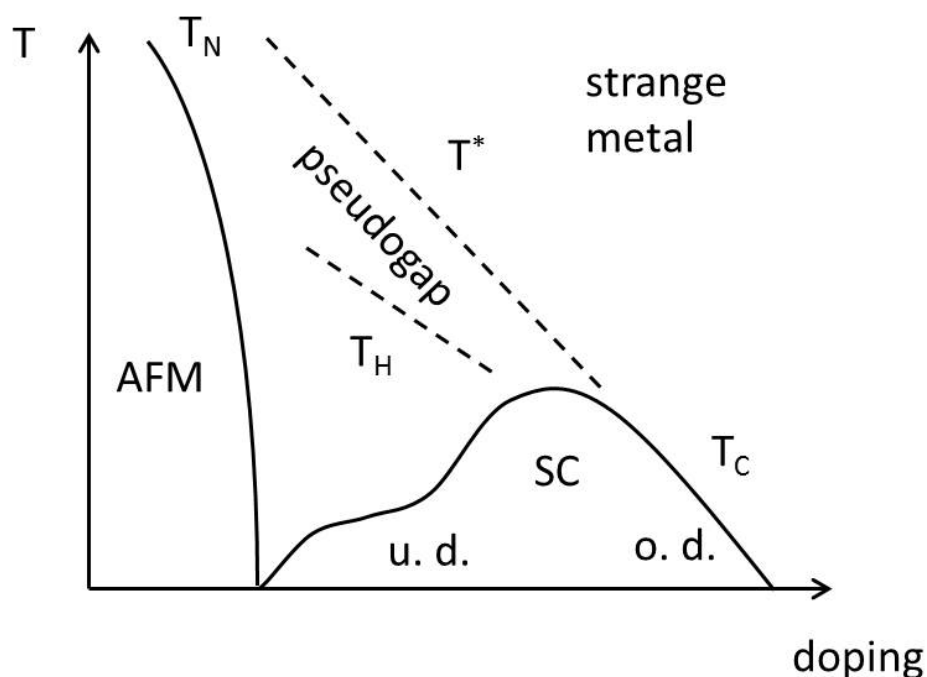
Fig. 4: Schematic phase diagram of YBCO

The resistivity of YBCO is anisotropic due to the anisotropic crystalline properties. The resistivity in the a- and b-directions (parallel to the CuO_2 planes) of YBCO are more than one magnitude smaller compared to the resistivity in the c-direction

(perpendicular to the CuO_2 planes) as shown by Friedmann et al. [16] for twin free single crystals. Also the transport properties of the a- and b-direction differ from each other. Whereas the conductivity in the a-direction is dominated by the CuO_2 planes, the CuO chains also contribute to the conductivity in the b-direction. Subsequently, the resistivity in the b-direction is smaller compared to the a-direction.

The Seebeck-coefficient of optimally doped YBCO is strongly anisotropic as reported for YBCO single crystals [17, 18] and polycrystalline samples [19]. The Seebeck-coefficients of the ab-plane ($S_{ab}(T)$) are small and negative and nearly temperature independent. In contrast, the Seebeck-coefficient of the c-direction ($S_c(T)$) of YBCO is positive and exhibits a strong temperature dependence. The absolute values of $S_c(T)$ are more than one magnitude higher compared to $S_a(T)$ and $S_b(T)$. Similar to the resistivity, the Seebeck-coefficients of the a- and b-direction differ because of the additional contribution of the CuO chains in the b-direction. The thermoelectric properties of YBCO are explained in detail in Chapter 5. 1.

3. 2. Physical properties of $La_{2/3}Ca_{1/3}MnO_3$

$La_{2/3}Ca_{1/3}MnO_3$ belongs to the family of the doped rare-earth manganites with the general formula $Ln_{1-x}A_xMnO_3$, where Ln is a trivalent cation like La^{3+}, A a divalent cation like Ca^{2+}, Sr^{2+}, Ba^{2+} and Mn a trivalent (Mn^{3+}) or tetravalent (Mn^{4+}) atom. The ratio between Mn^{3+} and Mn^{4+} is driven by the ratio of the bi and trivalent atoms. The atoms are arranged in a perovskite structure. The manganese atom in the center of the unit cell is surrounded by an octahedron of six oxygen atoms. The La and Ca atoms are settled at the corners of the unit cell, respectively.

Lanthanum (La^{3+}) or Calcium (Ca^{2+})
Manganese (Mn^{3+} or Mn^{4+})
Oxygen (O^{2-})
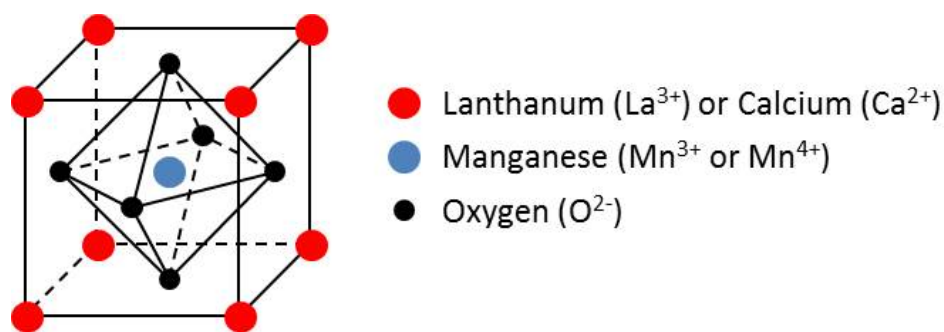
Fig. 5 Crystalline structure of $La_{2/3}Ca_{1/3}MnO_3$

The parent compounds of $La_{2/3}Ca_{1/3}MnO_3$ are $LaMnO_3$ and $CaMnO_3$; both antiferromagnetic insulators. The mixture of both compounds ($La_{1-x}Ca_xMnO_3$) leads to a rich phase diagram including a ferromagnetic insulating and charge ordered phase (x ≈ 0.1 to 0.2), a ferromagnetic metallic phase (x ≈ 0.2 to 0.5) and an antiferromagnetic and a charge ordered state (x ≈ 0.5 to 0.9). The regions with a doping x < 0.1 and x > 0.9 exhibit similar properties as the parent compounds. All compounds become paramagnetic and insulating at higher temperatures, depending on the doping.
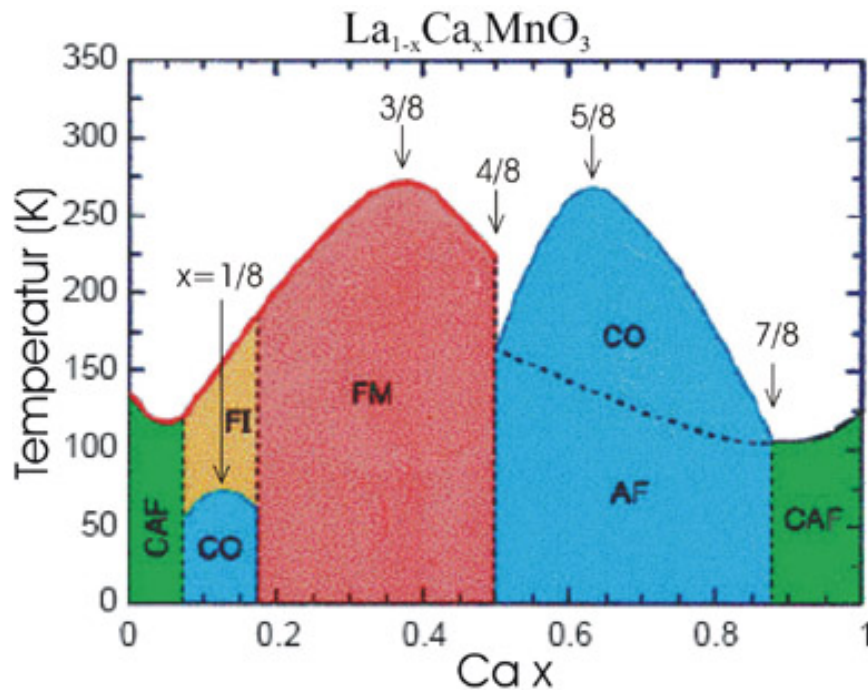
Fig. 6: Phase diagram of La$_{1-x}$Ca$_x$MnO$_3$ taken from Cheong at al. [20]

In one of the parent compounds, LaMnO$_3$, the valence of all manganese ions is nominally 3+. The manganese 3d-orbitals and the oxygen 2p-orbitals overlap inside oxygen octahedra. Since the distance and thus the Coulomb repulsions between the orbitals of the manganese atom and surrounding oxygen atom are partially different, the five manganese 3d-orbitals split up into three t$_{2g}$-levels with a decreased and two e$_g$-levels with an increased energy. Assuming a Mn^{3+} ion exhibits four 3d-electrons, the three t$_{2g}$-levels and one e$_g$-level are half filled. The spins of the electrons are all parallel due to Hund's rule.

Furthermore, the e$_g$ as well as the t$_{2g}$ levels are splitting up into different energetic states, as a consequence of the Jahn-Teller effect of Mn^{3+}. In addition, one direction of the octahedra is elongated and the other two directions shrink. In contrast in CaMnO$_3$, the Mn^{4+} exhibits three 3d-electrons and only the t$_{2g}$-levels are occupied and no Jahn-Teller-effect occurs. Starting from pure LaMnO$_3$, the Jahn-Teller-effect is weakened by substituting Ca and vanishes in CaMnO$_3$.

Due to the Jahn-Teller-effect, the manganese octahedra are distorted and due to the mismatch of the ionic radii of La^{3+} and Ca^{2+} slightly tilted with respect to each other.

The structure of the atomistic level effect the bond distances and bond angles of the elementary Mn-O-Mn building block. Consequently, the distortion of the octahedra is influencing the electronic and magnetic properties of the manganites.

The manganese atoms with the different valences (Mn^{3+}, Mn^{4+}) are randomly distributed in the crystal. The Mn^{3+} has a spin state of $S = 2$ and the Mn^{4+} of $S = 3/2$. An electron can only move from the e_g state of the Mn^{3+} to the empty e_g state of a Mn^{4+}. Due to the strong Hund's coupling, the hopping can only occur, if the spins of the t_{2g} electrons are parallel aligned. In principle, two electrons are hopping simultaneously. One electron is hopping from the Mn^{4+} to an oxygen atom and a second electron is hopping from the oxygen atom to a Mn^{3+}. This process is called "double exchange" mechanism. The spin alignment leads to a ferromagnetic ground state of the electrons.

The ferromagnetic metallic ground state develops into a paramagnetic insulating state while heating up to temperatures higher T_{Curie}. The transition can be characterized using magnetization or resistivity measurements. Investigating the electrical resistivity, the transition is indicated by a broad maximum. By applying a magnetic field, the maximum is shifted to higher temperatures and the resistivity is reduced. This is caused by the alignment of spins of the manganese ions by the external field. Originally, the spins of the manganese ions are parallel aligned in the ferromagnetic state at low temperatures. While heating up to higher temperatures, the spins get thermally exited and can be slightly tilted to each other. The tilting increases with increasing temperatures, what results in an increase of the electrical resistivity. The tilting can be reduced by an external magnetic field and the electrical resistivity decrease. Also the spins of the manganese ions in the paramagnetic state are aligned by the magnetic field. So the movement of the electrons via the "double exchange" mechanism is energetically favorable to the thermally activated processes in the original paramagnetic phase. Consequently, the electrical resistivity can be strongly suppressed by this process (up to three orders of magnitude). This effect is called the collosal magnetoresistance (CMR) effect.

The conduction mechanisms at high temperatures in the paramagnetic insulating state are still widely discussed in the literature. Different groups [21-24] found evidences for electron phonon interactions restricted over a small length scale, the so called small polaron or Holstein polaron. The investigations are supported by Seebeck-coefficient and Hall coefficient measurement (as overview see Salamon et al. and references therein [23]).

3. 3. Interactions between $YBa_2Cu_3O_{7-\delta}$ and $La_{2/3}Ca_{1/3}MnO_3$

The heterostructures and superlattices consisting of YBCO and LCMO have been widely investigated due to the antagonistic long range order phenomena occurring in both systems. The electron spins of the ferromagnetic LCMO are parallel aligned, whereas the spins are in a singlet state in the Cooper pairs of the superconducting YBCO. The previous work focuses on the mutual influences between both materials on the electrical conductivity [5], the magnetic properties [6-8, 25] and especially the shifts of the transition temperature [6, 9] and the coupling of the phonon modes [10]. Different scenarios were discussed to explain the phenomena occurring at the interfaces of YBCO and LCMO. In general, the effects and interactions are discussed either to be restricted to a small range near the interface (20 Å [7]) or propagate over a long range (up to 500 Å [10]).

A proximity effect, where Cooper pairs penetrate into the ferromagnetic layer, can weaken the ferromagnetic properties of the LCMO layers. Several studies of superlattices [6, 26] show a reduction of T_{Curie} by changing the YBCO thickness and holding the LCMO thickness constant. Also the inverse proximity effect, where the ferromagnet influences the properties of the superconducting layer, is widely discussed. The spin polarized electrons penetrating into the superconductor can destroy the Cooper pairs and thus suppress the superconductivity and shift the T_C to lower temperatures. Another often discussed phenomenon is the so called charge transfer between YBCO and LCMO. Holes from the YBCO layers can penetrate through the interface between both materials into the LCMO layers. This causes a reduction of the hole concentration in YBCO similar to an oxygen deficiency and thus a reduction of T_C. On the other side, the rising hole concentration in the LCMO layers increases the Mn^{4+} concentration.

Some of the most important studies on the interactions between YBCO and LCMO and the properties of the interface between both materials are presented in the following. This should give an overview about preliminary studies and can be seen as a background for the investigations done in this thesis. The work done on

YBCO/LCMO superlattices by Malik et al. [27] and Driza et al. [10] are not presented here. They are discussed together with the results of this thesis in the corresponding chapters.

The proximity effects in YBCO/LCMO superlattices were studied by Sefrioui et al. [6] using transport and magnetization measurements. First they investigated superlattices with a constant YBCO thickness (5 unit cells) and variable LCMO thicknesses (3 to 90 unit cells). They found a systematic suppression of T_C with increasing LCMO thickness, except for LCMO with thicknesses smaller 5 unit cells, where T_C is not significantly suppressed. The magnetization measurements of these samples at 90 K show a reduction of the magnetization of LCMO with decreasing LCMO thickness, similar to the thickness dependence of ultrathin LCMO films reported before [28]. The absence of the T_C suppression in the samples with small LCMO thicknesses was attributed to the reduction of the magnetization in the thin LCMO layers. Second they study samples with LCMO thicknesses of 5 unit cells and varying the YBCO thickness. Only for samples with YBCO layer thicknesses of 1 and 2 unit cells they could not observe superconductivity, which was attributed to a possible discontinuity of the layers over long lateral distances. With increasing YBCO thickness from 3 to 12 unit cells, also T_C increases up to 85 K. They also show that the suppression of T_C is reduced, when the ferromagnetic LCMO were replaced by insulating $PrBa_2Cu_3O_7$ layers with similar thicknesses.

Holden et al. [5] investigated the electronic properties of YBCO/LCMO superlattices using spectroscopic ellipsometry. They found a strong decrease of the free carrier response in the supperlattices in comparison to pure YBCO and LCMO thin films. The suppression occurs in the superconducting as well as the metallic state and emerges even for superlattices with YBCO thicknesses of 16 nm. The strongest effects were found for samples with equal YBCO and LCMO thicknesses. In contrast, no reduction of the conductivity was found when the ferromagnetic metallic LCMO layers were replaced by layers of insulting $PrBa_2Cu_3O_7$ or the paramagnetic metal $LaNiO_3$. Their observations were attributed to a charge transfer of holes moving YBCO and LCMO, or a charge localization due to magnetic correlations between both materials, induced by an exotic long range proximity effect.

Hoffmann et al. [29] investigated LCMO/YBCO superlattices focusing on the magnetic properties of both materials and the interface between them. They found a suppression of the ferromagnetic ordering at the interface between YBCO and LCMO. Magnetization measurements of superlattices with a constant LCMO thickness and varying YBCO thickness show a reduction of the magnetization with increasing YBCO thickness. An interpretation of neuron reflectivity data done by Stahn et al. [25] came to similar experimental findings. They interpreted the differences between the nuceal and the magnetic profiles either to arise from an antiphase magnetic proximity coupling when a ferromagnetic moment is induced in YBCO or a ferromagnetically "dead layer" (either paramagnetic or antiferromagnetic) in the LCMO. The reduction of the magnetization reported by Hoffmann et al. was also correlated with an increased hole density at the Mn sites. Finally they attributed their findings to a charge transfer between YBCO and LCMO also leading to an antiferromagnetic ordering at the interface.

Chakhalian et al. [7] investigated the magnetism at the interface between YBCO and LCMO using X-ray magnetic circular dichroism (XMCD) and neutron reflectometry. They found a ferromagnetic polarization of the Cu in the YBCO layer close to the LCMO interface. The investigation of this magnetic moment of Cu was also done over a wide temperature range. The temperature dependence of the magnetic moments examined by XMCD develops analogous with the bulk magnetization of the whole sample. From the similar temperature dependences they concluded that the magnetic moment of Cu is induced by exchange interactions between the Cu spins and the ferromagnetic moment of Mn across the interface [7]. Comparing the results with earlier neutron reflectivity measurements done by Stahn et al. [25] leads to a scenario of a 10 Å thick LCMO layer with suppressed ferromagnetism and a antiferromagnetically coupled 20 Å thick spin polarized YBCO layer at the interface. Chakhalian et al. claimed that an antiferromagnetic coupling of sufficient strength to explain the experimental data can only emerge, if the electronic occupation of the interfacial orbitals of YBCO and LCMO differs from the bulk occupation. Their results suggest an orbital repopulation within the Cu e_g doublet. Chakhalian et al. also investigated the lateral magnetization of the superlattices using off-specular neutron

scattering experiments under the influence of in-plane oriented magnetic fields and found a stripe-like magnetic domain pattern resulting from different origins.

Another approach to receive information about the properties of the interface between YBCO and LCMO was done by Chakhalian et al. [8]. They were using soft X-ray absorption spectroscopy (XAS) and soft X-ray linear dichroism (XLD) to investigate the electronic structure and the orbital occupation at the interface between YBCO and LCMO. Comparing the absorption spectra at the Cu L_3 absorption edge at the interface with bulk values leads to a shift of the to lower energies with respect to the bulk value. This shift was interpreted as a sign of a change of the valence state of the Cu ions near the interface and indicates a charge transfer across the interface in a way that the hole density in YBCO is reduced at the interface. Furthermore, investigations of the polarization dependence of the Cu absorption spectra in the interface sensitive mode (total electron yield) and in bulk sensitive mode (fluorescence mode), show that at the interface at least some of the Cu 3d electrons occupy the $d_{3z^2-r^2}$ orbital yielding a nearly equal occupation of $d_{x^2-y^2}$ and $d_{3z^2-r^2}$ orbitals. Since in the bulk only the $d_{x^2-y^2}$ orbital is occupied, this is clear evidence for an orbital reconstruction at the interface. Whereas the signals in bulk YBCO differ, the spectra of the interface are nearly overlapping. This was interpreted is a manifestation of an orbital reconstruction and a modified occupation of the holes in the orbitals. A similar behavior for the LCMO absorption spectra could not be clearly identified because overlap of the 5 partially occupied Mn d orbitals. The orbital reconstruction of the interfacial Cu $d_{3z^2-r^2}$ orbital at the interface was attributed to two different physical mechanisms. First, the possibility of a raised energy of the $d_{3z^2-r^2}$ orbital above the energy of the $d_{x^2-y^2}$ orbital due to the modified crystal field environment of the Cu ions at the interface was discussed. But it was nearly ruled out because of the large energy difference between both orbitals. Second, the possibility of a creation of covalent chemical bonds at the interface were discussed since the Cu $d_{3z^2-r^2}$ are pointed directly to the interface and can hybridize with the Mn $d_{3z^2-r^2}$ orbitals via the apical oxygen ion at the interface.

Chapter 4

Experimental setup

This Chapter introduces the most important systems used in the thesis for the preparation of the samples and their investigations. The first part includes a description of the preparation of the thin film samples by the Pulsed Laser Deposition (PLD) technique and the investigation of the structural properties of the thin films. The second part introduces the systems used for the investigations of the thermoelectric properties of the thin films.

4. 1. Thin film deposition and growth mechanism

All thin film samples discussed in this thesis are made by the Pulsed Laser Deposition (PLD) technique, a physical vapor deposition (PVD) process. The general features of a PLD process are the following: A pulsed ultraviolet (UV) laser beam with a wavelength of 248 nm and pulse duration of 28 ns is focused on a target with the required material and creates a plasma plume due to its high energy impact. The emitted material is ejected to a substrate and forms a thin film. A feature of fundamental importance is the stoichiometric material transfer from the target to the film. The samples investigated were deposited in different PLD system, which vary partially in structure and geometry. Also the targets used for the ablation of the samples differ. While the same targets were used in PLD 1 and 2, PDL 5 is working with a different set of targets. Also the temperature control of the heaters in the PLD systems differs. Therefore the properties of the samples can slightly differ from PLD to PLD even using exactly the same growth conditions. The process parameters for the deposition of the different materials and material systems are included in the corresponding chapters (temperature, atmosphere, annealing time). Samples fabricated in PLD 1 were made by myself, in PLD 2 by Mr. Cristinai and in PLD 5 by Mr. Kawashima.The basic design of a PLD systems is shown in Fig. 7 schematically:
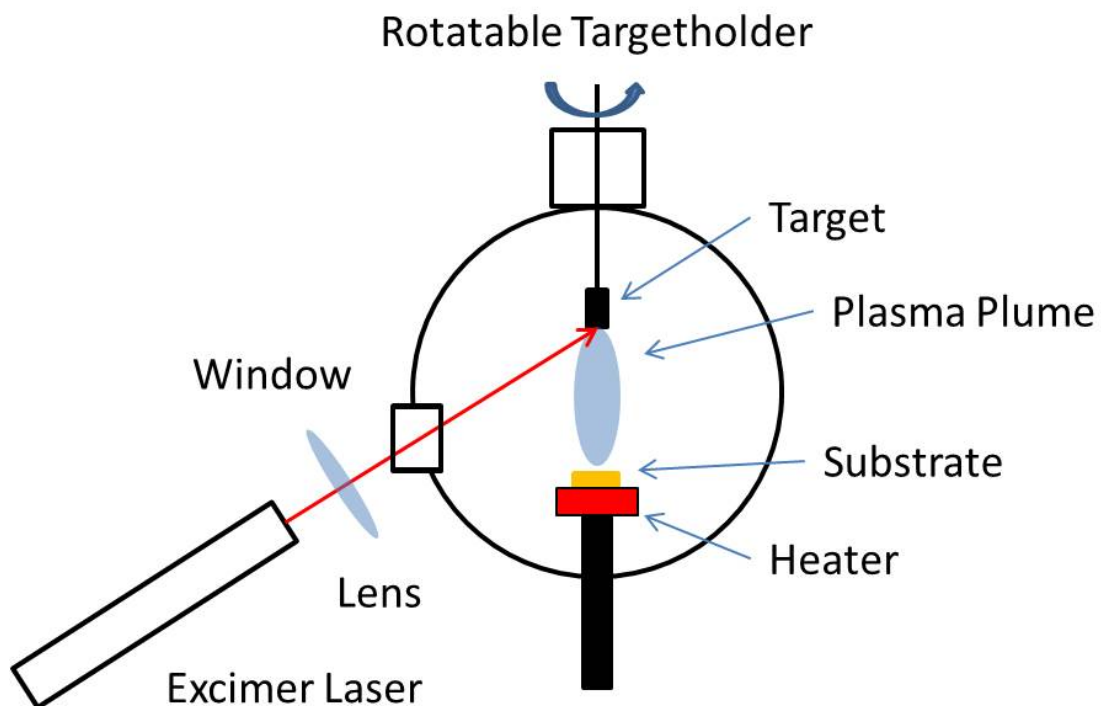
Fig. 7: Pulsed Laser Deposition system

The PLD chamber is designed as ultra high vacuum system to ensure a clean environment and a stable gas atmosphere during the process. A laser pulse created by a KrF - Excimer laser (λ = 248 nm) is focused by a lens through a window on a rotating target. This target is a dense ceramic consisting of the required material with its desired composition. The laser melts the target surface and the material is emitted as plasma plume, which is oriented perpendicular to the target surface. The amount of the emitted material depends on the pulse duration of the laser, its energy density and the spot size of the laser on the target. The plasma plume is focused on a substrate which is mounted on a holder and heated to the designated temperature for the deposition of the particular material.

The nucleation of the thin films and its growth are determined by a superposition of miscellaneous parameters like the deposition rate, the energy of the emitted material, the substrate morphology and the substrate temperature. The material (atoms, ions, agglomerates) emitted from the target condenses on the substrate surface. Depending on the kinetic energy of the material and the temperature of the substrate, the condensed material diffuses until it is forming a stable nucleus, is

added to an existing nucleus or desorbs. The nucleus density is strongly depending on the supersaturation of the emitted material on the substrate surface. A large supersaturation leads to a high nucleus density.

The thin film grows by the addition of material to the nucleus. Different growth models can appear in dependence on the mobility of the material, the critical nucleation forming size of the nucleus and the surface energy of the substrate ($\gamma_{Substrate}$), the nucleus ($\gamma_{Nucleus}$) and interface energy ($\gamma_{Interface}$) between substrate and nucleus . Assuming the nucleus behaves like a drop on the substrate, one can apply Young's Equation:

$$\gamma_{Substrate} = \gamma_{Interface} + \gamma_{Nucleus} \times \cos(\theta) \quad \rightarrow \quad \cos(\theta) = \frac{\gamma_{Substrate} - \gamma_{Interface}}{\gamma_{Nucleus}} \qquad \textbf{Equation 21}$$

where θ is the contact angle between the substrate and the nucleus.

The system always approaches the state of the lowest energy. So the ratios between the interface and surface energies determines the growth mode of the thin film. Mainly, three different growth modes exist: The Volmer-Weber growth mode, also called island growth, occurs when the sum of the interface energy and the surface energy of the nucleus is higher than the surface energy of the substrate. The layer by layer growth, the Frank-van-der Merve mechanism, emerges when the surface energy of the substrate is equal to the two other energies. It is also possible, that both mechanisms are mixed. This is called the Stranski-Krastanov mechanism, at which first a layer growth and then island growth takes place.

4. 2. Properties of the substrates used for the investigations

The choice of the right substrate is mandatory to receive an optimal growth of thin films. The substrates should be flat (roughness of less than one unit cell of the substrate) and the lattice parameter of the substrate should match the lattice parameter of the thin film to achieve optimal growth conditions and a strain free growth of the thin films. Also the thermal expansion coefficients α of the substrates and the thin films should be of the same order of magnitude to guarantee a stable strain state between substrate and thin film at any temperatures. In addition, structural phase transitions could occur in the substrate, which can lead to tremendous changes in the strain state and influences of the physical properties of the thin films.

Three different single crystalline substrates with a specific orientation were used for the thin film growth in this study: (001) oriented $SrTiO_3$ (STO), (001) oriented $(La_{0.27}Sr_{0.73})(Al_{0.65}Ta_{0.35})O_3$ (or $(LaAlO_3)_{0.3}$-$(Sr_2AlTaO_6)_{0.7}$) (LSAT) and (110) oriented $NdGaO_3$ (NGO). In addition (001) oriented STO with an off cut of 5 ° normal to the c-axis (out of plane orientation) were used to investigate the anisotropic properties of the Seebeck-coefficient. The off cut substrates are described in detail in Chapter 5. 6. In contrast to LSAT and NGO, STO exhibits a structural phase transition from cubic to tetragonal (pseudocubic) by cooling to temperatures lower 105 K.

The properties of the substrates (the crystal structure, surface orientation, lattice parameter (all values are given at 25 °C), thermal expansion coefficient) and the lattice mismatch between the substrates and the mainly investigated thin films, $YBa_2Cu_3O_{7-\delta}$ (YBCO) and $La_{2/3}Ca_{1/3}MnO_3$ (LCMO), are summarized in Table 1. Assuming similar lengths of the in plane lattice parameters of 3.854 Å for YBCO and 3.864 Å for LCMO, the lattice mismatch ζ was calculated using Equation 22:

$$\zeta = \frac{a_S - a_F}{a_F} * 100$$
Equation 22

where a_S denotes the in plane lattice parameter of the substrate surface and a_F the lattice parameter of the thin film. The surface of the orthorhombic (110) NGO was assumed to be pseudocubic with a lattice parameter of 3.861 Å for the calculations. Whereas an in plane tensile strain is induced by STO to the thin films, the strain between LSAT and NGO and the thin films is regarded to be of minor importance. The thermal expansion coefficients of the substrates (8.2 to 9 x 10^{-6} K^{-1}) are of the same order of magnitude like YBCO (13.4 x 10^{-6} K^{-1} [30]) and LCMO (comparable with LSMO with 11.6 x 10^{-6} K^{-1} [31]).

Table 1: Properties of substrates used in this study and lattice mismatch between substrate and thin films

Substrate with orientation	Crystal structure	Lattice parameter [Å] [32]	ζ (YBCO)	ζ (LCMO)	Thermal expansion coefficient α [K^{-1}] [32]
(001) STO	Cubic	3.905	1.32	1.07	9 x 10^{-6}
(001) LSAT	pseudocubic	3.868	0.36	0.11	8.2 x 10^{-6}
(110) NGO	orthorhombic	a = 5.43 b = 5.50 c = 7.71	0.18	-0.07	9 x 10^{-6}

4. 3. Sample characterization by XRD and RSM

XRD measurements were made to investigate the structural properties of the thin films. The utilized system was a Bruker D8 Discover diffractometer working with Cu-Kα radiation (λ = 1.54184 Å). The system was equipped with a fixed source and a moving sample holder and detector. 2θ - ω scans (ω is the angle between substrate and incident X-ray beam and 2θ the angle between the incident and the diffracted X-ray beam) between θ = 5 ° and 90 ° were used to investigate the thin film orientation, the phase purity of the samples and to determine the out – of - plane lattice constants (c-axis length) of the deposited materials. The c-axis length of the samples was determined from the positions of the Bragg reflections θ from the XRD measurements and applying the Nelson Riley function [33]:

$$NR = \frac{1}{2}\left(\frac{\cos^2\theta}{\sin\theta} + \frac{\cos^2\theta}{\theta}\right)$$

Equation 23

The values of the Nelson Riley function NR are plotted with the corresponding c-axis values calculated using the position of the Bragg reflections θ applying Bragg's Law (c.f. see Fig. 18 in Chapter 5. 1.). The c-axis parameter results from the extrapolation to NR = 0 (θ = 90) [33]. The method is used to eliminate instrumental errors, absorption of the XRD beam by the sample and errors occurring from the alignment of the sample. High resolution 2θ - ω scans were accomplished as an additional investigation of the sample quality and to calculated the bilayer thickness of superlattices. Reciprocal space mappings (RSM) were used to investigate the in plane and out of plane lattice parameters of thin films and the possible substrate induced strain.

4. 4. Measurement of thermoelectric properties

The investigations of thermoelectric properties were realized with three different systems. The Thermal Transport Option (TTO) in the Physical Properties Measurement System (PPMS) from Quantum Design was used for a temperature range of 2 K to 390 K and magnetic field dependencies, the ZEM-3 M8 from Ulvac for measurements from 150 K to 1070 K (- 120 °C to 800 °C) in different atmospheres and the Laser Induced Thermoelectric Voltage (LITV) system to study the anisotropic properties of thermoelectric materials. These three systems will be described in detail in the following sections.

4. 4. 1. The Thermal Transport Option (TTO)

The TTO enables measurements of the Seebeck-coefficient S, the resistivity ρ and the thermal conductivity κ. These properties allow the calculation of the thermoelectric figure of merit $ZT=S^2T/(\rho\kappa)$. For measurements of thin films, the thermal conductivity is always dominated by the substrate, consequently only the Seebeck-coefficient and the resistivity could be determined. The thermal conductivity was only used to estimate the quality of the contacts on the samples. The TTO allows measurement between 2 K and 390 K with applied magnetic fields up to 1 T and from 20 K to 390 K up to 9 T, respectively.

It is important to mention, that the TTO requires samples with a special geometrical aspect ratio, especially for thin film samples. Thus only samples with a length to width ratio of maximum 2 could be investigated. The optimal geometry for a substrate was 2 x 10 x 0.5 mm. Several steps are needed to install a sample in the TTO. First, pads consisting of chromium and gold with a nominal thickness of 20 nm and 200 nm, respectively (Cr/Au 20/200 nm), were evaporated on top of the thin film to create a reliable thermal contact between sample and sample holder (puck). Second, copper rods with a diameter of 1 mm are glued with two component silver epoxy (EPO-TEK H20E-PFC) on top of the Cr/Au pads. Third, the copper rods are

screwed in the thermocouple shoes of the sample puck. Also pads fabricated of titanium and platinum (Ti/Pt) were used as alternative contact materials to investigate possible influences of the contact material on the measurements. Two $La_{2/3}Ca_{1/3}MnO_3$ samples were deposited with the same parameters in one PLD process. One sample was contacted with Cr/Au and the other one with Ti/Pt. The investigated properties of both samples were identical and independent of the contact material.

The measurement setup is depicted in Fig. 8 a) schematically and Fig. 8 b) shows an image of a completely contacted sample. A measurement at a certain temperature is accomplished by the following routine: A heater induces a heat pulse which is running through the sample. The two so called thermo shoes (T_{hot}; T_{cold}) are monitoring the temperature as well as the signal ($V+$; $V-$) during the heat pulse. The Thermal Conductivity and the Seebeck-coefficient are calculated from the monitored temperatures and the signals, respectively [34]. The resistance is measured by a four probe alternating current technique with the AC Transport Option (ACT) of the PPMS before and after the heat pulse. All parameters for these measurements are readjusted after every single measurement at a particular temperature to receive optimal conditions.
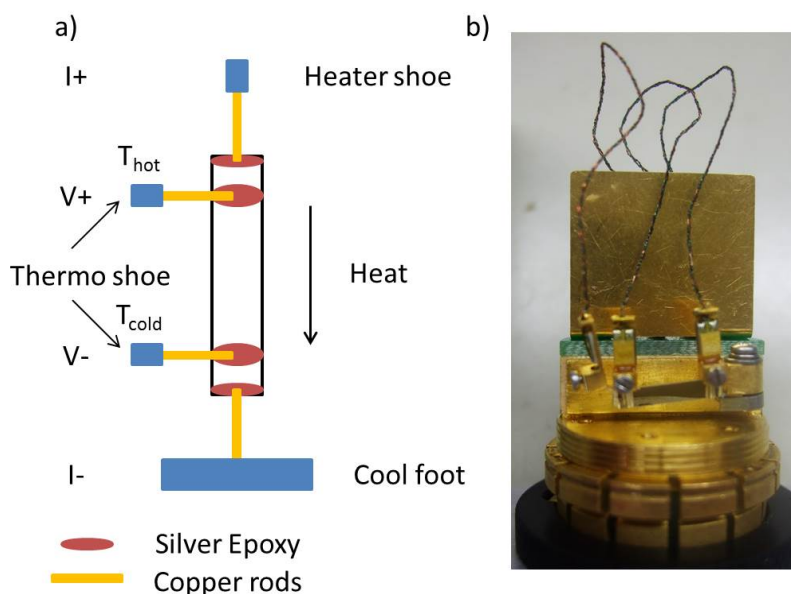

Fig. 8: a) Schematic setup and b) image of a contacted sample

The measurement is always started at low temperatures (1.9 K or 20 K – depending on the magnetic field or sample properties) and is running with a temperature rate of 0.5 K/min up to 390 K. The initial parameters for the measurement are always the same for the certain starting temperatures. The conditions for the actual sample and starting temperature are optimized during the first data points of a measurement. So these first data points should be neglected. Since the duration of the heat pulse varies for different temperature ranges, the measurement parameters are consequently changing during the temperature scan and also the density of measurement points. Below a temperature of 100 K, one can obtain one data point every 1 K to 2 K in contrast to high temperatures (above 300 K) were the distance between the single measurements amounts to 10 K to 15 K.

4. 4. 2. The ZEM-3 M8

The ZEM-3 M8 from Ulvac is a system specially designed for the investigation of the Seebeck-coefficient and the resistivity. The ZEM-3 offers the possibility to investigate these properties with a cryostat in a temperature range from - 120 °C to 100 °C and a heater option from room temperature to 800 °C. Originally, this system was designed for measurements in a helium atmosphere. The outer electrodes were fabricated using corrosive metals which made it impossible to measure in oxygen atmospheres. Replacing these electrodes by platinum and adding a pressure control, it was possible to extend the working range to oxidizing and reductive atmospheres with a control of the background pressure. To guarantee a constant pressure over the whole measurement, a needle valve is used to achieve a constant gas flow inside the system. In addition, a baratron system is used to keep the pressure constant. The baratron system consists of a pressure cell to monitor the actual pressure and a control device which drives a flexible valve that regulates the diameter of the pipe towards the pump. So it is possible to adjust pressures between 50 mbar and 950 mbar over the whole temperature range.

Because of the robust construction, it is possible to investigate a wide range of samples. For thin films, substrates with 5 x 5 mm to 10 x 10 mm area and bulk

samples with a minimum length or diameter of 5 mm can be investigated. Possible limitations are only given by the temperature stability and the chemical stability of the corresponding sample in different atmospheres and the mechanical stability of the bulk samples and substrates.

The heater option of the ZEM-3 M8 is illustrated in Fig. 9 and shown in Fig. 10. It consists of two main parts. On the right side the electronic contacts for the electrodes and the thermocouples, the connections to the gas inlet and the baratron system and the attachment for the electrodes are embedded. The left side includes the heater and the sample chamber. The complete sample chamber is covered by the heater, which consists of six quartz lamps. It is used to generate a stable temperature in the sample chamber, the base temperature. The chamber itself is enclosed by a transparent quartz tube. The heater and the tube are embedded in a sliding carriage which can be moved over the sample. This sliding carriage can be pressed with a clamping ring at the body to ensure a stable environment. A water cooling circuit is protecting this clamp against overheat. The electrodes inside the quartz tube are covered by a metal shield, which ensures a stable temperature around the sample. It contains a thermocouple that measures the base temperature as a feedback control for the quartz lamps.
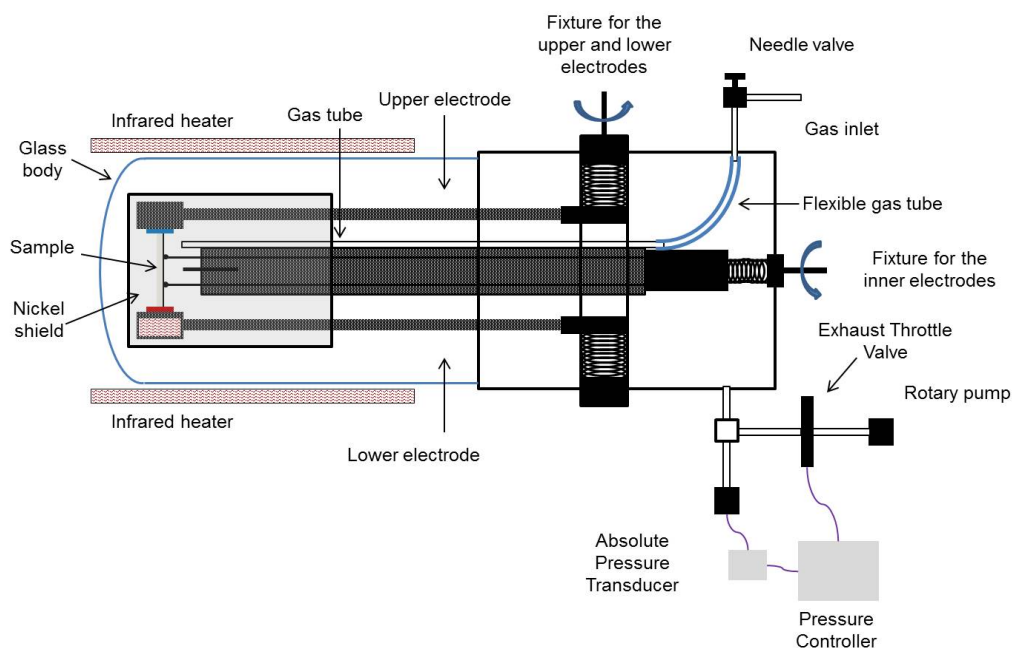

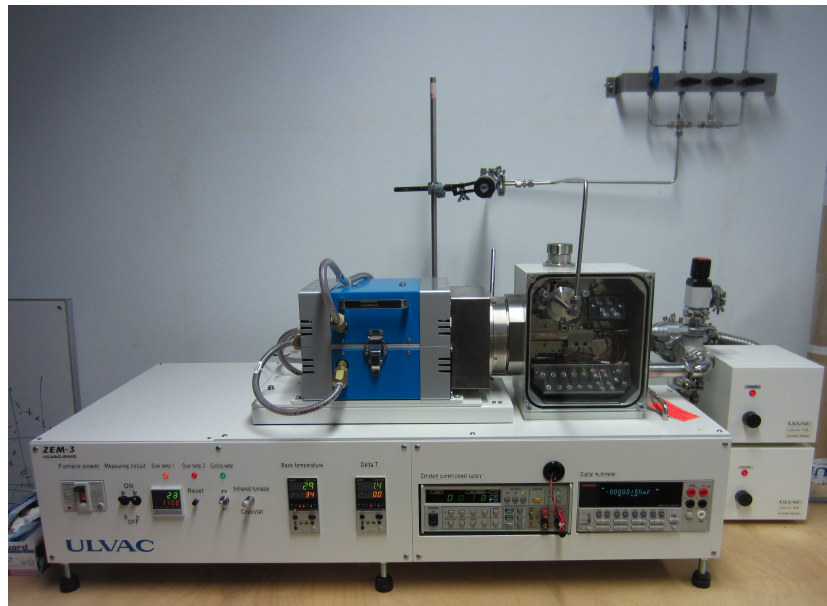**Fig. 9: ZEM-3 M8 schematic overview**

Fig. 10: ZEM-3 M8 with baratron system

The sample is contacted by four platinum electrodes (c.f. see Fig. 11 and Fig. 12). It is clamped between the upper and the lower electrode (outer electrodes) and the two inner electrodes are pressed on the sample. The lower electrode includes a platinum wire heater which is used to apply a temperature gradient along the sample and a thermocouple. A second thermocouple is installed in the upper electrode. The set point temperature difference (ΔT_1 = 20 to 40 K) is applied between these two thermocouples. The temperature difference between the inner electrodes ΔT_2 is used for the calculation of the Seebeck-coefficients and amounts between 1 K and 10 K.
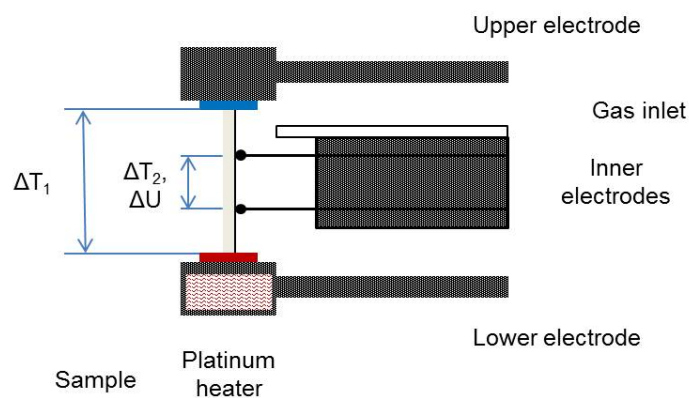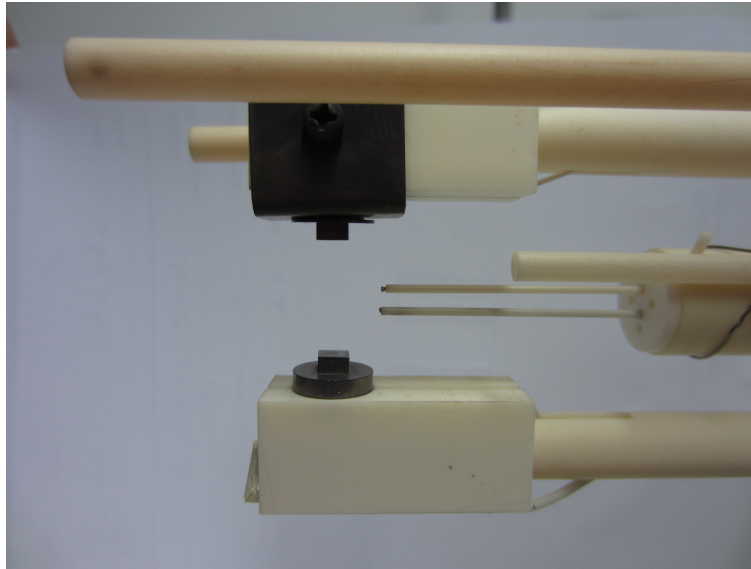

Fig. 11: ZEM-3 M8 schematic sample handling with sample

Fig. 12: ZEM-3 M8 real sample handling without sample

The whole system, expect the baratron system, is computer controlled with a lab view program. It allows one to adapt the geometry parameters of the sample, the modes for the resistivity measurements and the temperature program as well as the required temperature gradients.

The evaluation of the Seebeck-coefficients requires several measurements and calculations. At first, the temperature difference ΔT_2 and the potential difference ΔU between the inner electrodes are monitored at three different set point temperature gradients. Also the Seebeck-coefficients of the inner electrodes and the Dark Electromotive Force (EMF) are recorded. Second, the potential differences are plotted versus temperature differences. The slope of the trend line results in the so called "simple Seebeck-coefficient". A similar calculation is made for the wire Seebeck-coefficient. Third, to estimate the real Seebeck-coefficient, the "simple Seebeck-coefficient" is subtracted by the wire Seebeck-coefficient to get rid of the fraction of the inner electrodes.

The resistivity can be measured by a two point (only the inner electrodes) or in the four point (outer and inner electrodes) configuration in a sweep mode (ac mode) or a step mode (dc mode). It is monitored at every temperature gradient and the resistivity is calculated using the average of these three values.

4. 4. 3. The Laser Induced Thermoelectric Voltage (LITV) system

As described in Chapter 2. 3. the properties of the Seebeck-coefficient of a certain material can be anisotropic. These properties can be investigated by generating optically a temperature gradient perpendicular to the surface and measuring the voltage signal along the sample, the so called Laser Induced Thermoelectric Voltage (LITV). Fig. 13 shows the schematic principle of the system. A KrF - Eximer laser (Lambda Physics LPX 100) working with a wavelength of $\lambda = 248$ nm and a pulse duration of 20 ns was used for the investigations. The laser is running always in the High Voltage mode to guaranty stable conditions during the whole measurement. First the laser pulse is spotted on an attenuator which is used to adjust its energy. Out of this, the laser pulse passes a collective lens to focus it and a slit to get a well defined geometry of the laser pulse on the sample. A beam splitter is placed between the slit and the sample. One part of the beam is directed towards the sample and the other part is used to monitor the energy of the laser pulse by means of a pyrometric energy meter (Laser Probe). The ratio between both energies in dependence of the attenuator position (and so the laser energy) was investigated by placing a second power meter at the original position of the sample. The measured ratio (c.f. Fig. 14) was used to calculate the real energy of the laser pulse of the sample surface. The size of the laser spot on the sample surface was also measured to calculate the energy density of the sample surface. The sample is glued and contacted on an eight pin chip carrier and connected by a semi rigid cable with an HP 54522A 500 MHz oscilloscope.
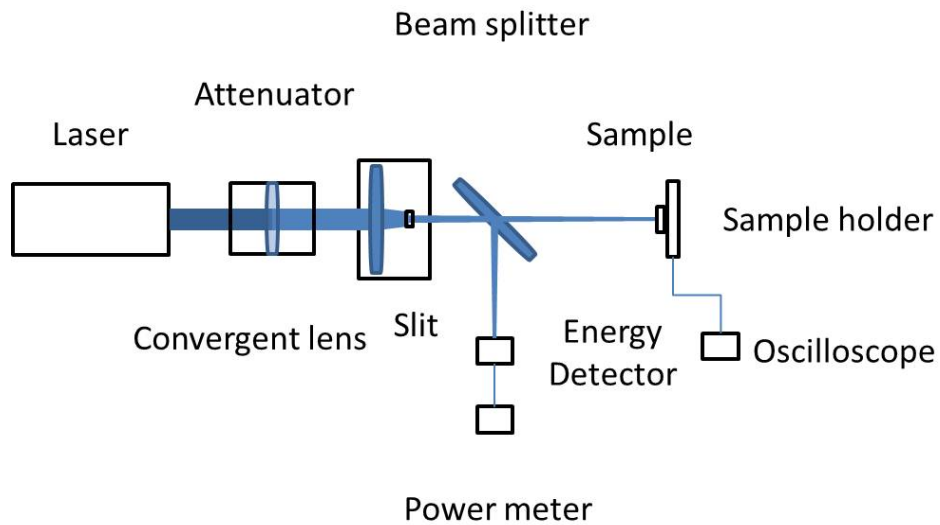
Fig. 13: LITV system with beam line
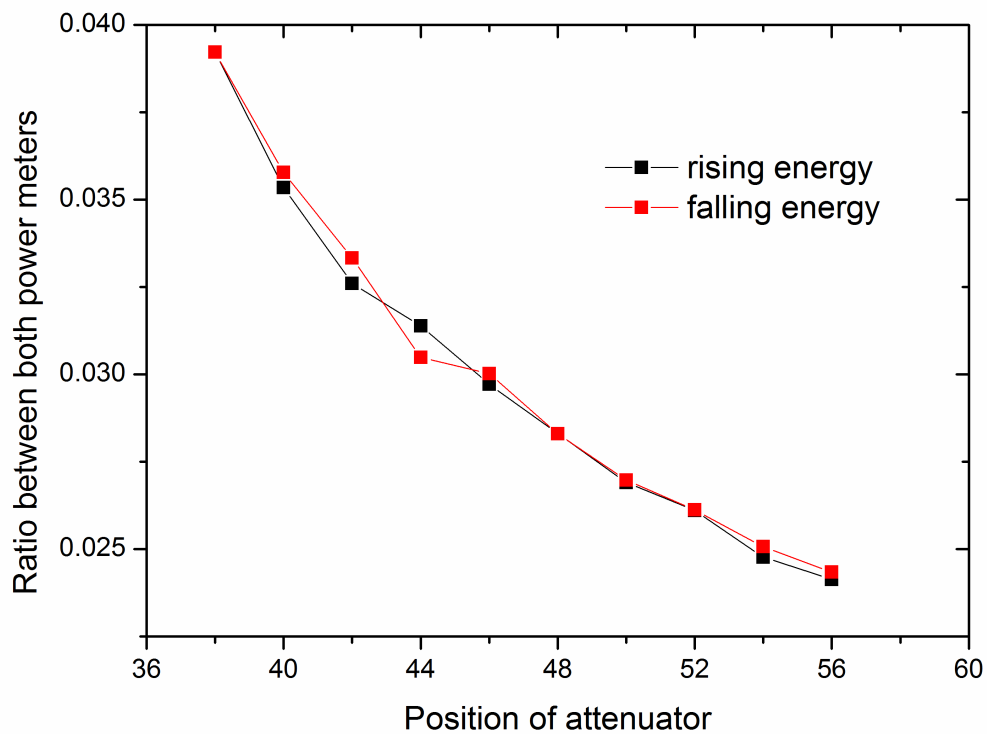
Fig. 14: Ratio of the incoming energy to the sample and the power meter

The oscilloscope is working with an internal impedance R_i of 1 MΩ or 50 Ω. Since the internal resistance of the oscilloscope can modify the measured signal, it is important to verify which internal impedance leads to a realistic result. Therefore a voltage divider (depicted in Fig. 15) was used to investigate the effect of the internal impedance. A pulse generator (output resistance $R_0 = 50$ Ω) and a double variable

resistor were used to simulate a signal U_S from a theoretical sample with a resistance R_S. The pulse generator was adjusted to send a rectangular pulse to the oscilloscope. Between both systems the double variable resistor was installed to change the resistance R_1 of the circuit and to measure its resistance of the parallel resistor. Therefore the absolute voltage of the signal emitted by the pulse generator U_S can be calculated using the signal U_M measured with oscilloscope and the resistances of the pulse generator R_0, the variable resistor R_1 and the internal impedance of the oscilloscope R_i by Equation 24 and Equation 25, respectively.

$$R_S = R_0 + R_1 \qquad\qquad\qquad\qquad \textbf{Equation 24}$$

$$U_S = U_M (1 + R_S / R_i) \qquad\qquad\qquad \textbf{Equation 25}$$
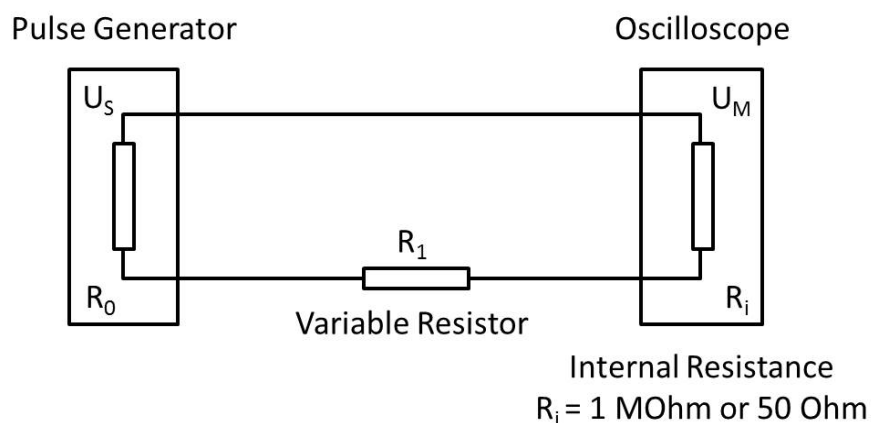
Fig. 15: Voltage divider

The voltages measured by the oscilloscope and the voltages subsequently calculated by Equation 24 and Equation 25 are shown in Fig. 16 in dependence of the resistance R_1. By using a broad range of resistance, it can be clearly seen, that only the measurements with an internal impedance of 50 Ω can reflect the original signal send by the pulse generator. For the internal impedance of 1 MΩ, the measured and the calculated values are completely overlapping. Consequently, the impedance of 50 Ω was used to for all measurements.
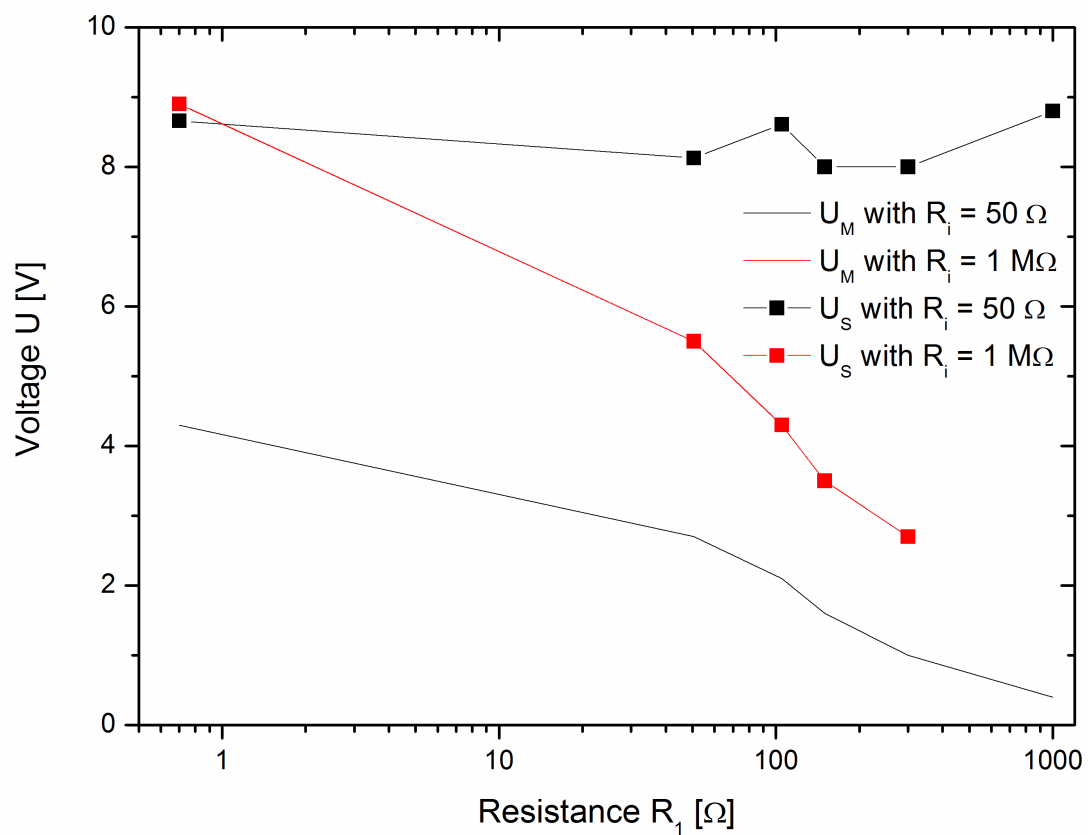
Fig. 16: Measured and calculated voltages in dependence of the resistance R₁

Chapter 5

Results and discussion

This chapter includes the investigations of the Seebeck-coefficient and the electrical resistivity of the relevant materials and material systems as well as their discussion. It covers the studies of $YBa_2Cu_3O_{7-\delta}$, $PrBa_2Cu_3O_7$ and $La_{1-x}Ca_xMnO_3$ (x = 1/3 and 2/3) thin films and the corresponding heterostructures and superlattices. The samples were grown using different growth conditions and different substrates. The measurements were performed in a wide temperature range and partially under applied magnetic fields.

5. 1. Thermoelectric properties of $YBa_2Cu_3O_{7-\delta}$ (YBCO) thin films

The thermoelectric properties of YBCO as a function of oxygen content and doping were widely studied by several groups using single crystals [17, 18, 35, 36], polycrystalline samples [19, 37-49] and thin films [50-52]. The results reported differ from group to group. For optimally doped YBCO ($\delta = 0.05$) values of $S(T) = \pm 2$ µV/K were found between the superconducting transition temperature (T_C) and 300 K. Negative values were reported for overdoped ($\delta < 0.05$) and positive ones for underdoped ($\delta > 0.05$) YBCO, however, the absolute values reported by different groups are also varying. Furthermore the relations between the absolute values of the Seebeck-coefficient and oxygen content or hole doping are different. The reported relations between the oxygen content and the c-axis length determined from XRD measurements are deviating as well. This might result from the different types of samples examined (single crystal, polycrystal and thin film) and their quality.

Several YBCO samples with nominal thicknesses of 1000 Å and 2000 Å were grown in two different PLD systems. The first set of samples (YBCO 1, 2 and 3 in PLD 2) was grown at 730 °C and 0.5 mbar and annealed at 530 °C and 1 bar for 30 minutes in oxygen to generate an optimal oxygen content. The second set of samples

(YBCO 4 and 5 in PLD 5) was grown at 750 °C and 0.27 mbar and annealed at 400 °C and 0.2 mbar for 2.5 hours in oxygen to receive a reduced oxygen content. The results of the XRD investigations indicate the single phase growth of the all samples. Where the samples YBCO 2, 4 and 5 are grown purely c-axis oriented, the XRD pattern of YBCO 1 and 3 exhibits an additional (200) peak arising from grains with the a-axis perpendicular to the surface (c.f. see Fig. 17).
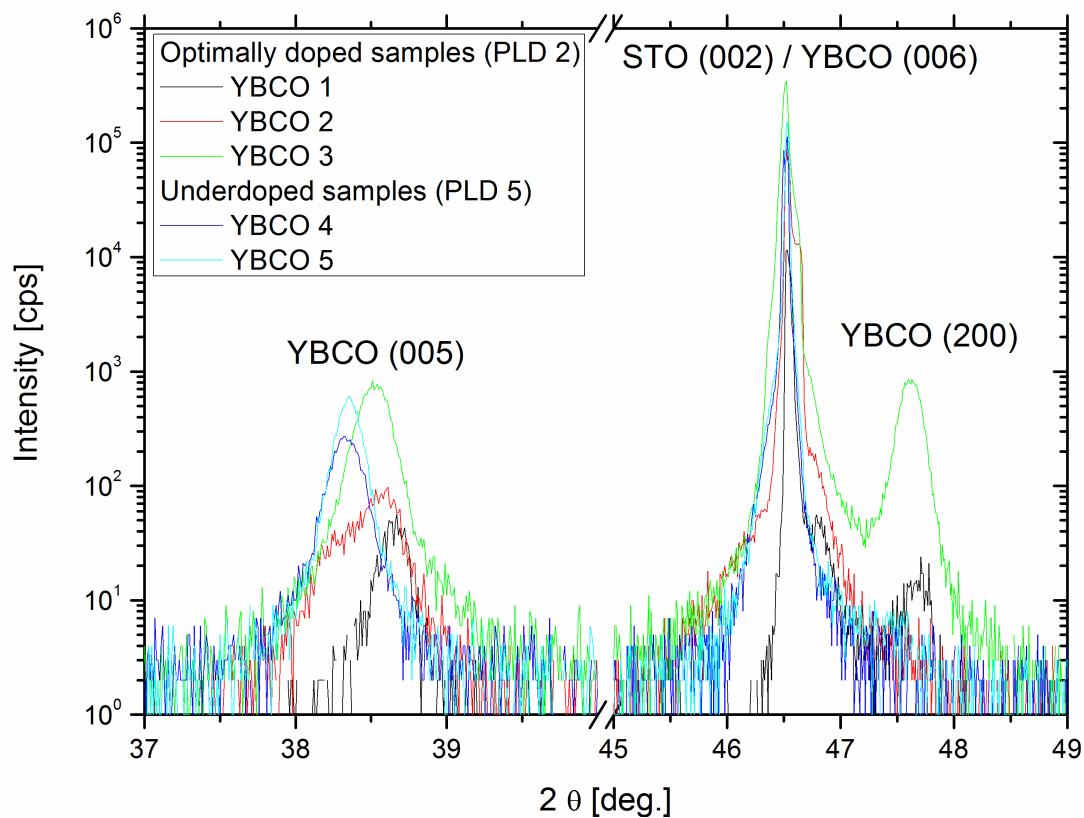

Fig. 17: XRD pattern of the (005) and (006) peak of YBCO with different oxygen content

The c-axis length of the samples was determined from the positions of the Bragg reflections θ from the XRD measurements and applying the Nelson Riley function [33]:

$$NR = \frac{1}{2}\left(\frac{\cos^2\theta}{\sin\theta} + \frac{\cos^2\theta}{\theta}\right)$$

Equation 23

The values of the Nelson Riley function *NR* are plotted with the corresponding c-axis values calculated from the position of the Bragg reflections θ using Bragg's law. The c-axis parameter results from the extrapolation to $NR = 0$ ($\theta = 90$) are shown in Fig. 18. The resulting c-axis lengths together with the standard deviation of the calculation are summarized in Table 2. The error bars of the c-axis ≤ 0.006 Å are small compared to the absolute values. They are neglected for the determination of the oxygen content.
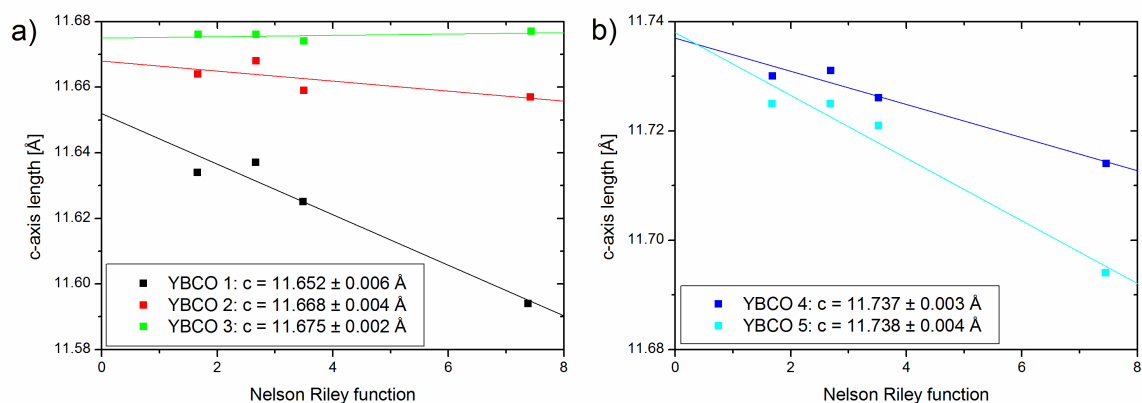
Fig. 18: C-axis values plotted versus the values of the Nelson Riley function for a) nominally optimally doped and b) underdoped YBCO

Since the c-axis length is known to be related to the oxygen content of YBCO it can be used to estimate δ with reference to Jorgensen et al. [53] and the hole concentration *p* with reference to Liang et al. [54]. Jorgensen et al. investigated the relation between c-axis length and oxygen content of polycrystalline samples, whereas Liang et al. examined the relations in single crystalline YBCO samples. Thin films of YBCO with a thickness of around 2000 Å are mainly c-axis textured, but partially they also exhibit an a-axis contribution and defects like stacking faults. Subsequently Jorgensen et al. was used as reference to estimate the oxygen content of the YBCO samples. These values are summarized in Table 2 and Table 3. The samples YBCO 2 and 3 exhibit an oxygen deficiency of $\delta = 0.05$ what corresponds to an optimal doping, whereas YBCO 1 seems to be fully oxygenated ($\delta = 0$). The underdoped samples exhibits an oxygen deficiency of $\delta = 0.45$ according to Jorgensen et al. Using Liang et al. as reference, the samples regarded to be optimally doped (in reference to Jorgensen et al.) are overdoped and the oxygen content of the underdoped samples results to $\delta = 0.4$.

Table 2: Properties of YBCO samples

Sample	System	Thickness [Å]	c-axis length with error bar [Å]	T_C [K]	S (290 to 300 K) [μV/K]
YBCO 1	PLD 2	2000	11.652 ± 0.006	74	4.3
YBCO 2	PLD 2	2000	11.668 ± 0.004	86	-0.2
YBCO 3	PLD 2	2000	11.675 ± 0.002	84	-0.8
YBCO 4	PLD 5	1000	11.737 ± 0.003	57	26.5
YBCO 5	PLD 5	2000	11.738 ± 0.004	57	21.1

Table 3: Calculated δ and p values from different properties in reference to Jorgensen et al., Cochrane et al. and Tallon et al.

Sample	System	Thickness [Å]	Calculated δ and p from different properties in reference to:		
			c-axis (Jorgensen)	S (300 K) (Cochrane)	S (290 K) (Tallon)
YBCO 1	PLD 2	2000	0	0.14	0.22 (p = 0.14)
YBCO 2	PLD 2	2000	0.05	0.08	0.06 (p = 0.17)
YBCO 3	PLD 2	2000	0.05	0.07	0.04 (p = 0.18)
YBCO 4	PLD 5	1000	0.45	0.41	0.45 – 0.5 (p = 0.1)
YBCO 5	PLD 5	2000	0.45	0.35	0.45 – 0.5 (p = 0.1)

The Seebeck-coefficient $S(T)$ and the electrical resistivity $\rho(T)$ of the YBCO samples were measured in the PPMS in a temperature range from 20 K to 300 K. Both, $S(T)$ and $\rho(T)$ are zero in the superconducting state. Values unequal to zero, especially in $S(T)$, are systematic errors generated by the measurement system. The superconducting transition temperature T_C is observable in $\rho(T)$, defined as the temperature with zero resistance, which coincides with the temperature where S(T) vanishes (T_C values are summarized in Table 2). $S(T)$ is nearly constant for the nominally optimal doped samples (YBCO 1 to 3) with Seebeck-coefficients of 4 μV/K to 4.5 μV/K for YBCO 1 and – 1 μV/K to 0 μV/K for YBCO 2 and 3. The resistivity of these samples shows a nearly linear temperature dependence and extrapolates to zero resistance at zero K for YBCO 2 and a positive intercept for YBCO 1 and 3. The

behavior of YBCO 2 is known to be typical for optimally doped high purity YBCO [41]. The positive intercept is regarded to be arising from oxygen deficiency and lattice defects.
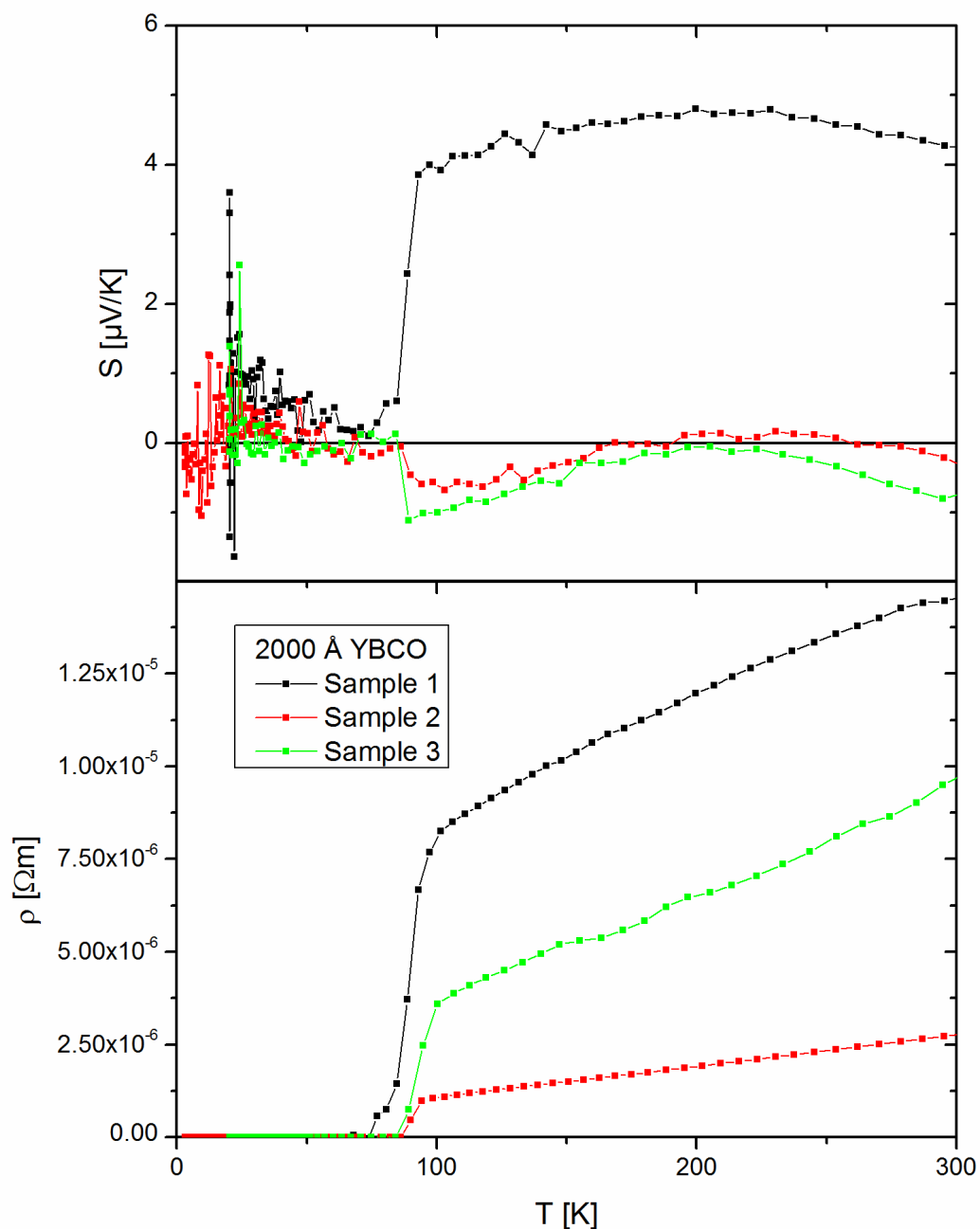

Fig. 19: Seebeck-coefficient and resistivity of YBCO 1, 2 and 3

The measured Seebeck-coefficients are similar to results reported earlier. Ma et al. [50] reported small positive values (0.2 µV/K to 2 µV/K) for dc magnetron sputtered films, but they supplied no information about the oxygen content. Thus, one can not

exclude an oxygen deficiency in these samples. The same values for dc magnetron sputtered films were reported by Cornejo et al. [51]. In addition, they studied laser ablated thin films and found small positive and negative values (± 2 µV/K). From their results they conclude that the Seebeck-coefficient is negative for $\delta \leq 0.08$ and positive for $\delta \geq 0.08$, which is in a good agreement with our findings for YBCO 2 and 3. The results also perfectly agree with the investigations of the $S(T)$ by Cochrane et al. [17] and Shams et al. [18]. They measured the ab-plane of untwinned single crystal YBCO and found small negative values for optimally doped YBCO. The small positive values found in slightly underdoped YBCO ($\delta = 0.11$) are matching with the results of YBCO 1. Cohn et al. [35] measured $S(T)$ in the a- and b-directions of untwinned single crystals and found slightly different temperature dependences of $S(T)$ in both directions. Our results for $S(T)$ can be interpreted as a combination of the $S(T)$ of both directions concerning these results as discussed before.

A contribution from the c-axis is not visible in $S(T)$ due to its high resistivity ($\rho_c \gg (\rho_a, \rho_b)$) according to Kirchhoff's law. So the measured $S(T)$ is composed of $S_a(T)$ and $S_b(T)$. Assuming independent contribution from the copper oxygen planes (CuO$_2$) and chains (CuO), the Seebeck-coefficient parallel and perpendicular to CuO chains in given by the following expressions:

$$S_a = S_{PL} \qquad\qquad \text{Equation 26}$$

$$S_b = \frac{2S_{PL}/\rho_{PL} + S_{CH}/\rho_{CH}}{2/\rho_{PL} + 1/\rho_{CH}} \qquad\qquad \text{Equation 27}$$

were S_{PL} and ρ_{PL} indicates the transport properties of the CuO$_2$ planes and S_{CH} and ρ_{CH} indicates the transport properties of the CuO chains. For c-axis oriented grown thin films the in-plane Seebeck-coefficient yields:

$$S_{ab} = \frac{4S_{PL}/\rho_{PL} + S_{CH}/\rho_{CH}}{4/\rho_{PL} + 1/\rho_{CH}} \qquad\qquad \text{Equation 28}$$

A comparison of our results with values of polycrystalline YBCO samples reported by Ouseph et al. [38], Cooper et al. [41] and Cochrane et al. [43] also indicates the optimal doping of our samples. The results also agree with the investigation of Mosqueira et al. [44] and Shams et al. [19]. Cochrane et al. summarized the values of three reports [38, 41, 43] to compare them with the oxygen content of the samples. Taking the values of *S (300 K)* (values for *S(300 K)* are given in µV/K) one can estimate the oxygen deficiency of our samples using Equation 29 taken from Cochrane et al. [43]:

$$7 - \delta = 6.92 - (0.0152 \times S) + (0.00011 \times S^2); \quad 6.4 \leq 7 - \delta \leq 7.0 \qquad \textbf{Equation 29}$$

They sum up to $\delta = 0.15$ (YBCO 1), $\delta = 0.08$ (YBCO 2) and $\delta = 0.07$ (YBCO 3) and indicated a small oxygen deficiency of our samples. The differences of these values for δ to those determined from the c-axis are close to the error bar of 0.02 for δ, reported by Cochrane for YBCO 1 and 2.

An alternative possibility to determine the oxygen content from *S (290 K)* was reported in several publications by Obertelli et al. [42], Tallon et al. [45, 46] and Bernhard et al. [47]. They investigated a broad range of cuprate superconductors with different doping and found a general relation between *S (290 K)* (values for *S(290 K)* are given in µV/K) and the hole concentration *p*:

$$\begin{aligned} S_{290} &= 372 \exp\left(-32.4p\right) &&\text{for } 0.00 < p < 0.05 \\ S_{290} &= 992 \exp\left(-38.1p\right) &&\text{for } 0.05 < p < 0.155 \qquad \textbf{Equation 30} \\ S_{290} &= -139p + 24.2 &&\text{for } p > 0.155 \end{aligned}$$

Using Equation 30 the hole concentration sums up to $p = 0.14$ (YBCO 1), $p = 0.17$ (YBCO 2) and $p = 0.18$ (YBCO 3). The oxygen deficiency of the samples can be estimate using the relation between the oxygen deficiency δ and the holde doping p investigated by Liang et al. [54] (c.f. see Fig. 20). They sum up $\delta = 0.22$ (YBCO 1), $\delta = 0.06$ (YBCO 2) and $\delta = 0.04$ (YBCO 3), what reconfirms the estimations of the nearly optimal oxygen content of YBCO 2 and 3 and the reduced oxygen content of YBCO 1.
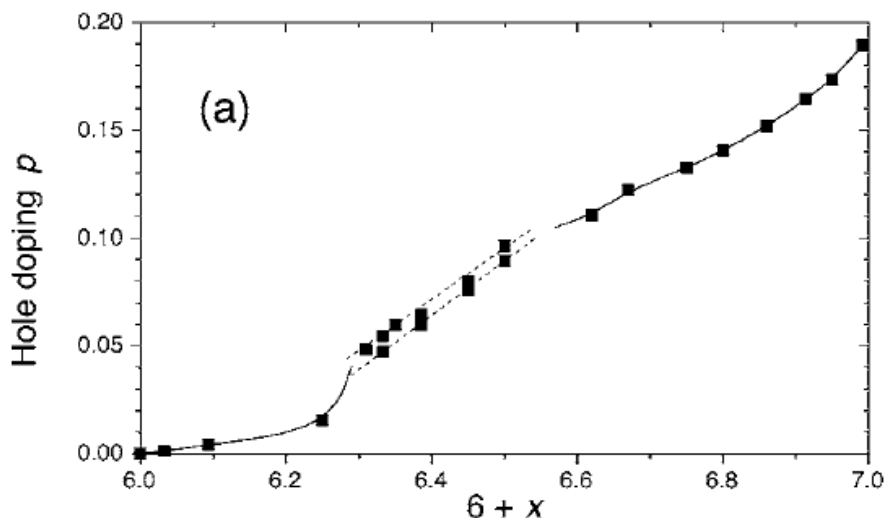
**Fig. 20: Relation between oxygen content δ and hole doping p taken from Liang et al. [54]**

The oxygen content of YBCO 2 and 3 determined using the c-axis are matching with the estimations in reference to Liang et al. using $S\,(300\,K)$ and are similar to the calculation using the relation of Cochrane using $S\,(290\,K)$. The differences of $\Delta\delta = 0.03$ are regarded to be small and within the error bar. The results for YBCO 1 are strongly deviating from YBCO 2 and 3. These differences might result from a reduced sample quality as seen in the XRD measurements and the reduced T_C.

The $S(T)$ dependence of the underdoped samples differs from samples with an optimal oxygen content (c.f. see Fig. 21 with YBCO 2 as reference). Above T_C, $S(T)$ increases with rising temperature to a broad maximum and decrease afterwards. This behavior was described by different groups before for thin films [52], single crystals [17], and polycrystalline samples [43, 45-47]. The maximum is related to a certain temperature in the pseudogap region of YBCO [14, 47]. T_{max} was investigated before using Hall effect measurements by LeBoeuf et al. [13] and addressed to an onset of a Fermi-surface reconstruction. This reconstruction could be caused by a charge ordering instability according to Ghiringhelli et al. [15].

Calculating the oxygen deficiency of the underdoped YBCO samples, with the same procedure to optimally doped YBCO, amounts to an oxygen deficiency of $\delta = 0.41$ to 0.45 for YBCO 4 and $\delta = 0.35$ to 0.45 for YBCO 5. The higher value of $\delta = 0.5$

evaluated in reference to Liang et al. [54] from Equation 30 is due to a possible ordering of oxygen in the CuO chains. The effect of ordering could be examined using single crystal YBCO with $\delta = 0.5$ and investigate the Seebeck-coefficient of the ordered and the unordered phase.

Measurements with an applied magnetic field parallel to the c-axis of the YBCO layers of 9 T where performed to investigate the shift of T_C and potential changes of $S(T)$ and $\rho(T)$. The results, as depicted in Fig. 21, indicate that neither $S(T)$ nor $\rho(T)$ exhibits a strong magnetic field dependence in the normal state (within the error bar of 5 %). The superconducting transition temperature is shifted to values lower than 20 K for the underdoped samples. So the shift of T_C is larger than 40 K, which is much higher than the shift from 86 K to 75 K for YBCO 2. Also the broadening of the superconducting transition in magnetic fields seems to be more pronounced in the underdoped samples. The onset of the superconducting transition can not be exactly defined from $S(T)$ and $\rho(T)$. The differences of the T_C shift for YBCO with different doping was described before by Ramshaw et al. [55] and Ando et al. [56]. They investigated the resistivity of untwinned YBCO single crystals with different oxygen contents under magnetic fields. Both groups found a strong dependence of the T_C shift with different oxygen contents. The T_C shift is small for optimally doped YBCO, increases to an oxygen content around 6.67 (hole doping between 0.11 and 0.13) and decreases afterwards [55]. The minimum is again connected to a competition between superconductivity and a charge ordered state.
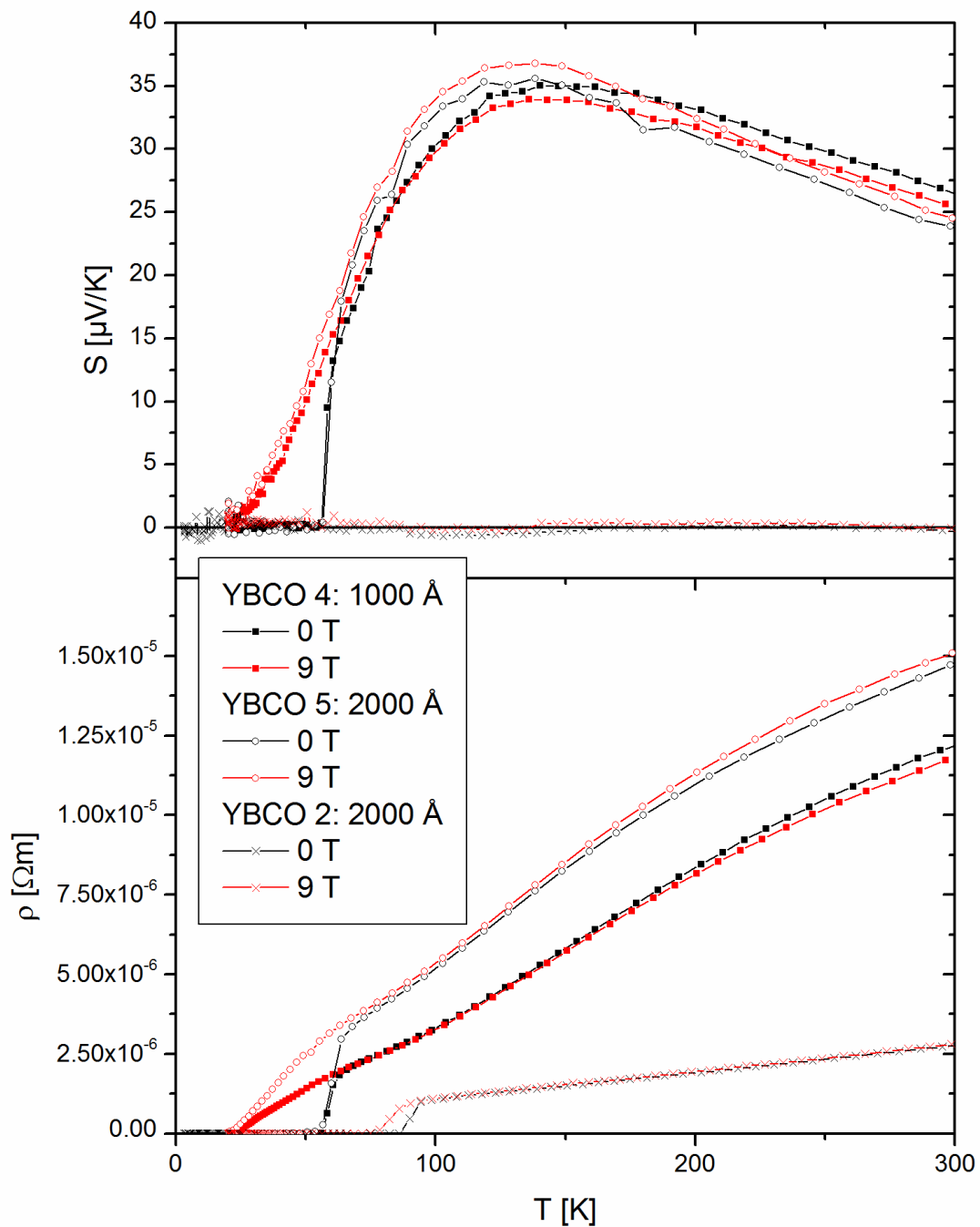
Fig. 21: Seebeck-coefficients and resistivity of underdoped and optimally doped YBCO

Thin films of $PrBa_2Cu_3O_{7-\delta}$ (PBCO) were investigated as an isostructural non superconducting compound of the $RBa_2Cu_3O_{7-\delta}$ (R = Y or a rare earth element) family. It exhibits an orthorhombic crystal structure like YBCO with slightly different lattice parameters. It was investigated as preliminary study to examine the interactions between $La_{2/3}Ca_{1/3}MnO_3$ and a non superconducting cuprate. PBCO was deposited on (001) single crystalline $SrTiO_3$ with a thickness of 2000 Å. The thin

film was grown single phase c-axis oriented with a c-axis lattice parameter of 11.71 Å (lattice parameter was calculated from the position of the (007) Bragg reflection of the XRD measurement) what is exactly matching with the lattice parameter reported by Chryssikos et al. [57]. The resistivity could be measured between 25 K and 300 K and shows insulating behavior (Fig. 22). *S(T)* shows positive values between 50 K and 300 K. It decreases from 50 K up to around 90 K, increases up to 170 K and decreases again. It was impossible to examine the properties at lower temperatures because of the insulating behavior. The insulating behavior shown in the resistivity measurements was reported by different groups in polycrystalline samples before [37, 58, 59]. The measured Seebeck-coefficient differs partially from the results reported earlier [58, 60]. *S(T)* shows an upturn from 90 K to 50 K were other groups reported a decrease of *S(T)* with decreasing temperature in this particular temperature range. The temperature dependence of the Seebeck-coefficient between 100 K and 300 K agrees with the literature. These differences might result from the different strain conditions and / or oxygen contents. Whereas we measured the ab-plane of PBCO, the results presented in the literature express a combination of all crystallographic orientations. It is not clear, if the contribution of the c-axis can be neglected similar to YBCO. Also the possibility of an error, determined by the measurement unit is imaginable. The high resistivity of the sample at low temperatures can cause problems examining the Seebeck-coefficient.
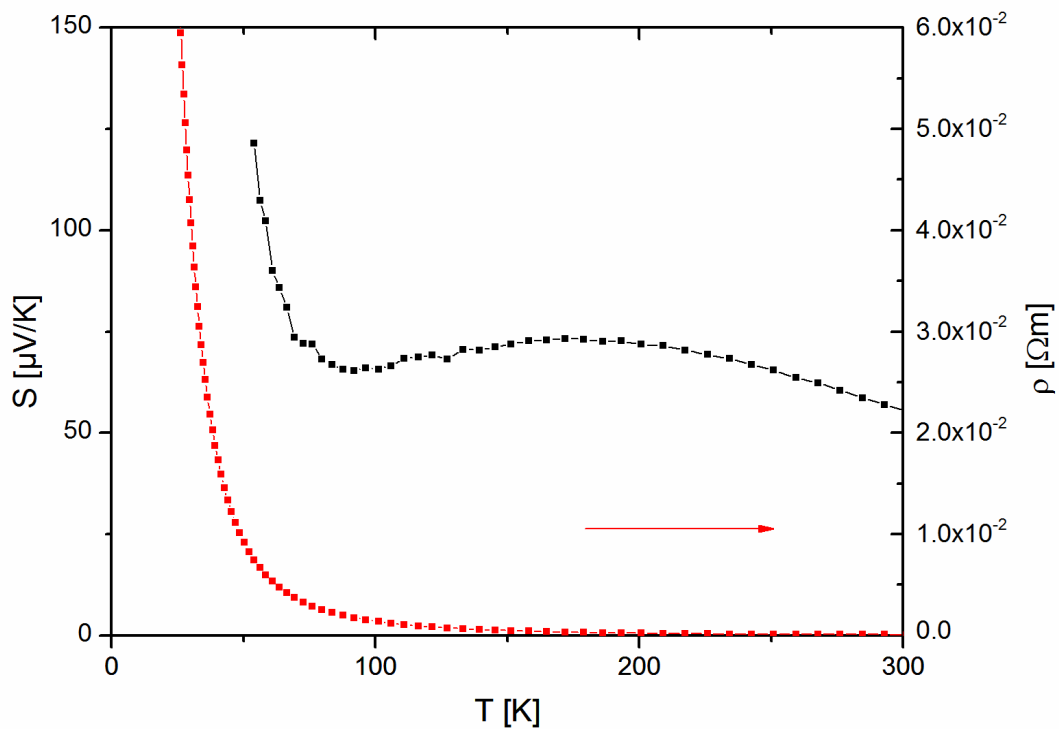
Fig. 22: Seebeck-coefficients (black curve) and electrical resistivity (red curve; arrow indicates the scale for $\rho(T)$**) of PBCO**

In summary, the investigated thin films of YBCO are single phase grown and exhibit mainly the planned oxygen content. Especially the investigations of YBCO 2 shows a nearly perfect match with the values for optimally doped YBCO reported before. The Seebeck-coefficient is small ($S(T) < \pm 2 \, \mu V/K$) for optimally doped and positive for underdoped YBCO. The investigations of PBCO indicate an insulating behavior concerning $\rho(T)$. The temperature behavior is matching the literature values over a wide range, but deviating below 80 K.

5. 2. Thermoelectric properties of La$_{2/3}$Ca$_{1/3}$MnO$_3$ (LCMO) thin films

The investigations of single layer La$_{2/3}$Ca$_{1/3}$MnO$_3$ thin films serve as a baseline for the investigations of the YBa$_2$Cu$_3$O$_{7-\delta}$/La$_{2/3}$Ca$_{1/3}$MnO$_3$ superlattices. The Seebeck-coefficient and the electrical resistivity of samples (nominal thickness of 2000 Å), grown on different substrates (SrTiO$_3$ (STO), (La$_{0.27}$Sr$_{0.73}$)(Al$_{0.65}$Ta$_{0.35}$)O$_3$ (LSAT), NdGaO$_3$ (NGO)) and in different PLD chambers (c.f. see parameters in Table 4), were investigated. The intention of using different substrates was to study possible influences of interfacial strain between substrate and thin film on the transport and magnetic properties of thin films. The samples were grown at 730 °C and 0.5 mbar and annealed at 530 °C and 1 bar for 30 minutes in oxygen. Different targets were used for the ablation (LCMO 1 and 2 from target 1 and LCMO 3 to 4 from target 2). The depositions rates used for the two targets were different, which could result in slightly different growth conditions of the thin films. The crystalline structure of these samples was investigated by X - Ray diffraction analysis (see Fig. 23 for overview and Fig. 24 for details).
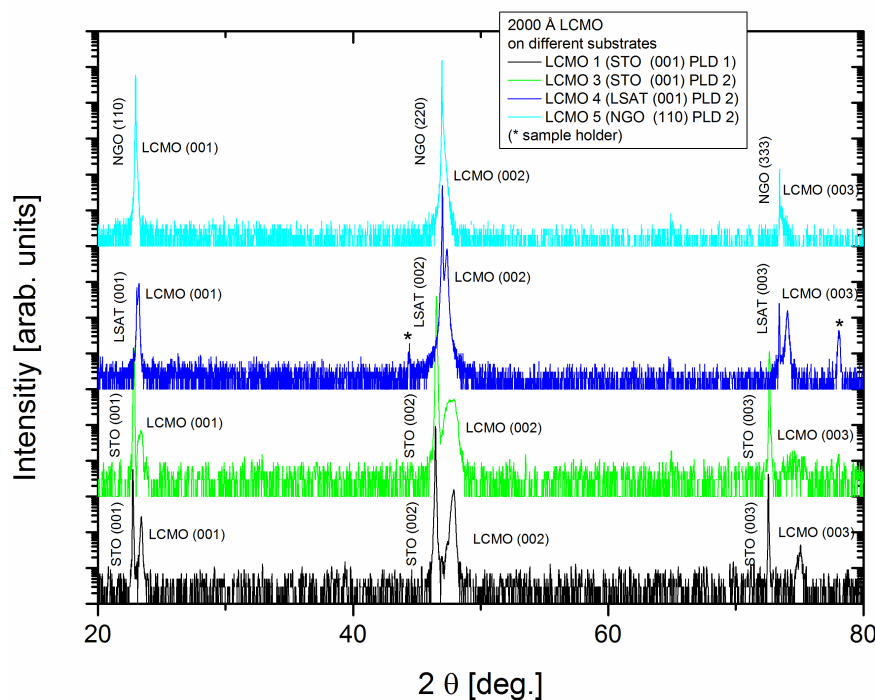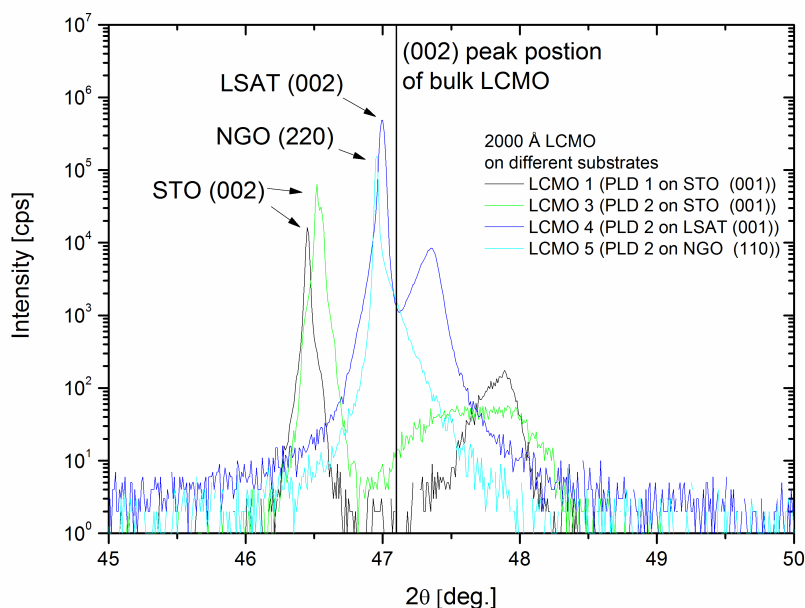

Fig. 23: XRD pattern of LCMO samples on different substrates

Fig. 23 indicates the single phase c-axis orientated growth of all samples. The small peaks around *2θ* equal to 44.5° and 78° (marked as *) are corresponding to the sample holder of the utilized XRD system. Whereas the general features of the different samples are quite similar, a detailed examination of the (002) peak of the LCMO and its position reveals some differences. The samples, grown on STO (a = 3.905 Å) and LSAT (a = 3.868 Å), exhibit a shift of the (002) peak position resulting from a slightly smaller c-axis lattice parameter (*c(LCMO on STO)* = 3.81 Å; *c(LCMO on LSAT)* = 3.84 Å) compared to the literature value of 3.864 Å for bulk material [61]. This is regarded to be due to the biaxial planar tensile strain of the films, resulting in a reduction of the c-axis, provided an elastic deformation takes place. Only the value of the sample grown on NGO nearly matches the literature value because of the nearly identical lattice parameters (*c(NGO)* = *c(LCMO on NGO)* = 3.86 Å).

Fig. 24: XRD pattern of the (002) peak of LCMO on different substrates

The Seebeck-coefficient and the resistivity of five different LCMO samples were investigated in the PPMS in a temperature range from 20 K to 390 K and shown in Fig. 25. In the ferromagnetic state, the Seebeck-coefficient shows small values either slightly positive and negative (± 2 μV/K), whereas in the paramagnetic insulating state, the values are always negative. They amount to values of - 8 μV/K to - 17 μV/K at 390 K. The transition temperature T_{Curie} between both states is indicated

by a change in *S(T)* and a broad maximum in *ρ(T)*; which is nearly matching the Curie temperature investigated by magnetization measurements [62]. Samples grown in PLD 1 exhibit a minimum and maximum around T_{Curie} in *S(T)*. This feature is similar to that found by Jaime et al. [63]. An exact definition of T_{Curie} using *S(T)* is not possible, but one can define it as the middle of both extremes. These temperatures amount to 225 K (LCMO 1) and 210 K (LCMO 2), what differs slightly from the temperatures taken from the maximum of *ρ(T)* of 230 K (LCMO 1) and 220 K (LCMO 2) respectively. Comparing these values with stoichiometric $La_{2/3}Ca_{1/3}MnO_3$ (T_{Curie} = 275 K [64]), T_{Curie} shows a significant shift to lower temperatures. For samples grown in PLD 2, the transition is indicated by a dropdown in *S(T)* to an onset at 275 K (LCMO 3) and 255 K (LCMO 4, 5), respectively. These temperatures are matching with the maximum in *ρ(T)* at 275 K for LCMO 3 and are again smaller for LCMO 4, 5 with 267 K respectively. Thus they are consistent with the literature values.

Table 4: LCMO samples with substrates, lattice parameters and transition temperatures

Sample	System	Substrate with lattice parameter [Å]	Strain and lattice mismatch [%]	Calculated c-axis [Å]	$T_{Curie}(S)$ [K]	$T_{Curie}(ρ)$ [K]
LCMO 1	PLD 1	STO 3.905	tensile 1.07	3.81	225	230
LCMO 2	PLD 1	STO 3.905	tensile 1.07	N.D.	210	220
LCMO 3	PLD 2	STO 3.905	tensile 1.07	3.79 to 3.83	275	275
LCMO 4	PLD 2	LSAT 3.868	tensile 0.11	3.84	255	267
LCMO 5	PLD 2	NGO 3.866	no strain	3.86	255	267
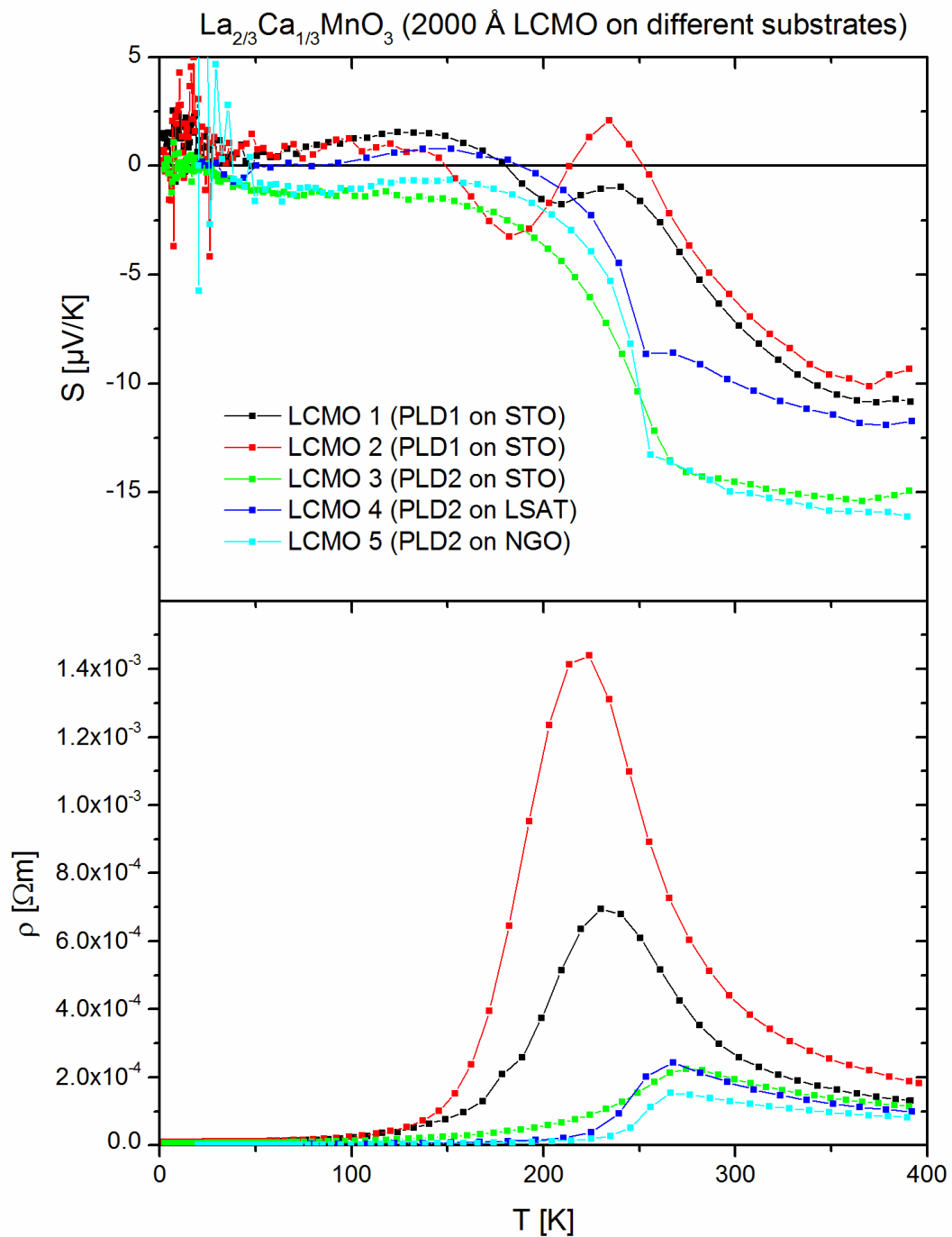
Fig. 25: Seebeck-coefficient and resistivity of all LCMO samples

The results are in a very good agreement with earlier publications of thin film [21, 63, 65] and polycrystalline LCMO samples [22, 24, 66-68]. Most of the reports are dealing with the high temperature behavior in the paramagnetic state. Jaime et al. investigated the thermoelectric and electric transport properties of 600 nm thick laser ablated LCMO films on $LaAlO_3$ substrates [21, 63, 65]. They found a strong

correlation between annealing times and temperatures, the transition temperature T_{Curie} and the Seebeck-coefficient. For the samples with short annealing time they found a reduced oxygen content, therefore a reduced T_{Curie} of 120 K and also a large positive Seebeck-coefficient between 120 K and 230 K ($S(180\ K)$ = 22 µV/K). Longer annealing leads to a small positive $S(T)$ (2 µV/K to 4 µV/K) in the ferromagnetic regime, followed by a minimum and a maximum and results in negative values at high temperatures (350 K). Jaime et al. attributes this behavior to the existence of a stripe structure [63]. This behavior is also observable in the LCMO samples on STO made in PLD 1 in a temperature range from 200 K to 250 K (LCMO 1) and 160 K to 240 K (LCMO 2), respectively (see Fig. 25). These samples are supposed to be oxygen deficient, also indicated by the T_{Curie} reduction to 230 K (LCMO 1) and 220 K (LCMO 2), respectively, in comparison to the transition temperature of optimal doped LCMO of 275 K. Due to the lowered oxygen content the amount of the Mn^{4+} concentration could be reduced leading to a lowered T_{Curie}. A second explanation of the extremes is the existence of two macroscopic phases in this temperature range. This might be due to a variation of the calcium or the oxygen contents in some parts of the thin films. However, there is no evidence of such a macroscopic phase separation in our films.

The $S(T)$ in the ferromagnetic regime can also give information about possible modifications of the oxygen content. A change of $S(T)$ from positive to negative values at a calcium content of approximately 0.3 was investigated by different groups [22, 24, 66]. A change of the oxygen content may also change the transport properties of the LCMO resulting in a shift from negative to positive values even for samples with a nominal doping of calcium of 0.33. These findings were also confirmed by Mandal [66], who investigated the thermoelectric properties of $La_{1-x}A_xMnO_3$ (A = Sr, Ba, Pb, Ca). He attributes the change to positive Seebeck values at low temperatures to a lowered oxygen content. This behavior could be observed in LCMO 1 and 2 and is also slightly visible in LCMO 4 (c.f. see Fig. 25).

Since the conduction mechanism in the paramagnetic phase and the CMR effect are not completely understood till now, different groups [21, 22] tried to use the Seebeck-coefficient to investigate the high temperature conduction mechanism. In strongly

correlated mixed valence systems, the Seebeck-coefficient consists of two parts - the spin part S_σ and the charge carrier part S_c. Assuming a hole hopping from a Mn^{4+} site with a spin state of $\sigma_1 = 3/2$ to a Mn^{3+} site with a spin state of $\sigma_0 = 2$, the spin term amounts to $S_\sigma = -19.2\ \mu V/K$ according to Equation 31:

$$S_\sigma = \frac{k_B}{e}\left(\frac{2\sigma_1 + 1}{2\sigma_0 + 1}\right)$$

Equation 31

where k_B is the Boltzmann's constant and e the electron's charge. The charge carrier part could be used to extract the activation energy from the Seebeck-coefficient (Equation 32). In addition to the activation energy determined from the temperature of the electrical resistivity (Equation 33), one can derive conclusions concerning the conduction mechanism. For temperatures higher than the Curie temperature the $S(T)$ and $\rho(T)$ dependences are described by:

$$S_c(T) = \frac{k_B}{e}\left(\alpha + \frac{E_S}{k_B T}\right)$$

Equation 32

where α is a sample-dependent constant and

$$\rho(T) = \rho_0 T \exp\left(\frac{E_\rho}{k_B T}\right)$$

Equation 33

The activation energies E_S and E_ρ were fitted linearly between T_{Curie} and 370 K (see Fig. 26) and listed in Table 5. The E_S for LCMO 1 and 2 exhibits a large error due to the nonlinearity of $S(T)$. The values at higher temperature were neglected because of an upturn, which is interpreted as an error generated by the measurement system (PPMS). At higher temperatures, the system applies heat to the sample to warm it up to temperatures higher 300 K parallel to the heat pulse which is needed to apply a temperature gradient along the sample. The overlap of these two temperatures can lead to modifications of the Seebeck-coefficient at high temperatures (> 350 K) which are not related to the properties of the samples.

Table 5: LCMO samples with calculated activation energies

Sample	Substrate	$T_{Curie}(S)$ [K]	$T_{Curie}(\rho)$ [K]	E_S [meV]	E_ρ [meV]
LCMO 1	STO	225	230	(8.6)	120
LCMO 2	STO	210	220	(8.3)	125
LCMO 3	STO	275	275	1.5	85
LCMO 4	LSAT	255	267	3.3	95
LCMO 5	NGO	255	267	2.1	75
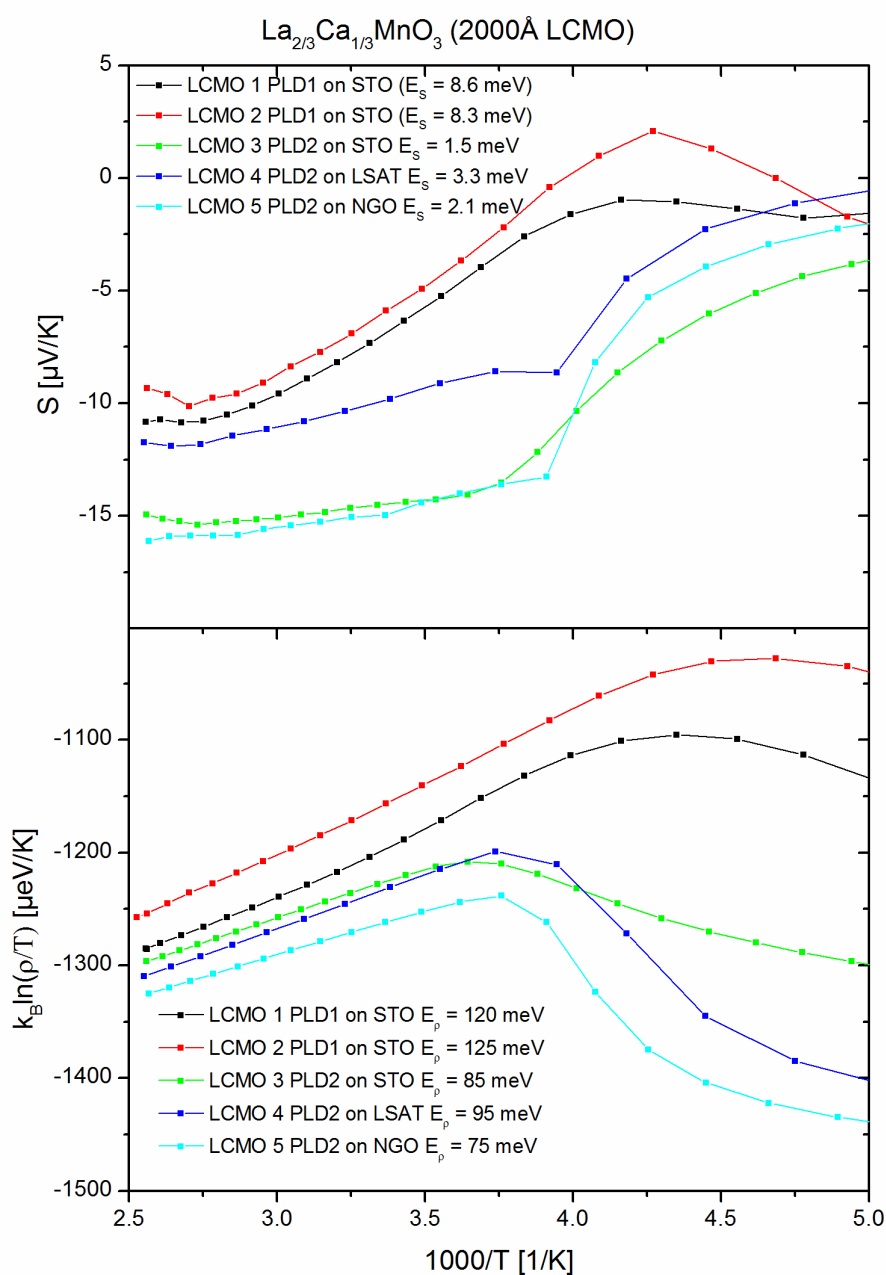
Fig. 26: Calculation of activation energies of LCMO samples (linear fit between T_{Curie} and 1000/T = 2.7 [1/K])

The calculated activation energies are matching the values reported earlier [21, 22]. The large difference between E_S and E_ρ (see Table 5) is a sign of a small polaron formation according to Mott et al. [69, 70]. The larger values of LCMO 1 and 2 compared to the other three samples are again a sign of an incomplete oxidation [22].

Several groups [22, 71] tried to calculate the high temperature limit of the Seebeck-coefficient using Heikes formula [72] and its extension:

$$S_{c,\infty} = \frac{k_B}{e}\left(\frac{1-c_h}{c_h}\right) \quad \text{with} \quad c_h = \frac{[Mn^{4+}]}{[Mn^{4+}]+[Mn^{3+}]}$$

Equation 34

where c_h is the hole concentration and $[Mn^{4+}]$ and $[Mn^{3+}]$ are the manganese concentrations for the specific valences. Hundly et al. [22] extrapolated their experimental values from 325 K and calculated $S_{c,\infty}$ equal to ± 20 µV/K for calcium concentrations larger than 18 %. These values can be simply explained using Heikes formula. They conclude a modification of the Mn^{4+}/Mn^{3+} ratio by excess oxygen or a disproportionation of two Mn^{3+} into one Mn^{4+} and one Mn^{2+} at high temperatures. Buch et al. [71] investigated the Seebeck-coefficient of LCMO with different calcium concentrations between 300 K and 673 K. They measured values of *S(650 K)* of - 20 µV/K and also addressed the results to a modification of the Mn^{4+}/Mn^{3+} ratio by excess oxygen or a charge disproportionation similar to Hundly et al. [22]. An extrapolation to high temperatures from our results was not accomplished, because of the relative low temperature range and the nonlinearity of *S(T)* at high temperatures in our measurements.

The dependence of *S(T)* and *ρ(T)* on a magnetic field of 9 T oriented perpendicular to the thin film surface were measured to receive additional information of the magnetic field dependence of the charge and entropy transport. The behavior of the electrical transport in magnetic fields and the resulting colossal magnetoresistance – effect (CMR – effect) are widely studied [28, 62, 64, 73]. With an applied magnetic field, the maximum in the resistivity is shifted to higher temperatures and the

resistivity is reduced by over hundred percent. Both effects are observable in all LCMO samples.

Less is known about the behavior of $S(T)$ in magnetic fields. A huge magnetothermopower was found by Jaime et al. [65], but only in oxygen deficient LCMO samples. The Seebeck-coefficients investigated with a magnetic field ($S_{9\,T}(T)$) are similar to the values measured without a magnetic field ($S_{0\,T}(T)$) in the ferromagnetic regime (< 150 K) and nearly identical in the paramagnetic state (> 370 K) for all samples, independent on the sign of $S(T)$ (see Fig. 27). For temperatures between 150 K and 370 K, the absolute values of the Seebeck-coefficients of LCMO 3, 4 and 5 are suppressed by the magnetic field. This is caused by the induced magnetic order. The minima and maxima in $S(T)$ found of LCMO 1 and 2 are vanishing by applying a magnetic field. The results can be explained by the presence of two phases as described by Jaime et al. [63]. The suppressions of the minima are consistent with the findings for LCMO 3, 4 and 5, where the reduction in $S(T)$ is caused by the magnetic order. The origin of the suppression of the maxima is not completely understood. If the minima and maxima result from two different phases, the magnetic properties (ground states) of these have to be different. A suppression of positive Seebeck-coefficients by magnetic fields was shown by Jamie et al. [65] for oxygen deficient LCMO. So the origin of the minima and maxima might emerge from two phases with different oxygen contents and magnetic properties.
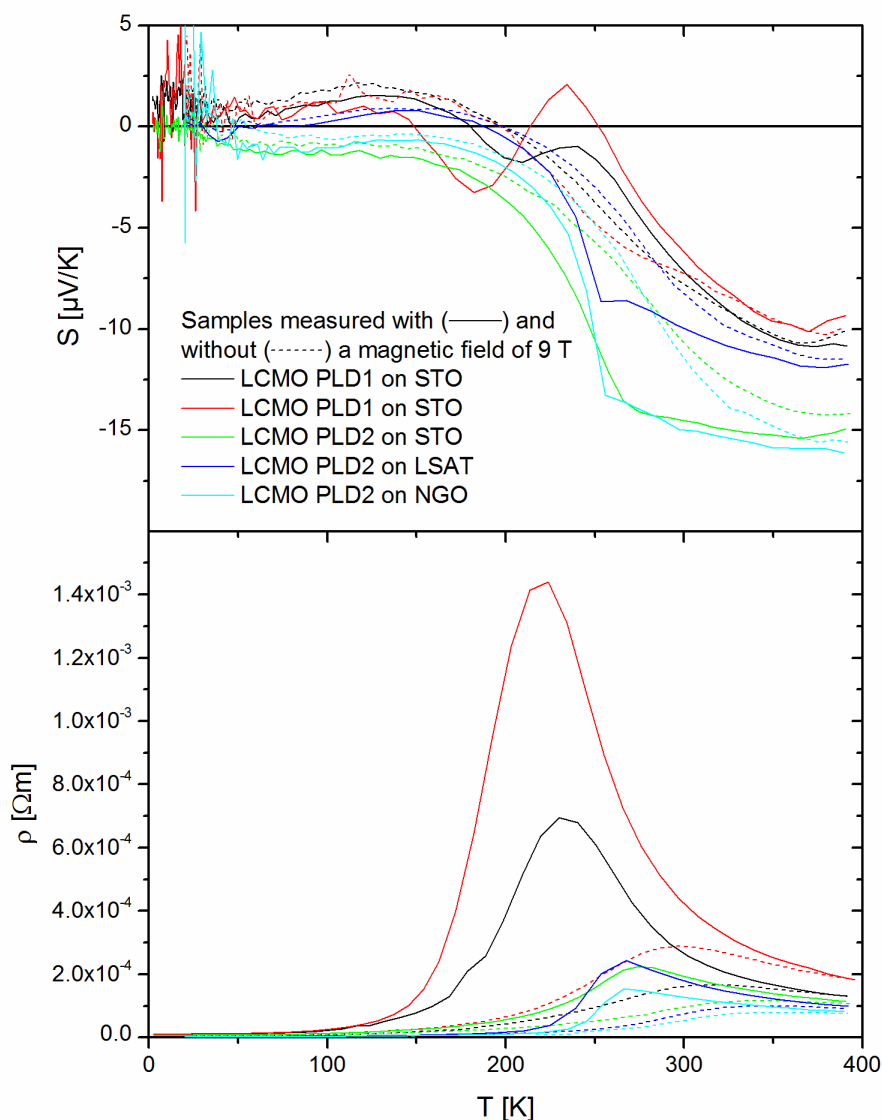
Fig. 27: Seebeck-coefficient and resistivity of all LCMO samples under different magnetic fields

$La_{1/3}Ca_{2/3}MnO_3$ was investigated as an antiferromagnetic insulating (or charge ordered) compound of the $La_{1-X}Ca_XMnO_3$ system. The results are shown in Fig. 28. The measurement was accomplished to compare the properties with $La_{2/3}Ca_{1/3}MnO_3$. The temperature behavior of the resistivity shows an insulating behavior as reported for Ca concentrations $x > 0.5$ [62, 74, 75]. The transition temperature between the paramagnetic and the antiferromagnetic state could not be examined. The Seebeck-coefficient of $La_{1/3}Ca_{2/3}MnO_3$ was studied only at temperatures higher 300 K till now [67]. *S(T)* is positive at low temperatures and decreases to negative values with increasing temperature to a minimum at approximately 185 K. Afterwards it increases with rising temperature to a maximum

at 340 K and decreases with higher temperatures. Both temperatures are not matching with transitions temperatures of 240 K to 260 K reported before [62]. Only the temperature of 214 K, where the curvature of $S(T)$ changes is similar to the transition temperature. Compared to $La_{2/3}Ca_{1/3}MnO_3$, the Seebeck-coefficient of $La_{1/3}Ca_{2/3}MnO_3$ is completely different at temperatures below 340 K. Also the absolute values of - 50 µV/K are much higher compared to $La_{2/3}Ca_{1/3}MnO_3$ with values of less than - 20 µV/K.
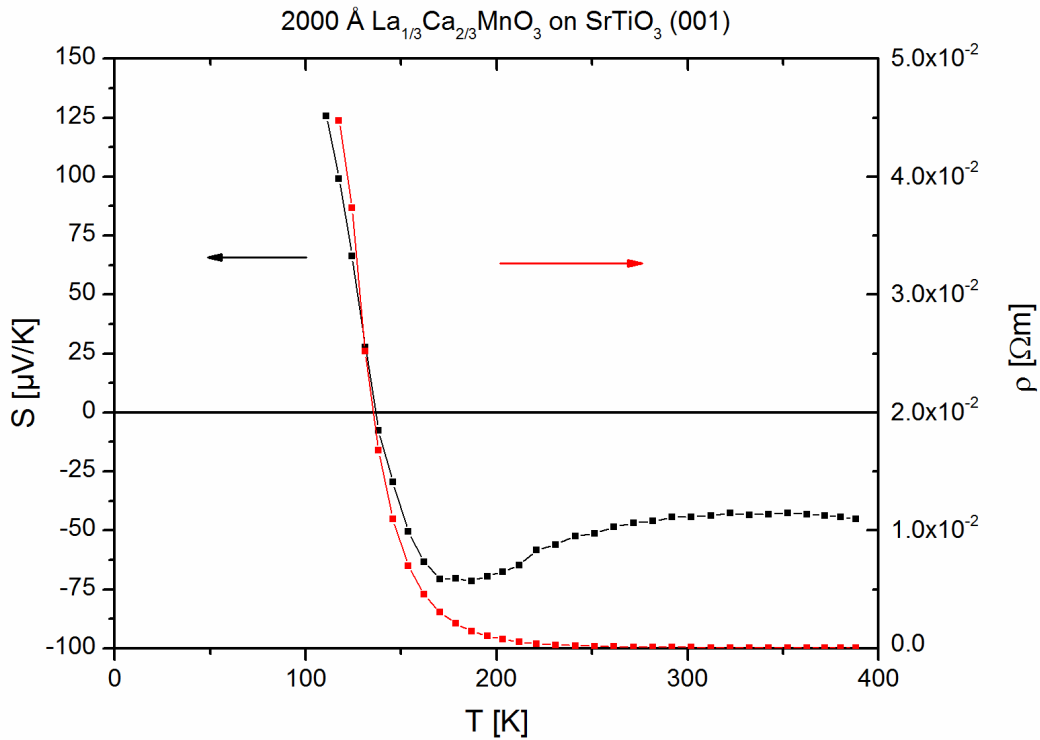
Fig. 28: Seebeck-coefficient and resistivity of La$_{1/3}$Ca$_{2/3}$MnO$_3$

Summarizing the experimental findings, one can claim a phase pure c-axis growth of the $La_{2/3}Ca_{1/3}MnO_3$ samples prepared in PLD 2 from XRD measurements. The transition temperatures T_{Curie} of the samples are not influenced by any substrate induced strain even their lattice parameters are slightly different. The investigations of $S(T)$ and $\rho(T)$ show the phase purity and homogeneity of LCMO 3, 4 and 5 in contrast to LCMO 1 and 2. The calculated activation energies indicate the existence of small polarons in the paramagnetic state. The results are in a good agreement with the literature.

5. 3. Thermoelectric properties of $YBa_2Cu_3O_{7-\delta}$/$La_{2/3}Ca_{1/3}MnO_3$ heterostructures and superlattices grown on $SrTiO_3$

The thermoelectric properties of $YBa_2Cu_3O_{7-\delta}$/$La_{2/3}Ca_{1/3}MnO_3$ heterostructures and superlattices were studied to investigate the interactions between materials with antagonistic long range order of the electronic system such as superconductivity and ferromagnetism. The experiments focus on entropy transport and thus they can be seen as complementary to Hall Effect, electrical transport and optical conductivity measurements. As shown in previous chapters, the Seebeck-coefficient is very sensitive to the charge carrier concentrations in oxide materials that can be adjusted by the oxygen content. Consequently, measurements of the Seebeck-coefficient should give information about the oxygen content in the YBCO and LCMO layers of the heterostructures and superlattices. A modification of the oxygen content in the superlattices or parts of them should be visible in $S(T)$. Additionally, a charge transfer between YBCO and LCMO (holes are moving from YBCO to LCMO) would lead to a change of the charge carrier concentration in both materials. The reduction of the hole concentration in YBCO leads to a positive $S(T)$ similar to oxygen deficiency or cation doped YBCO, for example by replacing Yttrium partially by Praseodymium [37]. A higher hole concentration in the LCMO is comparable with an increase of the Ca content in LCMO and thus an increase of the Mn^{4+} concentration. The thermoelectric properties of LCMO with $Mn^{4+} < 0.5$ are similar to LCMO with $Mn^{4+} = 0.3$. A Mn^{4+} concentration larger than 0.5 would lead to large negative values for $S(T)$ [67]. Thus an effect of a charge transfer would be only visible in the YBCO and not in the LCMO as long as the Mn^{4+} concentration stays smaller than 0.5. The development of an interface between both materials with orbital and magnetic reconstruction could also influence $S(T)$. A direct contribution to $S(T)$ from the interface is maybe barely observable due to its small thickness (~ 20 Å [8]) and high resistivity [5], but the interface can affect the whole layers. Interactions at high temperatures ($T > T_{Curie}$) like electron-phonon interactions [10] can also influence the Seebeck-coefficient.

Heterostructures and superlattices of YBCO and LCMO were grown on (001) oriented STO single crystals in different PLD systems with similar deposition parameters. An overview of the samples with corresponding layer thicknesses and stacking sequence is given by Table 6 and Table 9. The total layer thickness was kept constant (approximately 2000 Å) for all heterostructures and superlattices used for the examination of $S(T)$ and $\rho(T)$ in the PPMS. Also the thickness of YBCO and LCMO layers was always kept equal in these structures. The samples were investigated by XRD measurements to receive information about the sample quality. 2θ - ω scans were used to check the phase purity and to determine the c-axis length. High resolution scans were used to receive information about the interface quality and to calculate the bilayer thickness of the samples. A 2θ - ω scan of one sample (YBCO/LCMO 4) is shown in Fig. 29 as example. It exhibits a nominal bilayer thickness of 260 Å. The real thickness can be determined from the superlattice peaks of the high resolution scan (Fig. 30) and amounts to 310 Å. The deviation from the intended thickness is larger than the expected error of 10 %.

Different approaches were used to estimate the oxygen content of the YBCO layers in the heterostructures and superlattices. The first approach is to use the relations between the c-axis length of YBCO and the oxygen content published by Jorgensen et al. [53] and Liang et al [54]. Since the in plane lattice parameters of YBCO and LCMO are nearly matching, it can be assumed that the unit cell is not elastically deformed. This is confirmed by X-ray diffraction experiments (see below). Consequently, the experimental relation between the c-axis length and the oxygen content can be applied for the heterostructures and superlattices. The second indicator for the oxygen content is the superconducting transitions temperature T_C. But the existing relations between T_C and δ can only be applied for structures were T_C is not suppressed by the ferromagnetic layers. A suppression can be nearly excluded for YBCO thicknesses larger 500 Å, thus the relation can be used to estimate δ for the heterostructures. The relation between T_C and δ can not be applied for the superlattices ($t_{YBCO} < 500$ Å) because of the suppression of T_C reported in numerous publications. The third indicator for the oxygen content of YBCO used in this thesis is the Seebeck-coefficient. Similar to the relations between T_C and δ, the relation between $S(T)$ and δ can only be applied for heterostructres,

were the properties of YBCO are not affected by the ferromagnetic layers. The Seebeck-coefficient of the heterostructures should be nearly identical to the Seebeck-coefficients of single layer YBCO, as discussed in the following chapter.
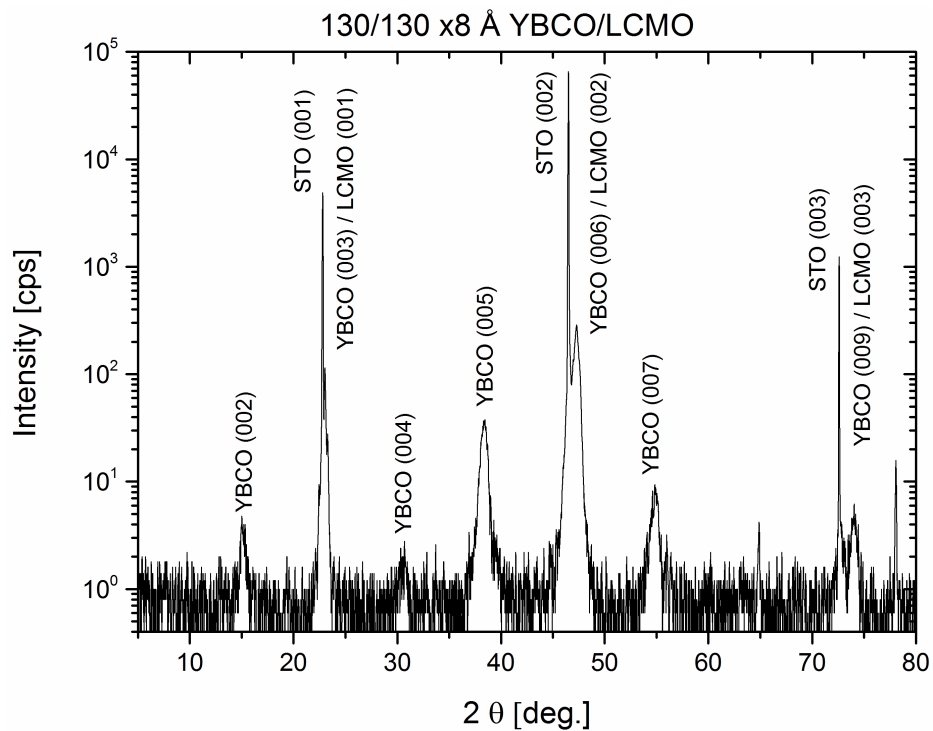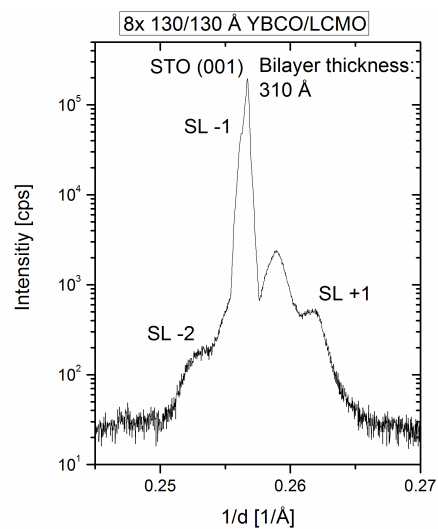

Fig. 29: XRD pattern of YBCO/LCMO 4

Fig. 30: Superlattice scan of YBCO/LCMO 4

5. 3. 1. Thermoelectric properties of YBa$_2$Cu$_3$O$_{7-\delta}$/La$_{2/3}$Ca$_{1/3}$MnO$_3$ heterostructures grown on SrTiO$_3$

At first, several heterostructures of YBCO and LCMO consisting of two to four layers were investigated (c.f. see Table 6). Two samples were grown in PLD 1 with YBCO as first and LCMO as top layer (YBCO/LCMO 1 and 2) at 750 °C and 0.4 mbar and annealed at 490 °C and 1 bar for 30 minutes in oxygen. In addition, two samples with the same stacking sequence (YBCO/LCMO 3 and 4), one sample with LCMO as first and YBCO as top layer and two samples where one material is embedded in the other one (YBCO/LCMO/YBCO and LCMO/YBCO/LCMO) were deposited in PLD 2 with slightly different parameters. The samples were grown at 730 °C and 0.5 mbar and annealed at 530 °C and 1 bar for 30 minutes in oxygen (identical parameters were used for the ablation of YBCO 2 and LCMO 3). Whereas the YBCO target used was the same for all of these samples, the LCMO targets used in PLD 1 and PLD 2 differ. The mechanical density of both LCMO was different which affects the ablation conditions. Different ablation rates were used for both targets, what could lead to different growth conditions for LCMO and thus different properties of the heterostructures.

All samples grow single phase c-axis oriented, according to XRD investigations. The c-axis lengths (together with their error bars) of the YBCO layers in the samples calculated from the position of the Bragg reflections using the Nelson Riley function [33] are listed in Table 6. The error bar of the c-axis length is relatively small, except for YBCO/LCMO 3. The error bar of 0.009 can lead to wrong δ values in the subsequent calculations. Similar to the calculations for pure YBCO, Jorgensen et al. [53] was used as reference for the calculations of the oxygen content because of the YBCO thickness (500 Å to 1000 Å). The estimated oxygen content of YBCO/LCMO 3 was set in brackets, because the large error of the c-axis. Only the sample LCMO/YBCO 1 exhibits a nearly optimal doping. All other samples are regarded to be underdoped with values of δ = 0.16 to 0.23. Using Liang et al. [54] as reference to estimate the oxygen content, leads to different values. Optimal values for δ are only observable for YBCO/LCMO 3 (neglecting the error bar of the c-axis) and

LCMO/YBCO/LCMO. YBCO/LCMO 4 is slightly ($\delta = 0.10$) and YBCO/LCMO/YBCO moderately ($\delta = 0.22$) underdoped in reference to Liang et al. and LCMO/YBCO 1 should be completely overdoped. The estimated value for YBCO/LCMO/YBCO of $\delta = 0.32$ in reference to Jorgensen et al. is far too high even for underdoped samples. The superconducting transition temperature of $T_C = 80$ K of YBCO/LCMO/YBCO is related to an oxygen deficiency of less than $\delta = 0.2$. The estimated oxygen deficiency of $\delta = 0.32$ should coincide with a $T_C < 60$ K. The differences could result from two YBCO layers with slightly different properties. The measured T_C of 80 K could result from a superconducting percolation path in the top YBCO layer of YBCO/LCMO/YBCO. Using Liang et al. as reference for this samples the oxygen content of $\delta = 0.22$ and the transtions temperature of $T_C = 80$ K are nearly matching.

Table 6: Properties of YBCO/LCMO heterostructures with c-axis length with error bar, calculated oxygen content in reference to Liang and Jorgensen and transition temperatures T_C and T_{Curie}

Sample	Thickness [Å]	c-axis lattice parameter of YBCO [Å]	Calculated oxygen content δ		T_C [K]	T_{Curie} [K]
			Jorg.	Liang		
YBCO/LCMO 1	1000/1000	N. D	N. D.	N. D.	58	N. D.
YBCO/LCMO 2	2x 500/500	N. D	N. D	N. D.	68	N. D.
YBCO/LCMO 3	1000/1000	11.691 ± 0.009	(0.17)	(0.05)	61	264
YBCO/LCMO 4	2x 500/500	11.699 ± 0.004	0.23	0.10	61	271
LCMO/YBCO 1	1000/1000	11.663 ± 0.003	0.03	-	86	(255)
LCMO/YBCO/LCMO	700/700/700	11.688 ± 0.002	0.16	0.03	74	255
YBCO/LCMO/YBCO	700/700/700	11.714 ± 0.003	0.32	0.22	80	246

The transport properties of the samples ($S(T)$ and $\rho(T)$) were investigated in a temperature range from 20 K to 390 K and summarized for samples with an even number of layers in Fig. 31 in comparison to single layer thin films. The samples with LCMO as top layer show superconducting transition temperatures, T_C, of 58 K to 68 K, (T_C is defined as zero resistance), which is unexpectedly low. Holden et al. [5] investigated similar structures and found a T_C of 85 K. So the reduction of T_C is maybe not affected by interactions between YBCO and LCMO. Only the sample with YBCO as top layer exhibits a high T_C of 86 K.

The Curie temperature T_{Curie} could not be determined for YBCO/LCMO 1 and 2 because it is not clearly detectable in the transport measurements. The T_{Curie} of YBCO/LCMO 3 and 4 of 264 K and 271 K, defined as maximum temperature in $\rho(T)$, are nearly matching the T_{Curie} of LCMO (267 K to 275 K). Also T_{Curie} of 255 K of LCMO/YBCO 1 is similar to the value of single layer LCMO. Thus the transition temperature of the LCMO in the heterostructures is not modified or influenced by the YBCO layer. Whereas the temperature behavior of the resistivity $\rho(T)$ was reported before [76], the temperature behavior of the Seebeck-coefficient $S(T)$ is completely unexpected for all samples with LCMO as top layer. In contrast, the $S(T)$ behavior of the LCMO/YBCO 1 sample reproduces the same values as YBCO 2. The Seebeck-coefficient of YBCO/LCMO 1 and 2 rises sharply at T_C, followed by a maximum at 135 K and decreases afterwards. This behavior is similar to underdoped YBCO (c.f. see Fig. 32). The maximum is also partially visible in YBCO/LCMO 3 and 4 as buckling at 125 K. Afterwards $S(T)$ increases up to T_{Curie} and decreases with rising temperature. The identical behavior of $S(T)$ and $\rho(T)$ in YBCO/LCMO 1 and 2 and YBCO/LCMO 3 and 4, respectively, can be interpreted as an oxygen deficiency in parts of the heterostructures. If the effect is caused by long range interactions, the results of the samples with two and four layers should be obviously different. So it is evident from these results that the YBCO layers in the samples are not fully oxygenated. An interface effect can be nearly ruled out in these samples because of the small numbers of interfaces (1 to 3) and its volume fraction (interface thickness of approximately 20 Å [8]).

A comparable experiment was done by Lin et al. [77]. They examined the interactions in $YBa_2Cu_3O_7/La_{0.7}Sr_{0.3}MnO_3$ bilayers with different LSMO thicknesses. They also found an enhancement of $S(T)$ in the bilayers compared to single layer YBCO, although the corresponding YBCO film exhibits a $S(T)$ between 13 µV/K and 15 µV/K which is typical for underdoped YBCO.
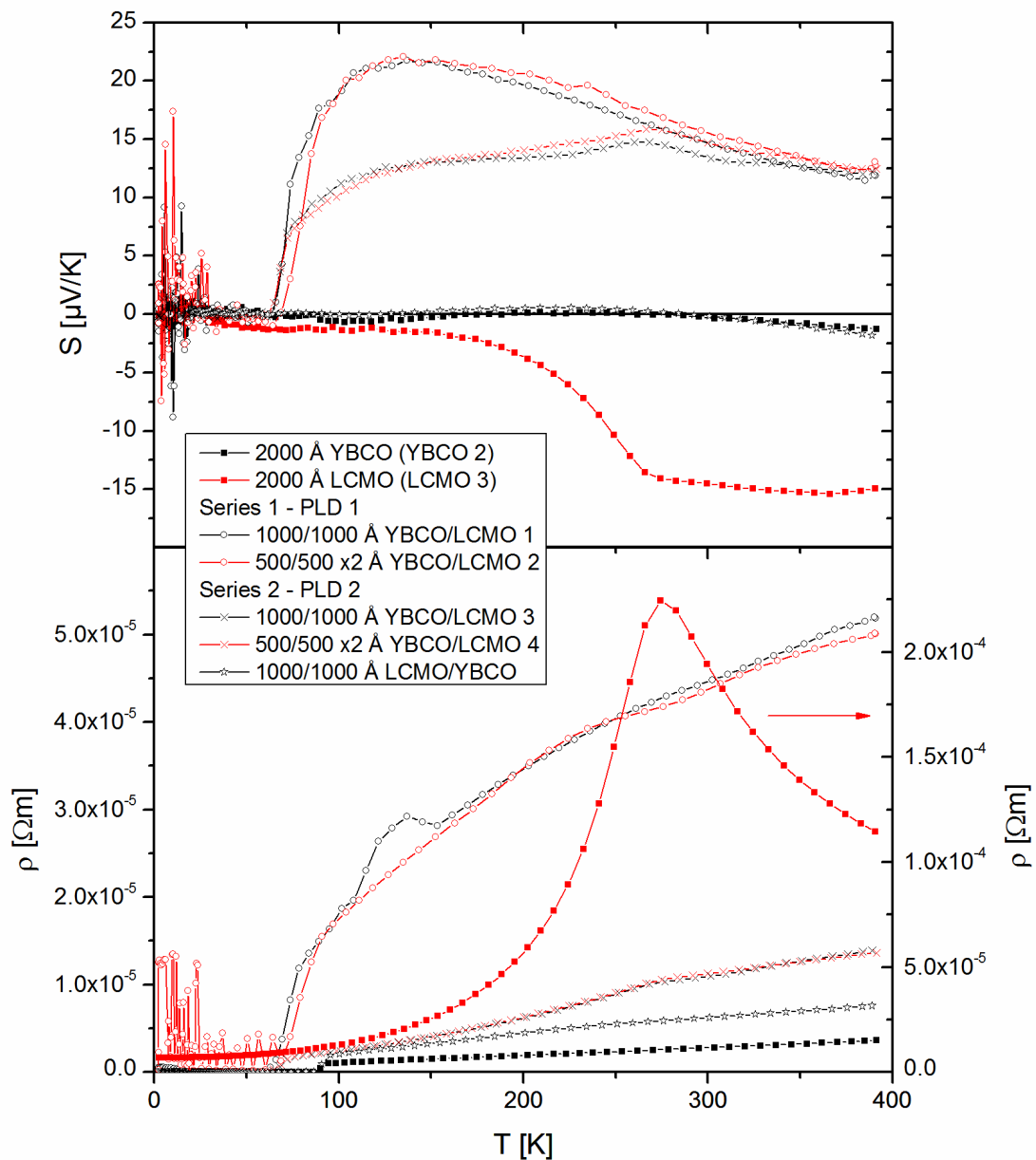
Fig. 31: Transport properties of heterostructures with even number of layers

Calculations of a theoretical *S(T)* of the heterostructures applying Kirchhof's law using the Seebeck-coefficient and the resistivity of optimally doped single layers (YBCO 2 and LCMO 3) should lead to the measured values of the heterostructures. The calculated results are matching with single layer YBCO and LCMO/YBCO 1. This is expected, because of the large differences between the conductivity of YBCO and LCMO (1 to 2 orders of magnitude). Only the calculations with underdoped YBCO and optimally doped LCMO are leading to a *S(T)* behavior similar to the investigated values for the heterostructures YBCO/LCMO 1 and 2. At the end, the

heterostructures with LCMO as top layer are supposed to be partially oxygen deficient.
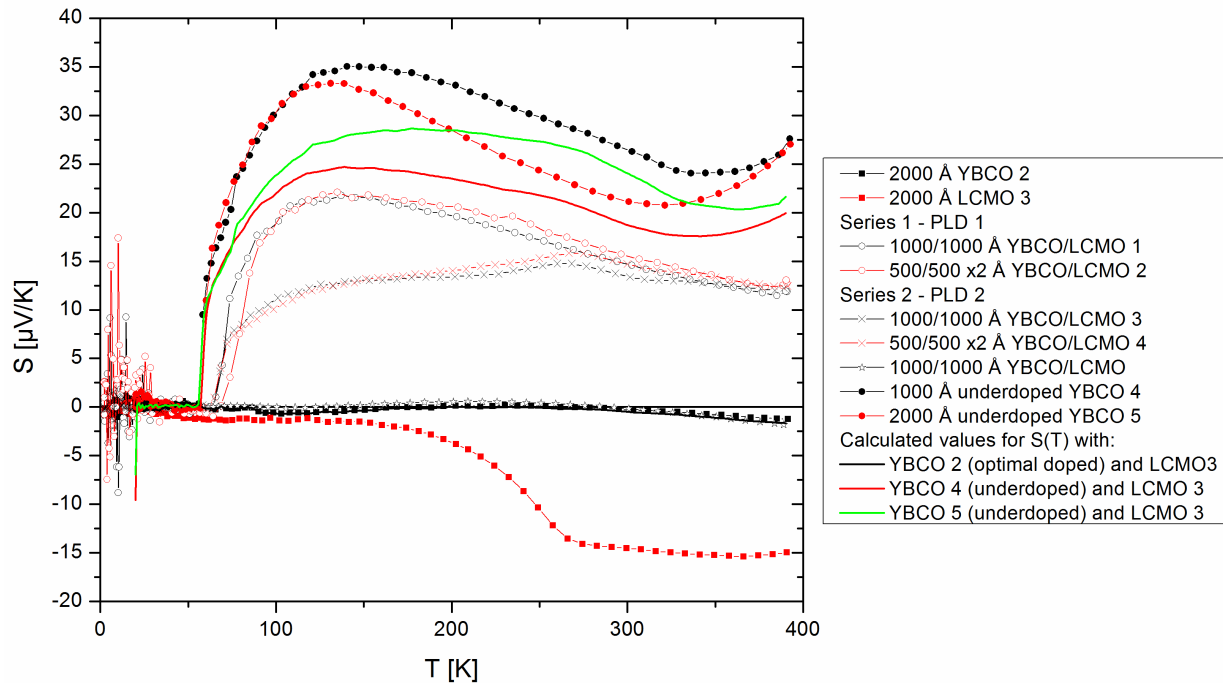
**Fig. 32: Seebeck-coefficient of heterostructures and underdoped YBCO**

To investigate the influence of the first and the top layer of a heterostructures on the results, systems consisting of three layers were investigated. The results of YBCO/LCMO/YBCO and LCMO/YBCO/LCMO in comparison to YBCO 2 and LCMO 3 are depicted in Fig. 33. The temperature dependences of the Seebeck-coefficient of both samples are nearly matching, whereas the temperature dependence of the resistivity strongly deviates. The reduction of T_C for both samples to 74 K and 80 K points in the direction of a small oxygen deficiency in the YBCO layers. Nevertheless, the matching of the $S(T)$ confirms the higher contribution of the YBCO to the measured values compared to the LCMO. Also the results confirm the suggestion, that the Seebeck-coefficient of the whole layer contributes and not only the top layer. The large difference on $\rho(T)$ is an effect of the different volume fractions of YBCO and LCMO in the tri layer systems.
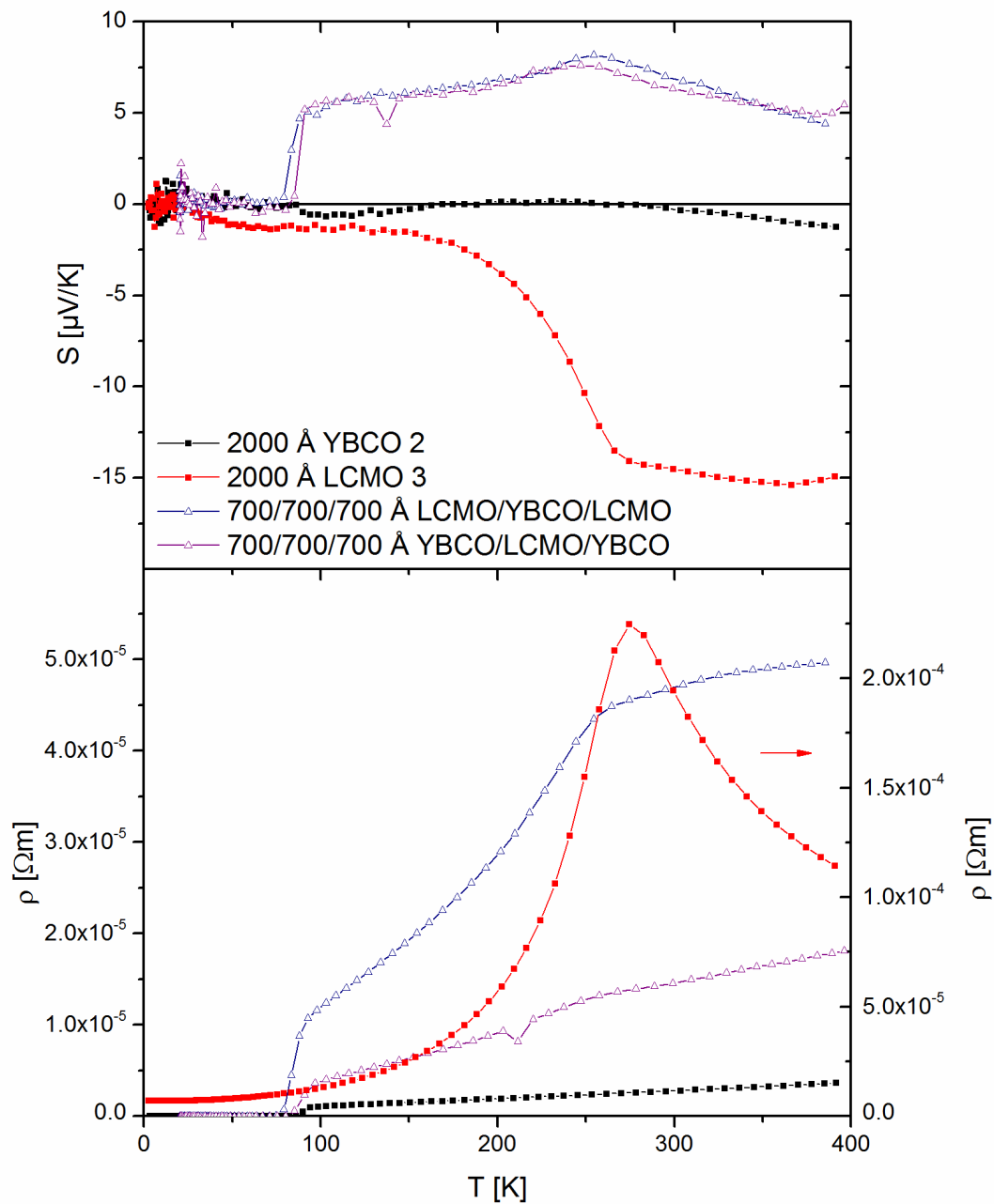
Fig. 33: Transport properties of the tri layers in comparison to YBCO 2 and LCMO 3

An additional series of heterostructures consisting of two layers with 1000 Å YBCO as first and 1000 Å LCMO as top layer was ablated on STO in PLD 5 to receive more information about the thermoelectric properties of the heterostructures. The investigation focuses mainly on the annealing conditions. The samples were deposited at 750 °C in an oxygen atmosphere of 0.2 mbar. The parameters of the subsequent annealing steps accomplished in the PLD system differ between the samples. They are summarized in Table 7.

**Table 7: Annealing conditions of YBCO/LCMO 6 to 10**

Sample	First annealing in oxygen			Second annealing in oxygen		
	Temp. [°C]	Pressure [bar]	Time [h]	Temp. [°C]	Pressure [bar]	Time [h]
YBCO/LCMO 5	530	1	0.5	400	1	15
YBCO/LCMO 6	530	1	0.5	-	-	-
YBCO/LCMO 7	530	1	0.5	400	0.05	16
YBCO/LCMO 8	530	1	0.5	400	0.05	16
YBCO/LCMO 9	-	-	-	-	-	-

The crystallographic properties of the samples were investigated using XRD measurements and the transition temperatures, T_C and T_{Curie}, were estimated using magnetization measurements. Again, the oxygen content was calculated using the c-axis length as described before. The values determined are summarized in Table 8.

Table 8: Properties of YBCO/LCMO 5 to 10 before (upper value) and after (lower value) the measurement in the ZEM-3: c-axis length with error bar and calculated oxygen content in reference to Jorgensen and Liang; transition temperatures T_C and T_{Curie} take from magnetization measurements (values in brakes taken from resistivity measurements) and Seebeck-coefficient

Sample	c-axis lattice parameter of YBCO [Å]	Calculated oxygen content δ		T_C [K]	T_{Curie} [K]	S (390 K) [µV/K]
		(Jorg.)	(Liang)			
YBCO/LCMO 5	11.671 ± 0.002	0.05	-	88.8	180	-2.8
	11.690 ± 0.004	0.15	0.03	90.0 (92.0)	170	0.8
YBCO/LCMO 6	11.697 ± 0.006	0.24	0.08	88.2	170	3.8
	11.694 ± 0.002	0.19	0.05	89.6 (91.9)	160	0.3
YBCO/LCMO 7	11.763 ± 0.002	0.61	0.52	55.4	190	34.0
	11.714 ± 0.004	0.34	0.22	88.2 (91.3)	190	2.2
YBCO/LCMO 8	11.756 ± 0.001	0.58	0.50	47.1	230	53.3
	11.682 ± 0.004	0.09	0.01	88.0 (90.2)	230	-2.8
YBCO/LCMO 9	11.830 ± 0.001	-	-	-	220	31.3
	11.666 ± 0.001	0.03	-	87.5 (90.5)	220	0.0

All samples were measured in the ZEM-3 at an oxygen atmosphere of 950 mbar beginning from 55 °C up to 485 °C (YBCO/LCMO 8 up to 640 °C). The temperature of 485 °C (for YBCO/LCMO 8 640 °C) was kept constant for 10 to 12 hours. The Seebeck-coefficient was measured during this time to monitor possible changes in the samples. Afterwards the sample was measured with decreasing temperature down to 100 °C. The results are shown in Fig. 34. The Seebeck-coefficients at 390 K to the beginning and the end of the measurement are summarized in Table 8. The crystallographic properties as well as the transition temperatures were investigated a second time after the investigations in the ZEM-3. Finally, the samples were contacted to measure the resistance and to monitor the transition temperatures.
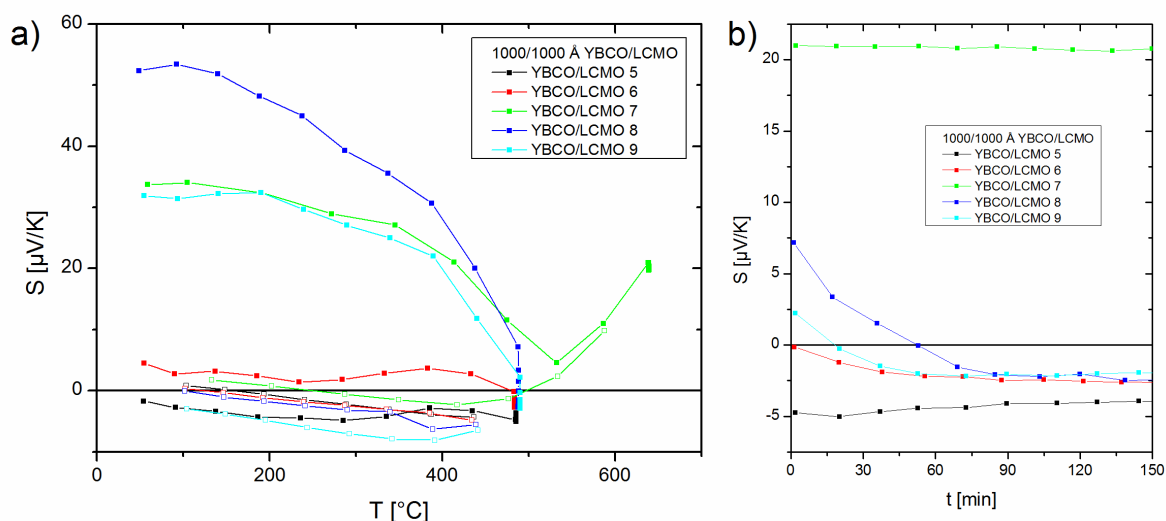
Fig. 34: Seebeck-coefficient of YBCO/LCMO 5 to 10 a) plotted versus the temperature (closed symbols for increasing and open symbols for decreasing temperature) and b) versus the annealing time at 485 °C (for YBCO/LCMO 7 640 °C)

At the beginning of the investigations in the ZEM-3, the Seebeck-coefficients of the investigated samples differ from each other, depending on the annealing conditions. YBCO/LCMO 5 was fabricated with an additional annealing step in contrast to YBCO/LCMO 6. Both samples differ in the crystallographic as well as the thermoelectric properties. Whereas YBCO/LCMO 5 is optimal or slightly overdoped and exhibits an *S(T)* of - 2.8 µV/K, YBCO/LCMO 6 slightly underdoped and exhibits an *S(T)* of 3.8 µV/K. Both samples were modified during the annealing (c.f. Fig. 34). The *S(T)* of YBCO/LCMO 5 and 6 is nearly constant during heating, changes during

the time were the temperature was kept constant 485 °C (*S(T)* of YBCO/LCMO 5 increases and YBCO/LCMO 6 decreases) and exhibits a linear slope during cooling. The properties of both samples are nearly identical after the temperature treatment in the ZEM-3. They are optimally doped, indicated by a $\delta \approx 0.05$ and a $T_C \approx 90$ and 92 K. Also the Seebeck-coefficients of 0.8 µV/K and 0.3 µV/K are nearly the same. The samples YBCO/LCMO 7 and 8 were treated with a second annealing step to reduce the oxygen content of these samples and YBCO/LCMO 9 was deposited without any annealing. The temperature treatment in the ZEM-3 should monitor the recovery of the oxygen content in underdoped YBCO/LCMO samples. All three samples exhibit large positive Seebeck-coefficients of 30 µV/K to 55 µV/K (c.f. Fig. 34) similar to underdoped YBCO with $\delta \approx 0.5$ to 0.65 [42]. *S(T)* decreases with increasing temperature what could be related to a change in the oxygen stoichiometry of YBCO. The Seebeck-coefficient of pure underdoped YBCO should be nearly constant in this temperature range [78]. The upturn for T > 500 °C for YBCO/LCMO 7 is related to the transition to the tetragonal phase [40]. The Seebeck-coefficient of YBCO/LCMO 8 and 9 is also decreasing during annealing, whereas it is stable in YBCO/LCMO 7. The oxygen content of this sample was stabilized while heating the sample up to temperatures higher 500 °C.

The properties of YBCO/LCMO 7 to 9 completely differ after the investigations in the ZEM-3. The calculations of the oxygen content indicated that YBCO/LCMO 7 is underdoped, YBCO/LCMO 8 nearly optimally doped and YBCO/LCMO 9 overdoped. Also the Seebeck-coefficient differ from - 2.8 µV/K to 2.2 µV/K. In contrast, the superconducting transitions temperatures are nearly identical with $T_C \approx 90$ K and 92 K. At the end, the samples YBCO/LCMO 5 to 9 are nearly optimally doped. The differences in the Seebeck-coefficient (- 3 µV/K to 3 µV/K) monitored after the temperature treatment can arise from inhomogeneities in the YBCO layers. Contributions of the LCMO layer could not be determined in the investigations of *S(T)*. The Curie temperature of YBCO/LCMO 5 to 9 is lower compared to the values of 275 K reported earlier [64], but changes in the LCMO caused by the temperature treatment could not be observed.

The investigations of the resistance are shown in Fig. 35. The superconducting transition temperature is clearly visible, whereas the Curie temperature is also not or only hardly observable in the resistance measurements. The resistance of YBCO/LCMO 5 to 7 develops nearly linearly, similar to optimal doped YBCO, without any sign of T_{Curie} and YBCO/LCMO 8 and 9 only show a change in the slope around 220 K related to T_{Curie}. The shape of $R(T)$ in the area of T_C (inset in Fig. 35) illustrates differences between the samples. The transition shown in $R(T)$ is steep and its width is less than 1 K for YBCO/LCMO 5, 7 and 8 and 2 K for YBCO/LCMO 9. Only YBCO/LCMO 6 shows a larger broadness of 4 K and an inhomogeneous transition, what can arise for inhomogeneity in the YBCO layer.
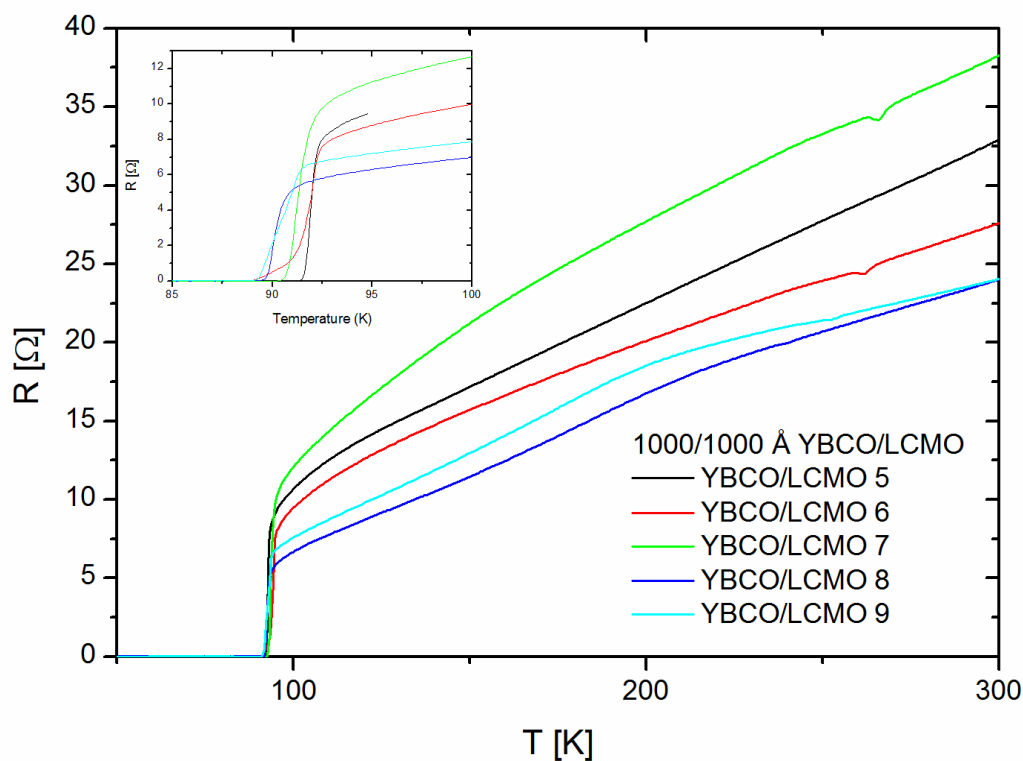

Fig. 35: Resistance of YBCO/LCMO 5 to 9; inset shows a magnification of the area of T_C

Fig. 36 shows the measured superconducting transition temperatures and the c-axis length of YBCO single crystals calculated by Liang et al. [54]. In this graph, the results of YBCO/LCMO 3 to 9 are added. The investigated samples partially match with the findings of Liang et al. The measured transition temperatures are in between 88 K and 92 K for c-axis length between 11.666 Å to 11.714 Å. A maximum in the

relation between T_C and c-axis could not be identified. The profile of the data points can be more described as a plateau. Also Liang et al. are claiming a $\delta = 0$ for a c-axis length of 11.68 Å. In contrast, Benzi et al. [79] found a c-axis length of 11.66 Å for polycrystalline samples of optimally doped YBCO. So the relation between the c-axis length and oxygen content as well as the transition temperature is strongly dependent on the crystallographic properties of the samples.
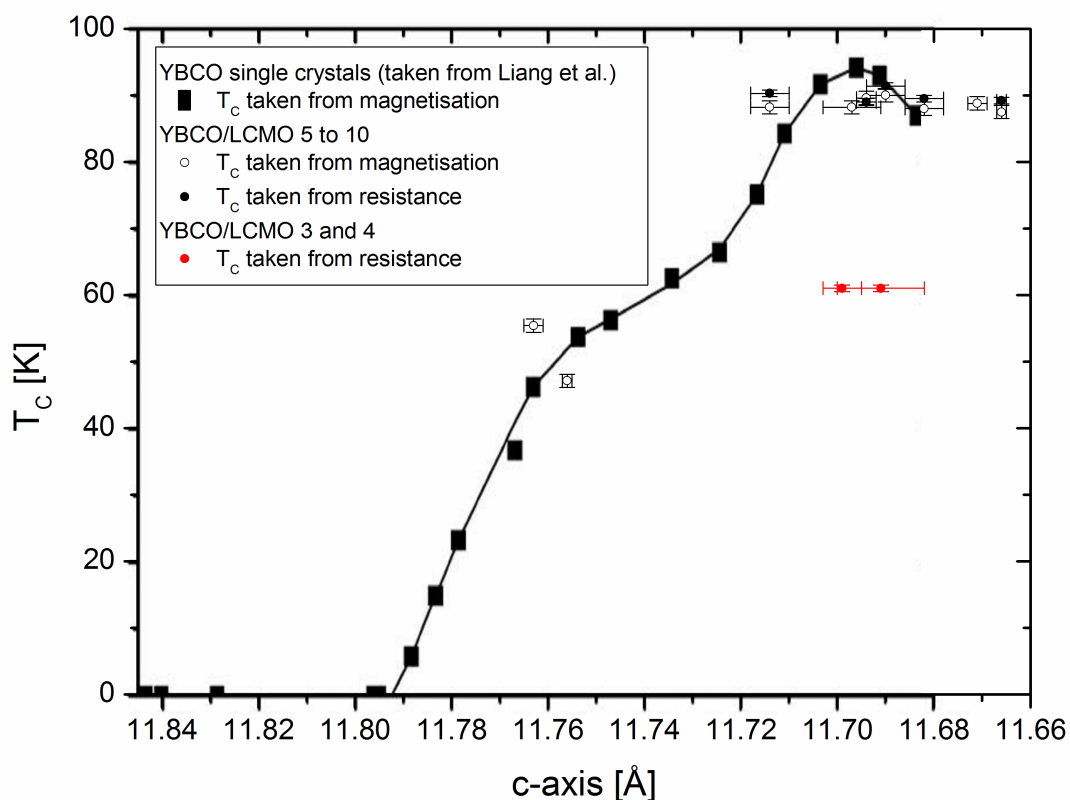

Fig. 36: Superconducting transition temperature versus c-axis length taken from Liang et al. [54] with values for YBCO/LCMO 2 to 9

In comparison, YBCO/LCMO 3 and 4 exhibit a much lower T_C of 61 K with a c-axis length of 11.691 Å and 11.699 Å. Since YBCO/LCMO 3 to 9 exhibits the same thickness, interactions between YBCO and LCMO as a major reason for the T_C reduction in YBCO/LCMO 3 and 4 can be ruled out. Also possible differences in the properties of the YBCO and LCMO targets used in the different systems are not regarded to cause the high differences. The long, additional annealing in the PLD 5 and the ZEM-3 could lead to an optimal oxygen content in contrast to the samples fabricated in PLD 2. These samples are maybe inhomogeneous regarding the oxygen content (as discussed above) what results in similar values for the c-axis but

differences in T_C. The differences are also visible in the absolute values of the Seebeck-coefficient. The measured values of 12 µV/K to 13 µV/K for YBCO/LCMO 3 and 4 are much higher than the investigated values for YBCO/LCMO 6 to 9 (- 2.8 µV/K to 2.2 µV/K). The differences are again a sign of an incomplete oxidation of YBCO/LMCO 3 and 4.

Summarizing the results of the heterostrutures, it turned out at first, that these samples were partially oxygen deficient, depending on the annealing conditions. The Seebeck-coefficients and the superconducting transition temperatures of the heterostrutures can be adjusted, partially independent from the c-axis length of the samples. The buckling of $S(T)$ between 120 K and 150 K examined for YBCO/LCMO 1 to 4 can also be seen as a sign of a incomplete oxidation. Second, it was shown that a simple combination of the properties of YBCO and LCMO according to Kirchhoff's law are dominated by the values of YBCO. The Seebeck-coefficient of the heterostructures is modified by an oxygen deficiency or interactions between YBCO and LCMO, whereas interaction could nearly be ruled out because of the single layer thickness of YBCO and LCMO (500 Å to 1000 Å). But interactions could explain the differences between the experimental results and the calculations using underdoped YBCO. Third it is shown that the Seebeck-coefficient is mainly driven by YBCO in these samples. It was also confirmed, that the measured Seebeck-coefficients are representing the whole system and not only the top layer.

5. 3. 2. Thermoelectric properties of YBa$_2$Cu$_3$O$_{7-\delta}$/La$_{2/3}$Ca$_{1/3}$MnO$_3$ superlattices grown on SrTiO$_3$

Superlattices (SL) of YBCO and LCMO (YBCO/LCMO 10 to 13) were fabricated by Mr. Cristiani in PLD 2 always with YBCO as first layer and LCMO as top layer. The samples were deposited at 730 °C and 0.5 mbar and annealed at 530 °C and 1 bar for 30 minutes in oxygen using the same target for YBCO and different LCMO targets. The samples YBCO/LCMO 10 and 11 were fabricated with one LCMO target and YBCO/LCMO 12 and 13 with a different LCMO target. The different ablation rates used for both targets can result in different growth conditions and properties of the LCMO in the superlattices. To compare the physical properties of the superlattices with the corresponding thin films, the samples YBCO 2, LCMO 3 and YBCO/LCMO 12 to 13 were deposited with the same targets and parameters.

The c-axis length of YBCO, the resulting oxygen deficiency δ and the transition temperatures are summarized in Table 9. The oxygen content was estimated using the data for the c-axis length and T_C of Liang et al. [54] as a reference. The determination of the c-axis length according to the Nelson Rilwey procedure of YBCO/LCMO 10 and 11 exhibits a large error, so the calculated oxygen deficiency of $\delta = 0.35$ and 0.28, respectively, exhibits also a large error. The samples YBCO/LCMO 12 and 13 are regarded to be optimally doped ($\delta = 0.05$).

Table 9: Properties of YBCO/LCMO superlattices investigated in the PPMS

Sample YBCO/LCMO	Thickness [Å]	c-axis lattice parameter [Å]	oxygen content δ (Liang)	T_C [K]	T_{Curie} [K]	S (355 K) [µV/K]
10	4x 260/260	11.725 ± 0.016	0.35	58	245 - 275	9.5 ± 0.1
11	8x 130/130	11.720 ± 0.018	0.28	54	225 - 270	13.9 ± 0.1
12	4x 260/260	11.695 ± 0.003	0.05	68	260	12.2 ± 0.1
13	8x 130/130	11.694 ± 0.007	0.05	59	245	14.2 ± 0.1

The superlattices were measured equally to the single layer materials in a temperature range from 20 K to 390 K. The results of YBCO/LCMO 10 to 13 are shown in Fig. 37 in comparison to YBCO 2 and LCMO 3. Similar to the

heterostructures, T_C as well as T_{Curie} are visible in $S(T)$ and $\rho(T)$ in all samples. YBCO/LCMO 10 and 11 show again a buckling between T_C and T_{Curie} (c.f. see Fig. 31), which can be caused by an oxygen deficiency in the YBCO layers of the superlattice. This finding is supported by the XRD measurement, which also indicates an oxygen deficiency. The temperature behavior can be seen as an overlap of oxygen deficient YBCO and interactions between YBCO and LCMO. In contrast, the Seebeck-coefficient of YBCO/LCMO 12 and 13 is nearly linearly increasing between T_C and T_{Curie} and decreasing from T_{Curie} to higher temperatures. Also, the calculated oxygen deficiency of $\delta = 0.05$ is optimal for these samples. The occurring differences between YBCO/LCMO 10 and 12 and YBCO/LCMO 11 and 13, respectively, are surprising since they exhibit nominally identical structures and were deposited using nearly identical conditions. The different LCMO targets used for the superlattices could cause the differences, even if the Curie temperatures of the samples and the properties of the LCMO layers in the superlattices are similar. The different ablation rates used, leads to a total ablation time of 150 minutes for YBCO/LCMO 10 and 11 and 75 minutes for YBCO/LCMO 12 and 13. It is not clear, if a longer dwell-time of the sample at higher temperatures (730 °C) can lead to modified properties of the superlattices.

As described before, the calculation of $S(T)$ from the single layer properties according to Kirchhoff's law leads to values similar to optimally doped YBCO. Thus one can conclude that the temperature behavior of YBCO/LCMO 12 and 13 is mainly driven by interactions between YBCO and LCMO or the interface between both materials. The interaction can be restricted over an interface region (~ 20 Å [7]) or the mutual influence occurs over the whole layer. These results were already published [80] and are discussed subsequently.
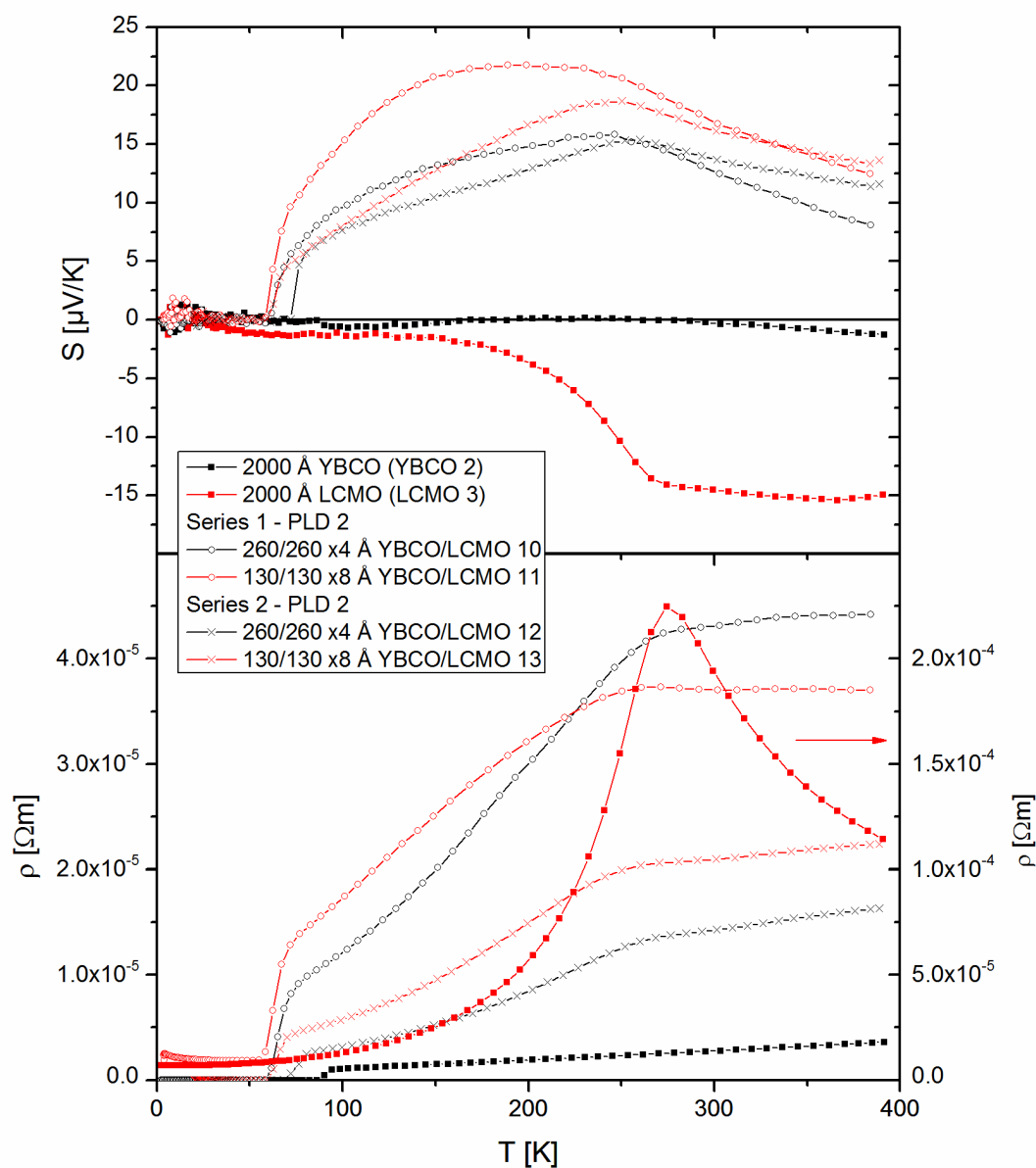
Fig. 37: Transport properties of different superlattices and YBCO 2 and LCMO 3

As reported before, the interface between YBCO and LCMO is more insulating than their neighboring material [5]. But a pure interface effect can be ruled out. The Seebeck-coefficients of YBCO/LCMO 12 and 13 are nearly the same (12.2 µV/K for YBCO/LCMO 12 and 14.2 µV/K for YBCO/LCMO 13), irrespective of the fact that the number of interfaces is more than doubled (7 interfaces in YBCO/LCMO 12 and 15 in YBCO/LCMO 13). Calculating *S(T)* with the physical properties of YBCO 2 and LCMO 3 and adding a possible interface should lead to large differences if the number of interfaces changes dramatically. So the main effect should be generated by an interaction that influences the whole superlattice. Possible modifications of the

interface were reported before [5, 8]. A charge transfer across the interface would change the hole concentration in YBCO and LCMO, whereas the concentration is decreased in YBCO and increased in LCMO. The decrease of the hole concentration in the YBCO would lead, similar to underdoped YBCO, to a positive $S(T)$ and a higher $\rho(T)$, as discussed in Chapter 5. 2. and reported by several groups before [45-47]. The increase of the hole concentration in the LCMO causes an increase of the Mn^{4+} concentration. The $S(T)$ of LCMO would only slightly change and stays small (< - 2 µV/K [22, 24, 66]) in the ferromagnetic state with Mn^{4+} concentrations < 0.5 and negative in the paramagnetic state. Also, changes in the LCMO should not be visible in $S(T)$ because of the high differences in the resistivity (two orders of magnitude) according to Kirchhoff's law. An orbital reconstruction at the interface with a lowered hole concentration in the interfacial Cu orbitals was described by Chakhalian et al. [8]. Similar to a charge transfer, this scenario would have no direct influence on the Seebeck-coefficient since the effect is restricted to a small range. Nevertheless a magnetically or orbitally reconstructed interface could modify the properties of the layers over a long range. Also our results can be explained by a charge ordered state nucleated at the interface. The values of $S(T)$ of the superlattices are similar to pure underdoped YBCO in sign and magnitude, so the differences to optimally doped YBCO could exhibit the same origin. Laliberé et al. [36] addressed these differences to a Fermi surface reconstruction due to a charge ordering instability in underdoped YBCO.

To receive information about the high temperature behavior of the superlattices, the activation energies E_S and E_ρ were calculated using Equation 32 and Equation 33 from Chapter 5. 2. The calculated activation energies using $S(T)$ are nearly matching with the values of single layer LCMO and the values reported by Hundley et al. [22]. So the temperature behavior of the Seebeck-coefficient follows the LCMO, whereas the absolute values are similar to YBCO. If the absolute values are also resulting from LCMO, the activation energies E_S should be much higher (15 to 20 meV [22]). The energies calculated from $\rho(T)$ are much smaller compared to the values of thin film LCMO, thus a temperature dependence of $\rho(T)$ dominated by LCMO can be excluded, what is conclusive with the increase of $\rho(T)$ with increasing temperature.
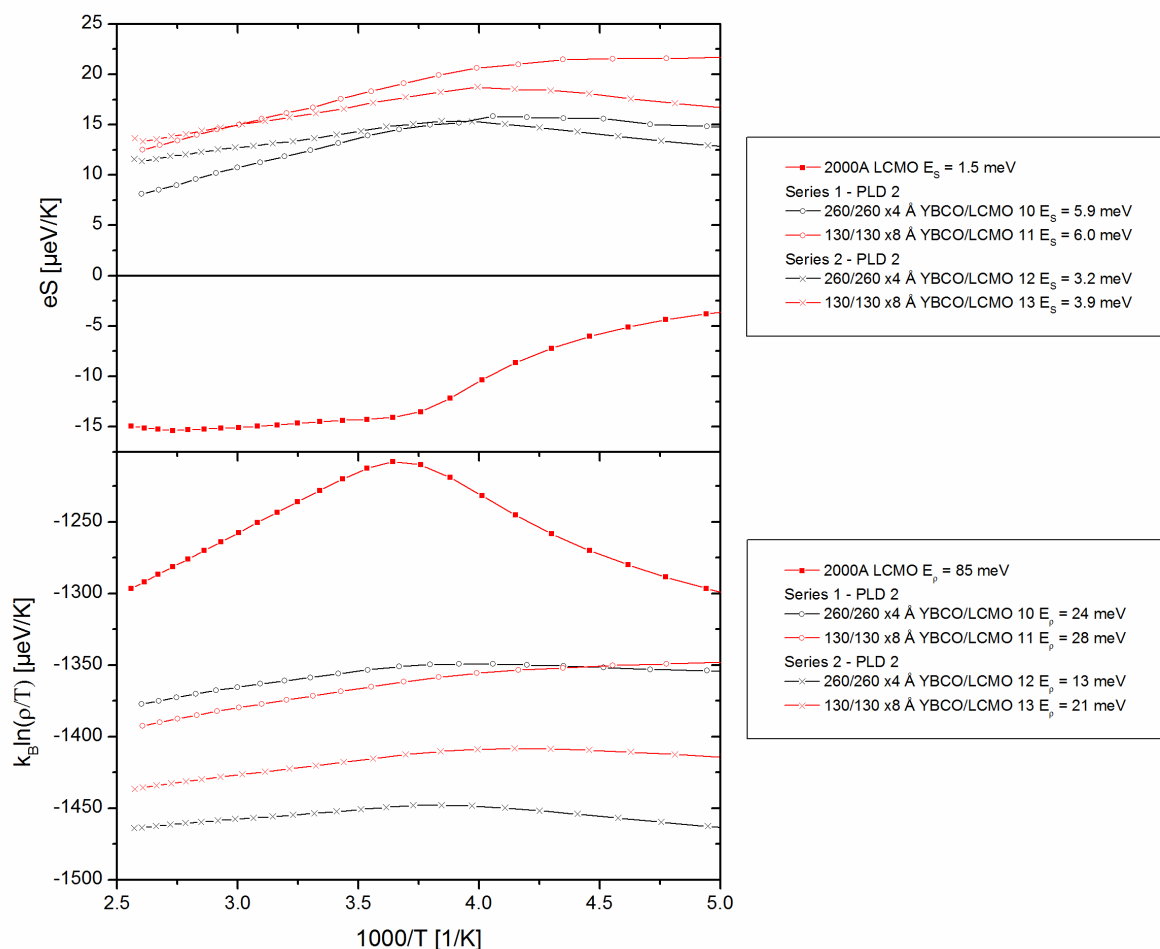
Fig. 38: Calculated activation energies following assumption for pure LCMO

In addition to the samples investigated in the PPMS, a large number of superlattices was fabricated in different PLD systems using similar conditions. They were investigated in the ZEM-3 as comparison for the Seebeck-coefficients at high temperatures (355 K) measured in the TTO for a larger number of superlattices. The values of all samples are also listed in Table 10. These samples were partially investigated by Raman measurements and Reciprocal Space Mapping (RSM) before. The results were published by Driza et al. [[10] including supplementary]. The investigations of the phonon mode around 500 cm^{-1}, which is known to be related to the vibrations of the apical oxygen in YBCO [81], indicates the optimal oxygen content of the YBCO layers. The RSM measurement were accomplished using the (002) and (013) reflections of STO as reference (Fig. 39). The red lines in Fig. 39 indicate the theoretical completely strained and unstrained states of thin films on STO. The LCMO reflection is nearly matching the line indicating a full relaxation.

Also the first and the second satellite peaks can be clearly seen around the (002) and (013) reflections of LCMO. The (006) reflection of YBCO overlaps with the (002) peak of STO. Only the (109)/(019) peak of YBCO is clearly visible near the (013) reflection of STO. At the end, the measurements indicate the strain free grown of the superlattices. Hence the measured effects are not caused by substrate induced or mutual strain.
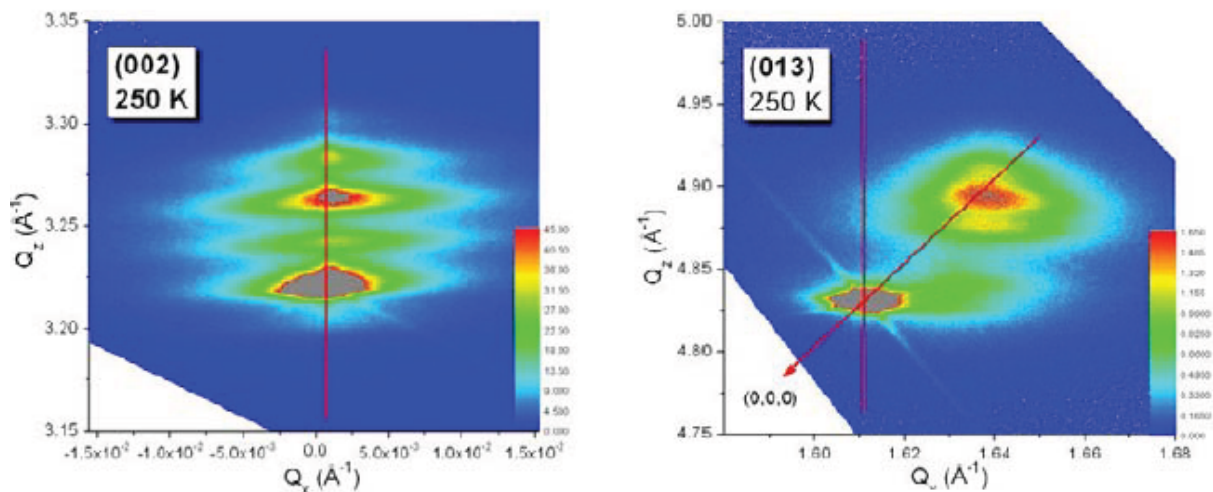

Fig. 39: RMS of a YBCO/LCMO 18 (150/100 x 12 Å YBCO/LCMO on STO) taken from supplementary material of Driza et al. [10]

Table 10: Properties of YBCO/LCMO 14 to 21 (investigated in the ZEM 3)

Sample	Thickness [Å]	T_C [K]	T_{Curie} [K]	S (355 K) [µV/K]
YBCO/LCMO 14	15x 100/100	45	230	18.2 ± 1.3
YBCO/LCMO 15	15x 100/100	N. D.	N. D.	19.2 ± 1.3
YBCO/LCMO 16	5x 100/100	62	240	11.2 ± 0.8
YBCO/LCMO 17	9x 60/60	34	230	15.9 ± 1.1
YBCO/LCMO 18	12x 150/100	48	225	21.5 ± 1.5
YBCO/LCMO 19	12x 150/100	N. D.	N. D.	16.0 ± 1.1
YBCO/LCMO 20	10x 200/100	60	220	17.0 ± 1.2
YBCO/LCMO 21	5x 500/100	82	230	13.5 ± 1.0

Driza et al. investigated mainly the phonon modes of LCMO around 240 cm^{-1} and YBCO around 345 cm^{-1} in a temperature range from 4 K to 300 K and found strong modifications of both phonon modes. The phonon mode of LCMO around 240 cm^{-1} exhibits a strong anomaly at the superconducting transition temperature T_C of the

YBCO and softens at temperatures below T_C [10]. In addition, a hardening above T_{Curie} in reference to single layer LCMO was found. They also investigated a hardening of the phonon mode of YBCO around 345 cm^{-1}. Since these effects were detectable even for samples with a YBCO thickness of 500 Å (YBCO/LCMO 21), they address the findings to long range electron-phonon interactions. The measured Seebeck-coefficients are in a range from 11 µV/K to 22 µV/K, similar to the values of YBCO/LCMO 10 to 13. The large thickness of the YBCO layer in the superlattices (up to 500 Å) confirms the long range character of the interactions. A change in the phonon mode of LCMO at high temperatures can influence the double exchange mechanism and thus explain the differences between the calculated activation energies of LCMO E_S(LCMO) and the superlattices E_S(SL).

The Seebeck-coefficient and the resistivity of two superlattices (YBCO/LCMO 12 and 13) were investigated in a magnetic field to study the magnetic field dependence of the Seebeck-coefficient. A field of 9 T was applied perpendicular to the thin film surface. The results are depicted together with the corresponding investigations without a magnetic field in Fig. 40 with reference to YBCO 2 and LCMO 3.
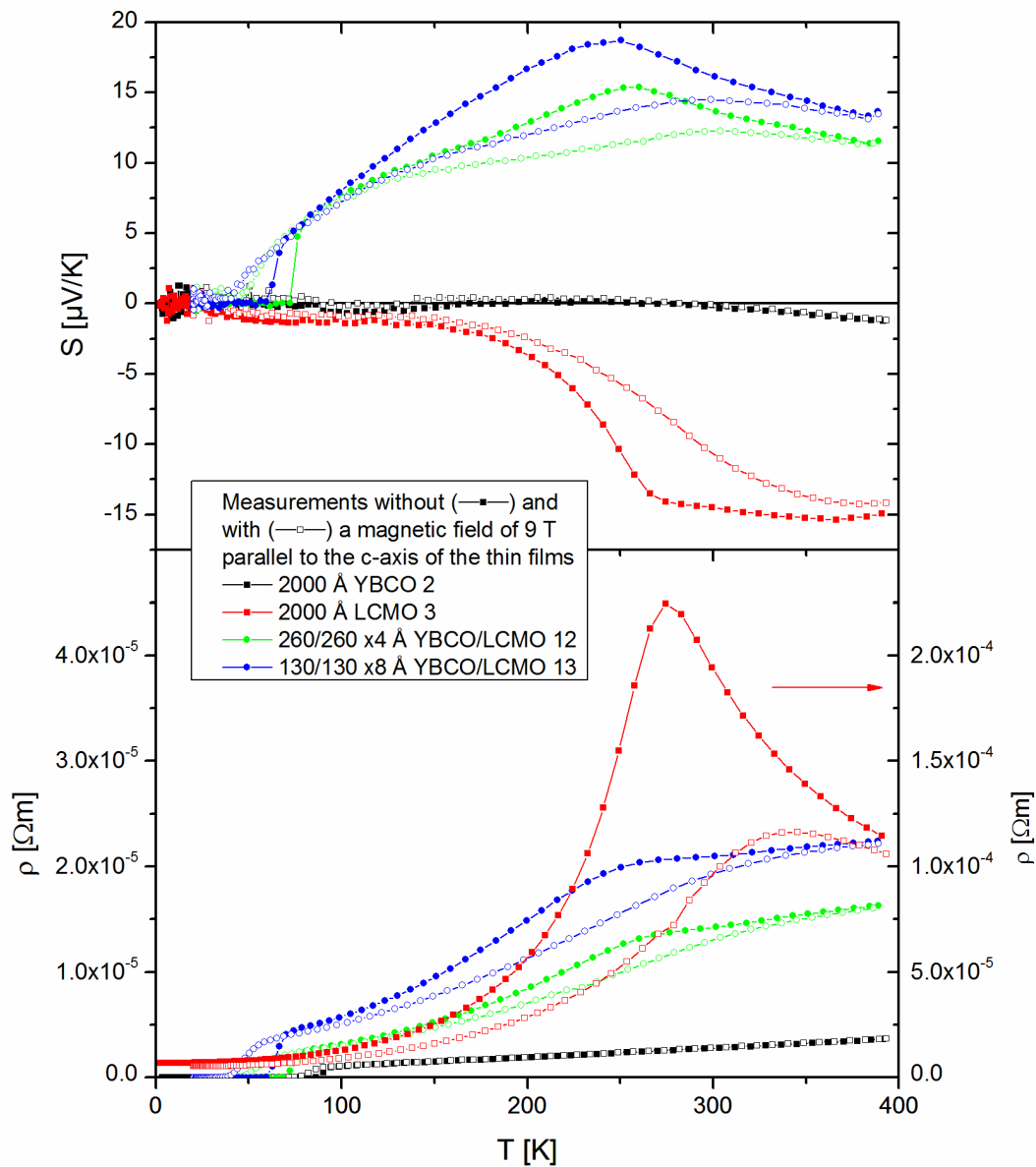
Fig. 40: Seebeck-coefficient and resistivity of YBCO 2, LCMO 3 and YBCO/LCMO 12 and 13 without (closed symbols) and with (open symbols) a magnetic field applied parallel to the c-axis of the thin films

The magnetic field causes a shift of T_C to lower temperatures, similar to pure YBCO and a shift of the characteristic points indicating T_{Curie} to higher temperatures, similar to pure LCMO, visible in $S(T)$ and $\rho(T)$. The absolute values of $S(T)$ and $\rho(T)$ are matching at 68 K for YBCO/LCMO 12 and 59 K for YBCO/LCMO 13 (T_C measured without magnetic fields) and temperatures higher 370 K. In between, both, $S(T)$ and $\rho(T)$ are reduced. Since the magnetic field is not influencing the properties of YBCO in the normal metallic state significantly, the modifications of $S(T)$ and $\rho(T)$ result from modifications of the LCMO layers. The reduction of $\rho(T)$ in magnetic fields was

also measured in LCMO thin film and reflects the colossal magnetoresistance effect in manganite layers. Since the resistivity of the superlattice is mainly driven the YBCO layers, the reduction is much smaller pronounced compared to single layer LCMO. Comparing both superlattices, the reduction of $\rho(T)$ is larger in YBCO/LCMO 13, where the thickness of YBCO and LCMO is reduced by the half compared to YBCO/LCMO 12. A possible coupling between the LCMO layers can be increased by the magnetic field and cause a higher reduction. The decrease of $S(T)$ by a magnetic field can not be simply caused by the reduction of $S(T)$ in LCMO. The direct influence would not be visible according to Kirchhoff's law, because the resistivity of LCMO is still much higher compared to YBCO. Also, the reduction is visible below 180 K, whereas the Seebeck-coefficient is nearly independent from magnetic field at temperatures lower 180 K. Only assuming a strong reduction of the conductivity in the YBCO layers to values in the order of LCMO should lead to sizable effects.

In summary different superlattices consisting of YBCO and LCMO were investigated. The oxygen content and the strain were investigated using XRD and RSM techniques. It was shown, that the samples were strain free c-axis oriented grown. Whereas the heterostructures are partially oxygen deficient, the superlattices exhibits an optimal (YBCO/LCMO 12 to 21 with $\delta \approx 0.05$) or nearly optimal (YBCO/LCMO 10 and 11) oxygen content. The measured values could not be recalculated using $S(T)$ and $\rho(T)$ of single layer YBCO and LCMO using Kirchhoff's law. Only using $S(T)$ and $\rho(T)$ of underdoped YBCO for these calculations result in values similar to the investigated ones in the heterostructures. At the end the measured effects in the heterostructures are mainly resulting from oxygen deficient YBCO, in contrast to the superlattices. The differences in the oxygen content could result from different crystallographic properties of the heterostructures and superlattices. The heterostructures could exhibit a higher crystallinity, with a smaller amount of extended defects like grain boundaries and screw dislocations, compared to the superlattices. Since such defects can act as diffusion path for oxygen, samples with a higher crystallinity (less extended defects) should be annealed for a longer time to achieve an optimal oxygen content. As discussed before, heterostructures could exhibit an optimal oxygen content, if they are annealed over a

long period of time (15 hours). The effects found in the superlattices are resulting from long range interactions between YBCO and LCMO. Also the interfaces between YBCO and LCMO are regarded to exhibit different properties as compared to the single layers. An orbital and magnetic reconstructed interface can influence of the properties of the whole layers in the superlattice over a long range. The properties of the interface itself could not be investigated due to its high resistivity.

5. 4. Thermoelectric properties of YBa$_2$Cu$_3$O$_{7-\delta}$/La$_{2/3}$Ca$_{1/3}$MnO$_3$ heterostructures and superlattices grown on NdGaO$_3$

Single layer thin films of YBCO and LCMO and heterostructures as well as superlattices of both materials were deposited single crystalline (110) oriented NGO. The investigations on an other substrate than STO have been performed to check whether the results found on STO are intrinsic or substrate related. The lattice mismatch between YBCO and (110) oriented NGO is less than 0.3 % in contrast to STO with 1.3 %. Nevertheless, the strain induced by STO will not affect the physical properties of the thin films as shown by Driza et al. [10]. Malik et al. [27] reported about YBCO/LCMO superlattices ablated on NGO (110) and LSAT (001). They used these substrates because the lattices parameters are nearly matching YBCO and LCMO and they are not undergoing any strctural transition below 300 K in contrast to STO. Malik et al. discovered that an additional annealing step is required to achieve a complete oxidation of the superlattices. So they annealed their samples for 12 hours at 485 °C in oxygen in a separate furnace. They correlate the necessity of an additional annealing to the crystalline perfection of their samples. Since the diffusion of oxygen in YBCO is very low and the diffusion coefficients differ between the ab-plane (D_{ab}(760 K) $\approx 10^{-15}$ m²/s) and the c-axis (D_c(760 K) $\approx 10^{-19}$ m²/s) as reported by Tsukui et al. [82] and Michaelis et al. [83], defects acting as diffusion path or longer annealing times are needed for an optimal oxidation of YBCO thin films and superlattices containing YBCO. In samples with lower crystalline perfectness defects like grain boundaries and screw dislocations act as diffusion path for oxygen and accelerate the oxygen diffusion. The absence of these defects requires a longer annealing time. Our sample grown on NGO were ablated using PLD parameters for samples on STO using an additional post deposition annealing step with the parameters reported by Malik et al. [27].

All samples grown on NGO were deposited by Mr. Cristiani in PLD 2 at 730 °C and 0.5 mbar and annealed at 530 °C and 1 bar for 30 minutes in oxygen. The ablation conditions are identical to the samples grown on STO. The targets used for the growth of the samples are the same which were used for fabricating YBCO 2,

LCMO 3 and YBCO/LCMO 12 and 13. The samples were investigated by XRD and RSM measurements to receive information about the oxygen content of the thin films. Afterwards, the samples were annealed using the ZEM-3 in an oxygen atmosphere of 950 mbar at approximately 480 °C for 11 to 12 hours. The conditions used were similar to the parameters reported by Malik et al. [27]. Afterwards, the XRD and RSM measurements were repeated to investigate possible changes due to the annealing. At the end, the Seebeck-coefficient and the electrical resistivity were measured in the PPMS between 20 K and 390 K.

The results of the XRD measurements as well as the RSM investigations are summarized in Table 11. The results of XRD investigations before and after annealing are shown in Fig. 41 and Fig. 42 for YBCO/LCMO 25 as example. All samples ablated on NGO, except YBCO 6, grow single phase c-axis oriented. The films exhibit a high quality with sharp interfaces, indicated by the appearance of superlattice peaks (Fig. 42).

Table 11: Crystallographic properties (bi-layer thickness in brackets) and oxygen content of samples on NGO

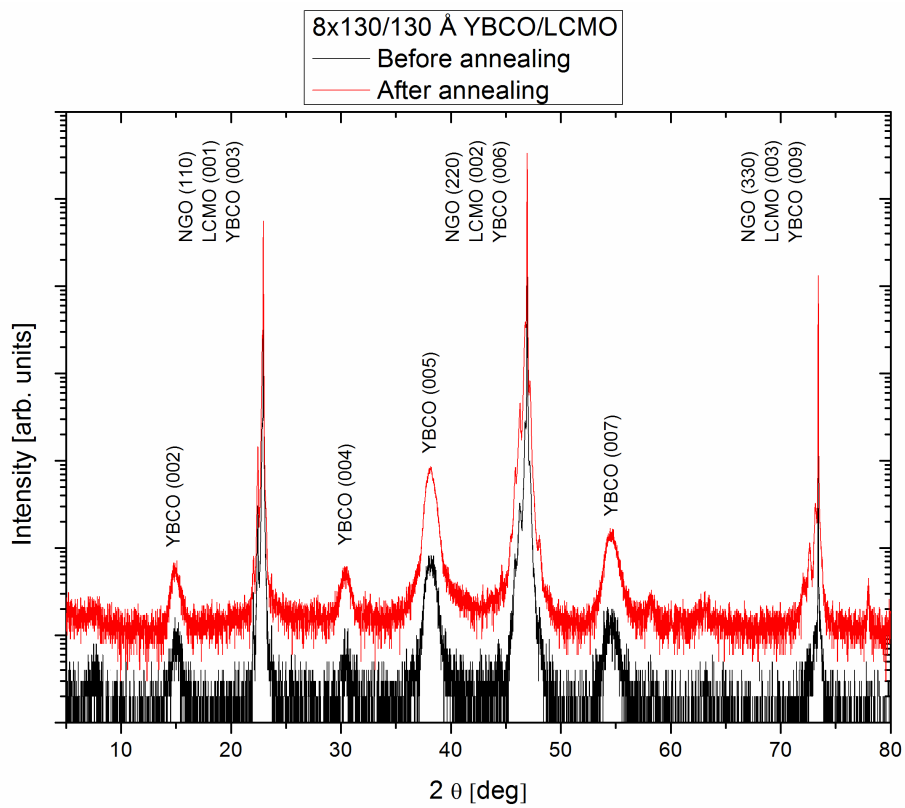|			After annealing		
Sample	Thickness [Å]	c-axis [Å] (XRD)	c-axis [Å] (XRD)	c-axis [Å] (RSM)	a-axis [Å] (RSM)
		δ	δ	δ	δ
YBCO 6	2000	11.685 ± 002	11.697 ± 003	11.693	3.855
		0.13	0.21	0.18	
LCMO 5	2000	3.864	3.864	3.863	3.855
LCMO/YBCO 2	1000/1000	11.674 ± 003	11.673 ± 005	(11.674)	(3.859)
		0.03	0.01	0.03	
YBCO/LCMO 22	1000/1000	11.724 ± 005	11.700 ± 007	(11.698)	(3.850)
		0.34	0.05	0.05	
YBCO/LCMO 23	2x 520/520	11.730 ± 010	11.716 ± 005	11.693	3.855
		0.38	0.22	0.05	
YBCO/LCMO 24	4x 260/260	11.731 ± 014 (436)	11.709 ± 017 (430)	11.703 (438)	3.855
		0.38	0.16	0.05	
YBCO/LCMO 25	8x 130/130	11.755 ± 026 (222)	11.716 ± 032 (224)	11.701 (226)	3.855
		0.50	0.22	0.05	

Fig. 41: XRD pattern of YBCO/LCMO 25 (NGO) before and after annealing (Intensities were normalized for clarification)
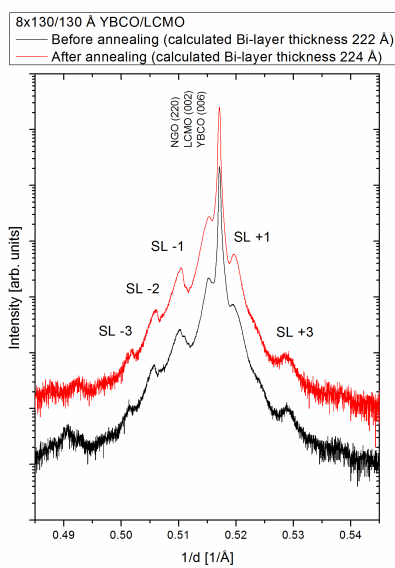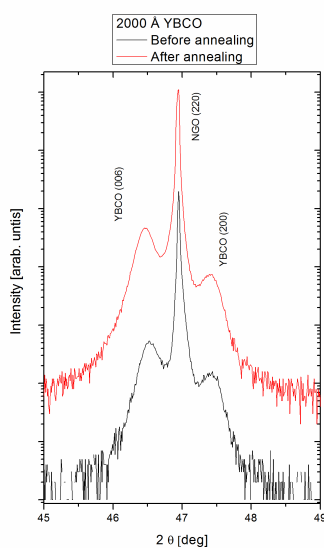

Fig. 42: Superlattice scans of YBCO/LCMO 25 (NGO) before and after annealing (Intensities were normalized for clarification)

Fig. 43 shows the XRD pattern of YBCO before and after annealing around the (220) and Fig. 44 the RSM around the (220) ((001) in pseudo cubic notation) Bragg reflection of the NGO substrate. The (006) and (200) reflection of YBCO is clearly visible in both scans. This implies that YBCO on NGO is grown in two crystallographic orientations similar to one of the samples grown on STO (YBCO 3). The origin of the unsymmetrical intensity profile in the RSM measurement shown in Fig. 44 could not be identified.

Fig. 43: XRD pattern of YBCO 6 around the (220) Bragg reflection of NGO before and after annealing (Intensities were normalized for clarification)
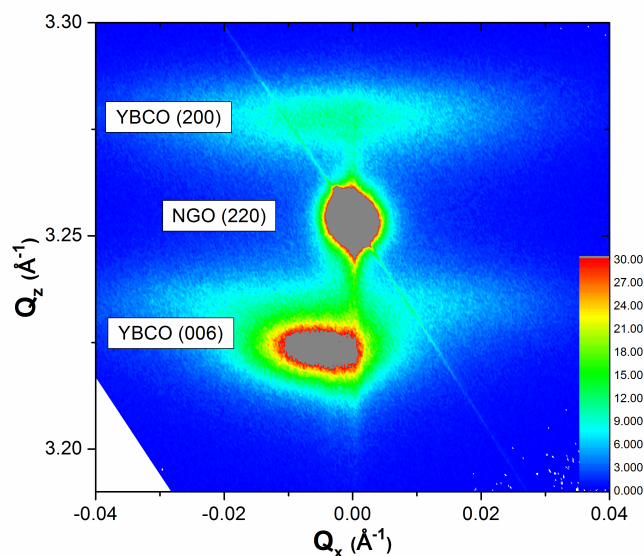
Fig. 44: RSM of YBCO 6 around (220) NGO before annealing

The analysis of the diffraction peaks using the Nelson-Riley function yields to changes of the c-axis parameters of YBCO caused by the annealing step and indicates changes in the oxygen deficiency δ (c.f. see Table 11). The c-axis of the YBCO single layer (YBCO 6) is elongated during annealing. So the oxygen content of this sample is lowered. The c-axis and thus the oxygen deficiency δ of LCMO/YBCO 2 stay stable during the annealing with values of 0.01 to 0.03. The c-axis of YBCO/LCMO 22 to 25 shortens during the annealing step, thus the oxygen content of these film is increased. The large error bars of 0.14 to 0.32 of the c-axis length estimated for YBCO/LCMO 24 to 25 results from the peak broadening of the Bragg reflections. The broadening can be caused by a small grain size of YBCO (< 100 nm), inhomogeneity in the oxygen content, a small tilt of the c-axis in reference to the surface normal in some parts of the thin film or can be result from a splitting of the peak into several peaks. The distance between these peaks is related to the bilayer thickness of the superlattice. Estimating the oxygen content using Liang et al. [54] as reference, all samples still exhibits small oxygen deficiency after the annealing. The calculated bi-layer thicknesses are nearly constant.

The RSM around the pseudo cubic (013) reflection of NGO for YBCO/LCMO 24 (NGO) is shown in Fig. 45. The (013) reflections ($Q_Y = 1.63$ Å, $Q_Z = 4.88$ Å) of the NGO substrate and the LCMO are completely overlapping because of the nearly identical lattice parameters. The reflections of YBCO are completely matching with NGO and LCMO in the Q_Y direction, resulting from a nearly complete match of the in-plane lattice parameters between YBCO (average between a and b-axis = 3.854 Å) and NGO (3.855 Å to 3.864 Å). The reflection at $Q_Z = 4.832$ Å corresponds to the (019)/(109) reflection of YBCO. The other reflections indicated in Fig. 45 are thickness fringes. They were used to calculate the bi-layer thickness of the superlattices and amount to similar values estimated from the XRD results. The c-axis length was identified for all samples using the center position of the (019)/(109) reflection of YBCO. These values are matching with the c-axis length investigated by XRD measurement for YBCO and LCMO/YBCO 2. The lengths of YBCO/LCMO 22 to 25 estimated by RSM are in general smaller compared to the results from XRD investigations. Also they are regarded to be more accurate,

because of the large error resulting from the peak broadening described before. A comparison of the results with the investigations of Liang et al. indicates an optimal oxygen content ($\delta = 0.05$) for YBCO/LCMO 22, 23, 24 and 25. Investigations of YBCO/LCMO superlattices by Driza et al. [10] using RSM came to similar results.
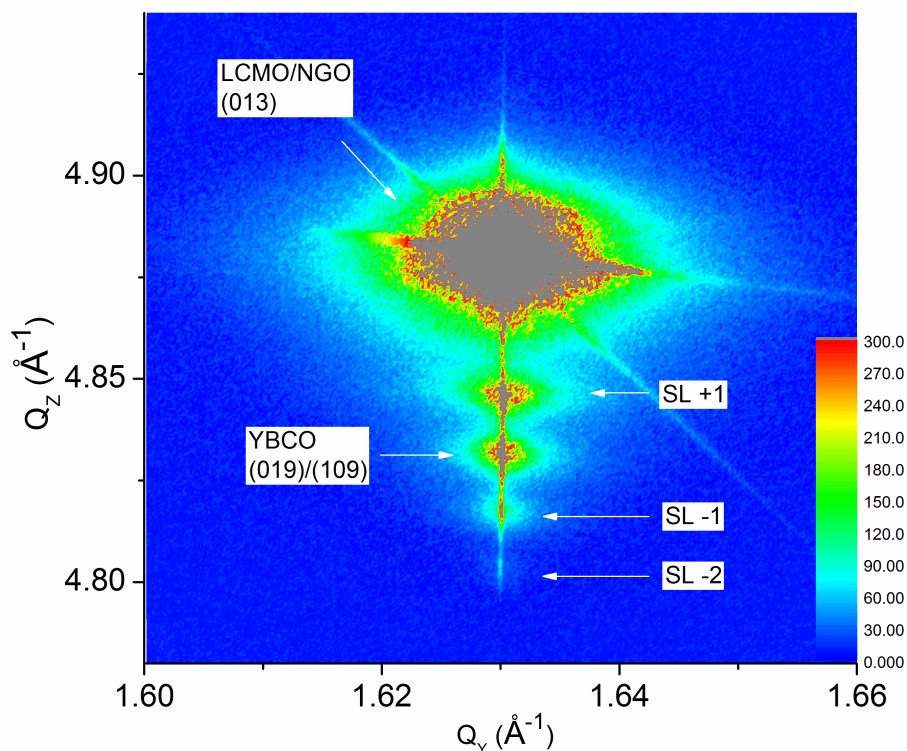

Fig. 45: RSM of YBCO/LCMO 24 (NGO) after annealing

The second annealing step (described before) was accomplished in the ZEM-3 to measure the Seebeck-coefficient and the resistivity during the annealing. The samples were investigated beginning from 50 °C in steps of 50 K up to a temperature set point of 500 °C (Fig. 46). All samples were measured 40 times at the temperature set point of 500 °C, what corresponds to an annealing time of 11 to 12 hours (Fig. 47). Afterwards the samples were cooled down also in steps of 50 K to 100 °C and measured again during this process (Fig. 46).
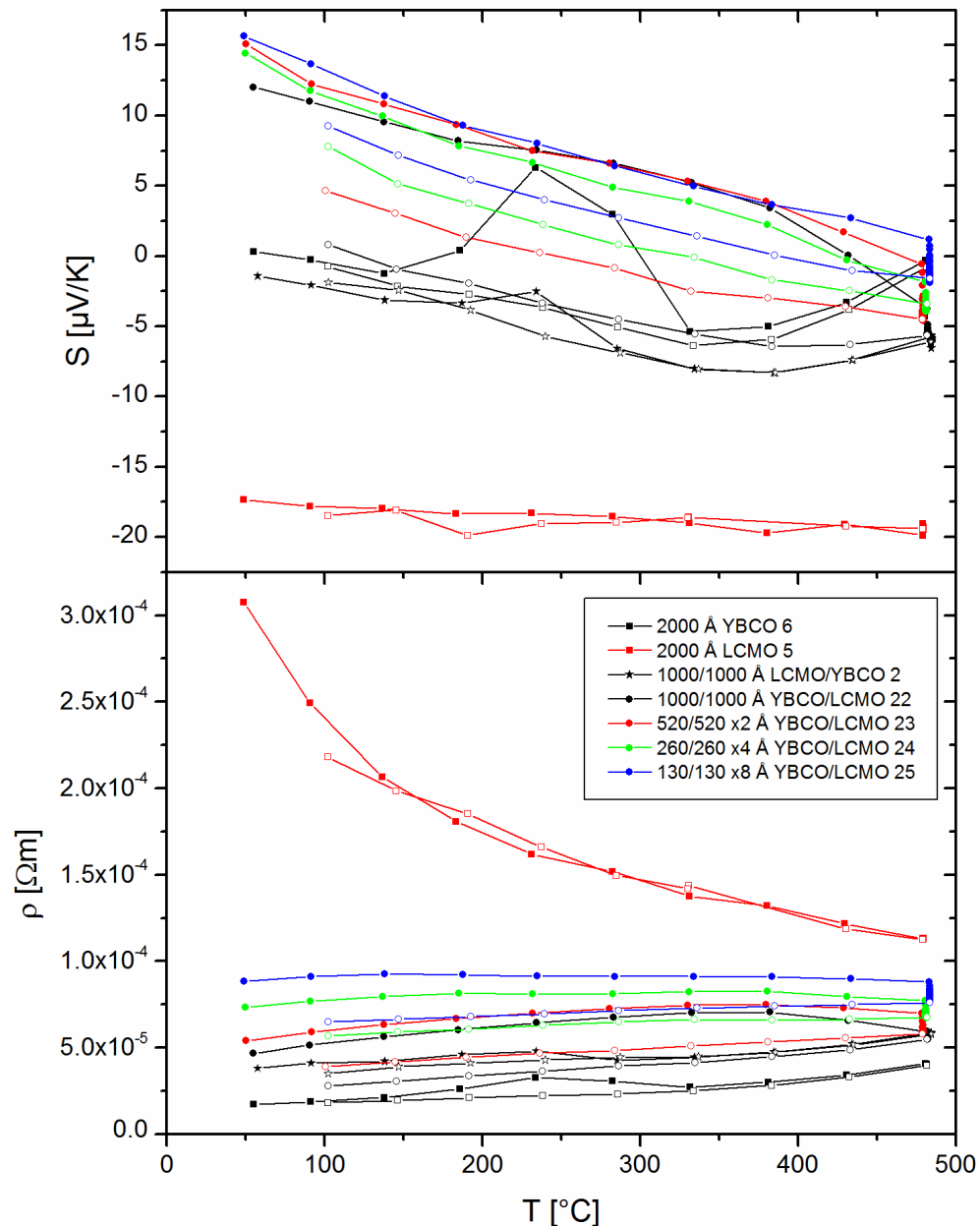
Fig. 46: Seebeck-coefficient and resistivity of all samples on NGO investigated in the ZEM-3 (closed symbols for increasing and open symbols for decreasing temperature)

The Seebeck-coefficients of all samples except YBCO 6 are decreasing with increasing temperature up to 400 °C. Afterwards the slopes are changing with increasing temperature. The changes of S(T) and ρ(T) at the 480 °C are depicted in Fig. 47 and explained later. YBCO 6 exhibits a broad maximum between 150 and 335 °C and an upturn of S(T) at temperatures higher 335 °C, which was previously described by Molenda et al. [40] as an indication for the phase transition to the tetragonal phase. The increase of S(T) between 150 °C and 235 °C is maybe related

to some at structural phase transition is some parts of the thin film. But the decrease of $S(T)$ between 235 °C and 335 °C is related to a structural realignment which destroys a possible second phase in YBCO. This assumption is supported by the absence of this maximum in the cooling curve. A similar, but weaker behavior was found in LCMO/YBCO 2.

Whereas the absolute values of $S(T)$ for YBCO 6, LCMO 5 and LCMO/YBCO 2 are nearly identical before and after annealing, the other structures show pronounced changes in $S(T)$. In general, the Seebeck-coefficient was smaller after annealing compared to the initial state. In combination with the results from the XRD investigations, the changes could result from an increase of the oxygen content in the YBCO layers. Since the absolute values of YBCO/LCMO 22 to 25 are relatively similar during heating from 50 to 380 °C, they differ from each other after annealing. The pronounced changes are observable in YBCO/LCMO 22 (from 11 µV/K to 1 µV/K at 100 °C) and they get smaller with decreasing YBCO thickness in the superlattices (from 13 µV/K to 9 µV/K for YBCO/LCMO 25 at 100 °C).

The resistivity increases for all samples with increasing temperature, except for LCMO, where it decreases. Similar to the behavior examined for $S(T)$, the resistivity is the same for YBCO 6, LCMO 5 and LCMO/YBCO 2 before and after annealing. Also YBCO 6 shows a broad maximum between 150 °C and 325 °C. The resistivity of YBCO/LCMO 22 to 25 is smaller after the annealing step. In contrast to $S(T)$, the shift of $\rho(T)$ is similar for all samples. So the dependences of $S(T)$ and $\rho(T)$ from the oxygen content are different in these samples. The changes in the oxygen content modify the charge carrier concentrations and thus the resistivity. In addition, the change of the oxygen content can modify the entropy of the system and the interactions between YBCO and LCMO.

The time dependent modifications of the Seebeck-coefficient and the resistivity of all samples at a constant temperature of 480 °C are shown in Fig. 47. Whereas the single layer thin films (YBCO and LCMO) and LCMO/YBCO 2 are stable, the samples YBCO/LCMO 22 to 25 show time dependent changes. In general, the $S(480\ °C)$ and $\rho(480\ °C)$ are decreasing over time till the values gets constant. The

period of change differs between the samples and depends on the number of interfaces in the structures. It can be relatively short (1 h for YBCO/LCMO 22 with one interface), taking some hours (4.5 h for YBCO/CMO 23; 3.5 h for YBCO/LCMO 24) or last over the complete annealing time (12 h for YBCO/LCMO 25 with 15 interfaces). A direct comparison between the annealing times is not possible, because some samples were modified (c.f. see Fig. 46) before reaching the annealing temperature of 480 °C. Nevertheless, the experiment shows the need of very long annealing time for superlattices grown on NGO.
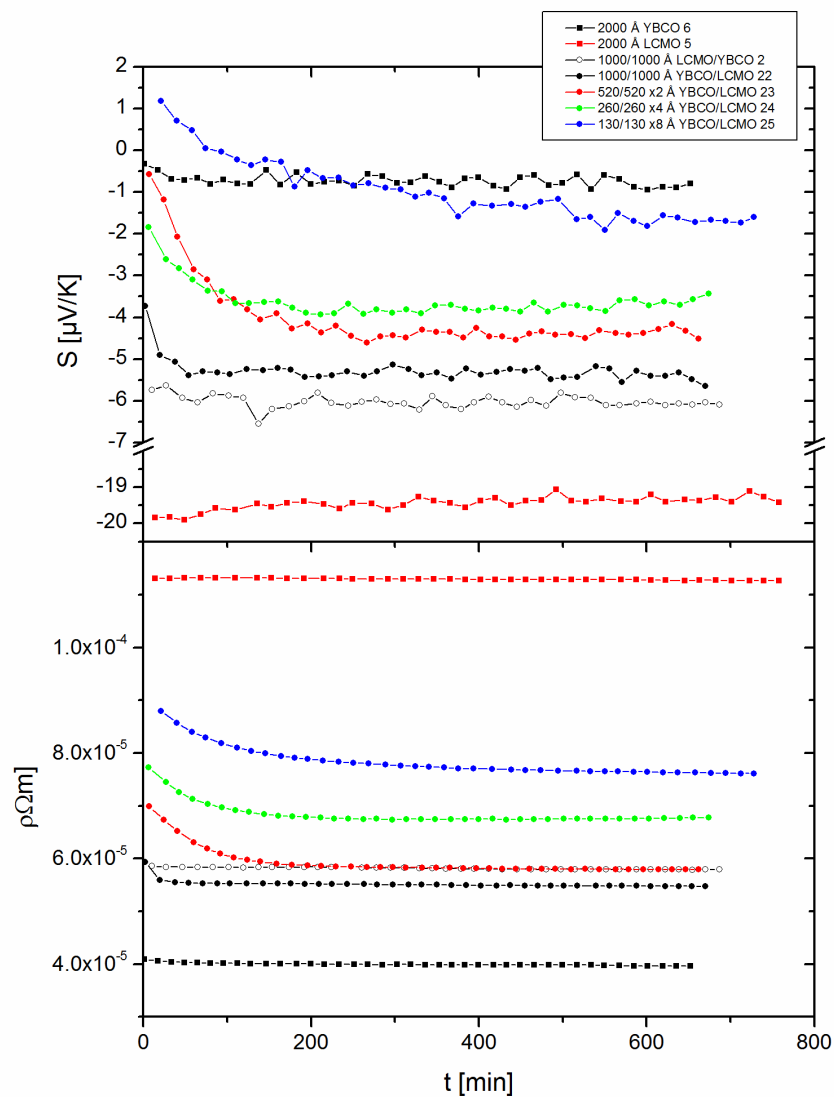

Fig. 47: Seebeck-coefficient and resistivity of all samples on NGO investigated in the ZEM-3 at 480°C

The Seebeck-coefficient of YBCO/LCMO 22 to 25 at different temperatures is plotted versus the number of interfaces in the superlattices in Fig. 48. The results indicate a strong dependence of *S(T)* on the number of interfaces (as well as YBCO thickness c.f. see Table 11). So the Seebeck-coefficient is increasing with the number of interfaces (or with decreasing YBCO thickness) at all temperatures.
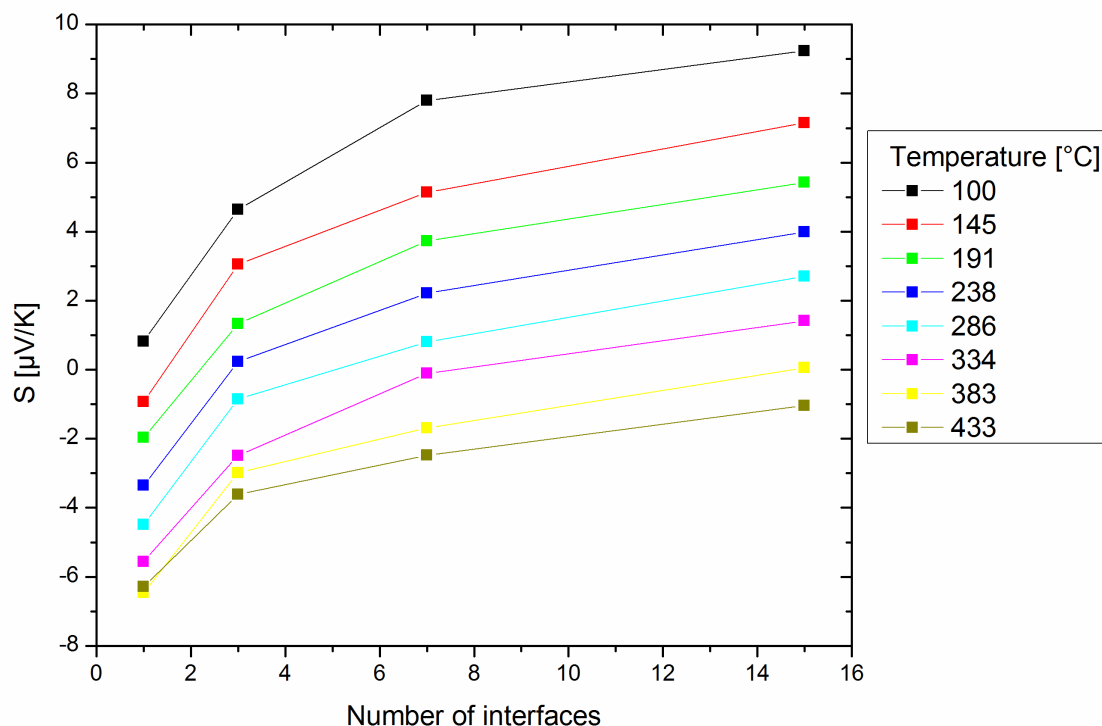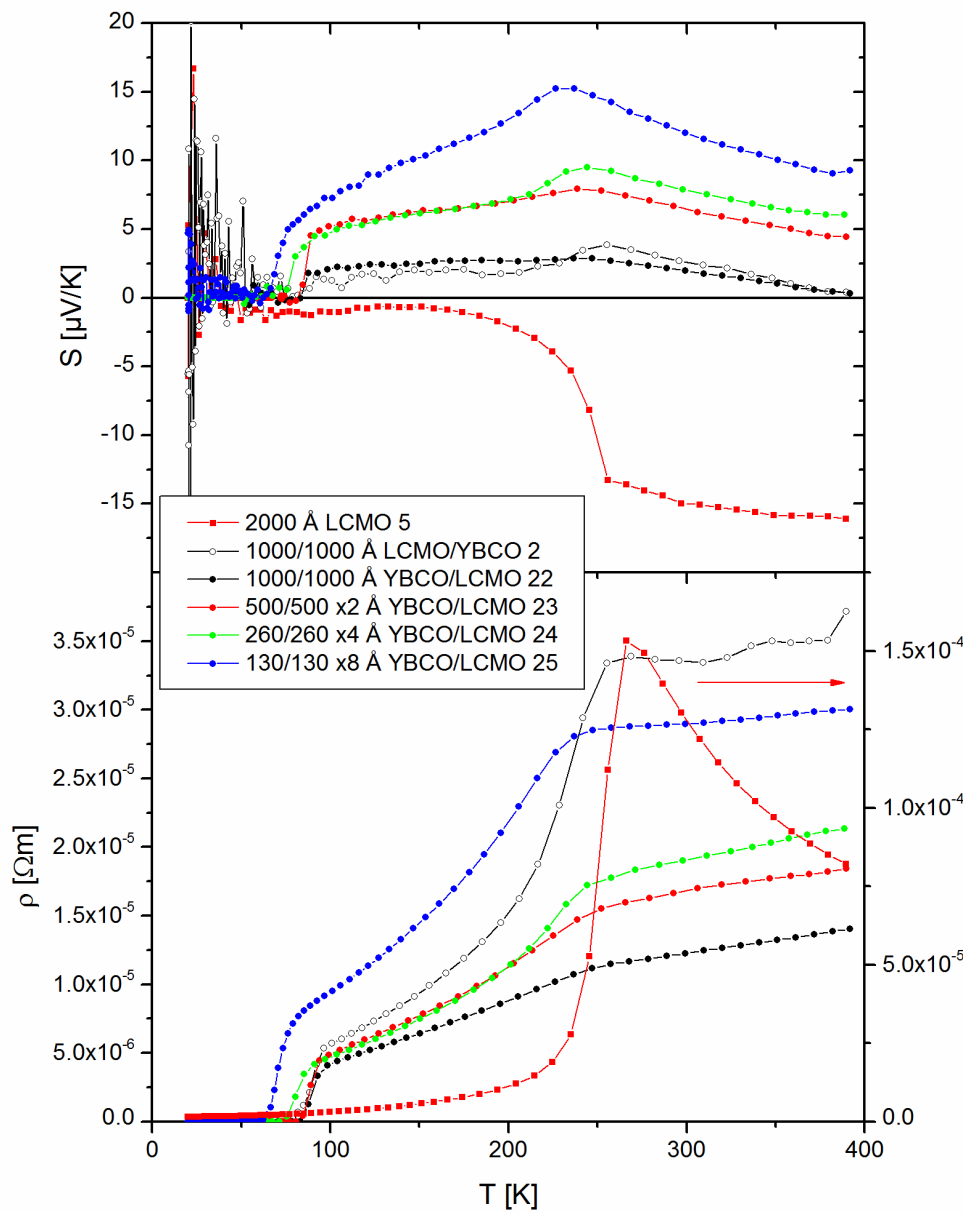

Fig. 48: Seebeck-coefficient of YBCO/LCMO 22 to 25 at certain temperatures in dependence of the number of interfaces

The samples were contacted and measured in the PPMS as described in Chapter 4. 4. 1. as comparative study to samples on STO. The results for the Seebeck-coefficient and the electrical resistivity of all samples expect YBCO 6 are shown in Fig. 49. The temperature behavior of the Seebeck-coefficient and the electrical resistivity are in general similar to the results investigated for samples grown on STO. Again *S(T)* rises at T_C and shows a maximum at T_{Curie} for all samples except LCMO/YBCO 2. Both temperatures, T_C and T_{Curie}, are also observable in *ρ(T)* at nearly the same temperatures. The transition temperatures and the values for *S(355 K)* are summed up in Table 12.

Table 12: Transition temperatures and Seebeck-coefficient at 355 K of samples on NGO

Sample	Thickness [Å]	Number of interfaces	T_C [K]	T_{Curie} [K]	S (355 K) [µV/K]
LCMO 5	2000	0	-	255 (267)	- 15.9
LCMO/YBCO 2	1000/1000	1	79	269	1.2
YBCO/LCMO 22	1000/1000	1	83	261	0.9
YBCO/LCMO 23	2x 520/520	3	81	254	5.1
YBCO/LCMO 24	4x 260/260	7	72	245	6.5
YBCO/LCMO 25	8x 130/130	15	61	238	9.9

Fig. 49: Seebeck-coefficient and resistivity of samples on NGO measured in the PPMS

The superconducting transition temperatures T_C investigated for LCMO/YBCO 2 (79 K) and YBCO/LCMO 22 (83 K) and 23 (81 K) are similar to the temperatures measured for single layer YBCO thin films (84 to 86 K), what is a sign of a nearly optimal doped YBCO. Since LCMO/YBCO 2 and YBCO/LCMO 22 are similar concerning $S(T)$, one can conclude, that both thin films exhibits the same properties, independent from the stacking sequence. The strong differences in $\rho(T)$ are unexpected because of the high $\rho(T)$ of LCMO/YBCO 2 and could result from contact problems during the measurement. The increase of $S(T)$ of YBCO/LCMO 23 in comparison to YBCO/LCMO 22 can be addressed to interactions between YBCO and LCMO. As reported by Driza et al. [10], mutual influences between both materials can occur over a range of more than 500 Å.

Comparing the Seebeck-coefficient and the resistivity of the superlattices grown on STO and NGO, shown in Fig. 50, leads to similarities and differences. Since the values for the transition temperatures ($\Delta T_C \approx 2$ K; $\Delta T_{Curie} \approx 15$ K) and $\rho(T)$ of the corresponding superlattices are nearly matching, the absolute values of $S(T)$ differs. The origin of these differences is not clear. An oxygen deficiency and strain induced effects can be ruled out as described before. The small shift of T_{Curie} could indicate changes in the LCMO layers. But a strong contribution from LCMO can be neglected according to Kirchhoff's law as discussed before. The origin of the differences in $S(T)$ could origin from slightly different crystallographic properties between thin films on STO and NGO. As described by Malik et al. [27], samples grown on NGO show a high crystalline perfectness. If the samples grown on STO exhibit a higher amount of defects, the entropy of the system can also be increased and thus the Seebeck-coefficient. A preferred orientation of the a-axis of YBCO 6 on the pseudo cubic NGO substrate could also be responsible for the differences. A $S(T)$ resulting only from the copper oxygen planes differs from the combination of the copper oxygen plane and chains as described in Chapter 5. 1. The unsymmetrical shape of the (006) reflection of YBCO 6 in Fig. 44 could result from an in plane anisotropy of YBCO 6 on NGO.
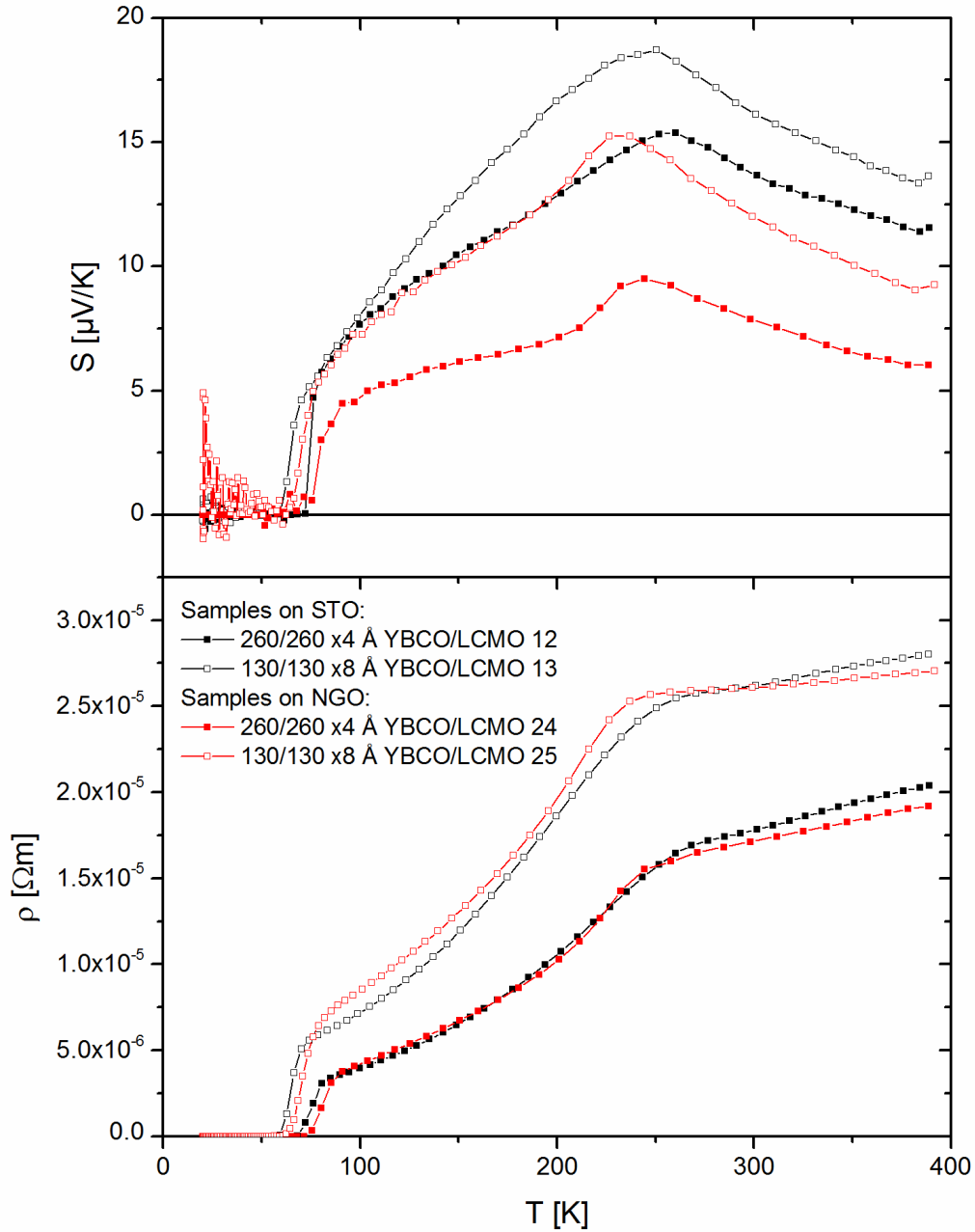
Fig. 50: Seebeck-coefficient and resistivity of superlattices grown on STO and NGO

Similar to the samples grown on STO, the activation energies E_S and E_ρ were calculated similar to single layer LCMO (c.f. see Chapter 5. 2.). The calculations were done using the results from PPMS and ZEM-3 measurement and plotted in Fig. 51. The differences in the absolute values of $\rho(T)$ between the low (PPMS) and high (ZEM-3) temperature range are caused by the measurement conditions with different contact mechanisms. The estimated activation energies using the PPMS result to values of 2 to 4 meV for E_S and 15 to 25 meV for E_ρ, respectively. The values

determined are equal to the results from measurements for the samples grown on STO. They are matching the activation energies reported by Hundley et al. [22] for E_S and much smaller than the energies reported for E_ρ. The results confirm the investigation from the samples grown on STO. The temperature dependence of the Seebeck-coefficient follows the LCMO, whereas the absolute values are similar to YBCO. The activation energies were also evaluated in the high temperature range, using the results from the ZEM-3. The calculated energies using the Seebeck-coefficient are two to three times higher than the values examined in the low temperature range. So they are more similar to LCMO with a Mn^{4+} concentration less than 0.3 [22]. The energies E_ρ calculated from the ZEM-3 results differ and exhibit a large error bar, because of the nonlinearity of the curves (c.f. see Fig. 51).
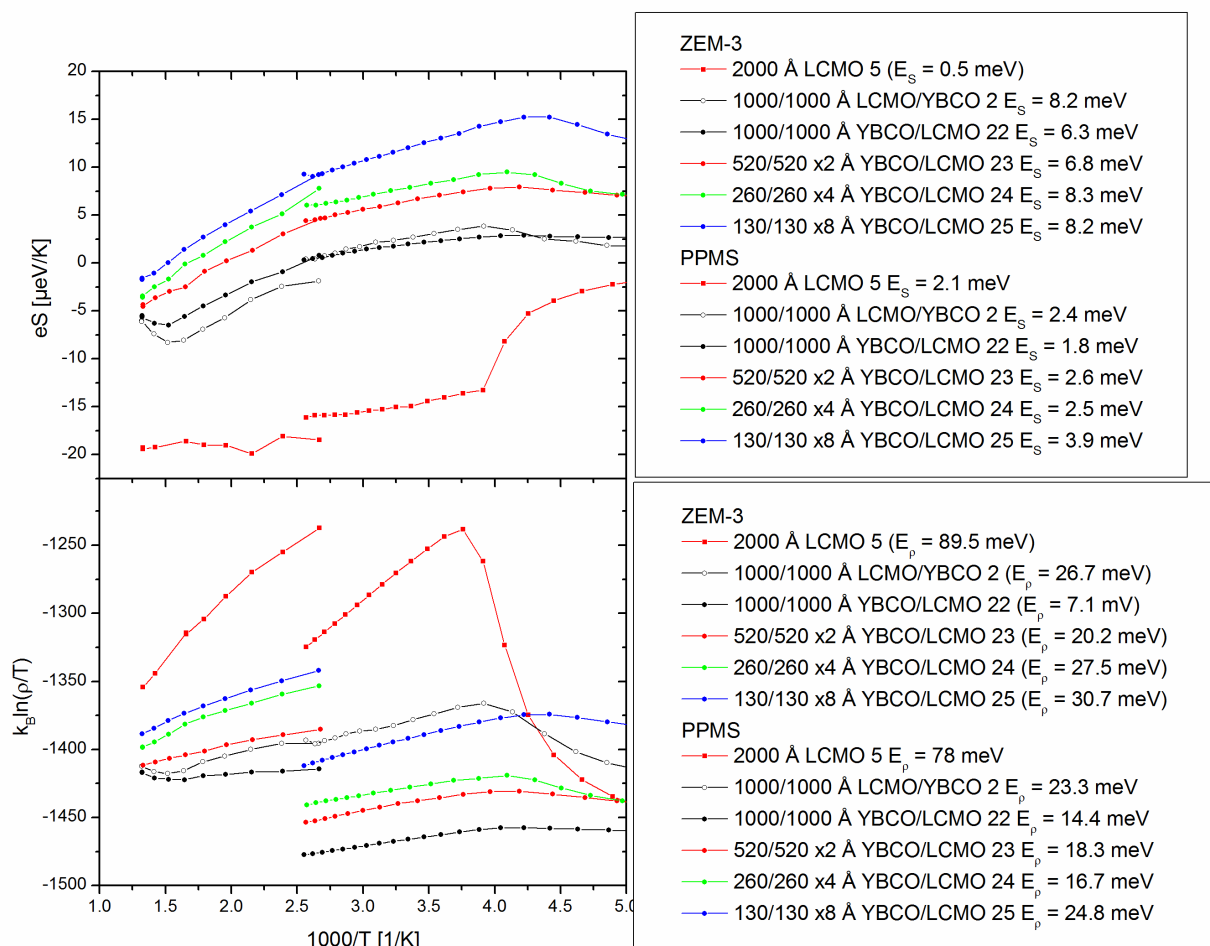

Fig. 51: Calculated activation energies following assumption for pure LCMO

In summary, the crystallographic properties of thin films of YBCO and LCMO, as well as the corresponding heterostructures and superlattices, on NGO were investigated directly after the deposition and after an additional annealing step. Changes of the lattices parameters and the oxygen content of the thin films could be examined. Most of the samples exhibit an optimal oxygen content ($\delta = 0.05$) after the additional annealing step. The Seebeck-coefficient and the electrical resistivity were measured during the complete annealing process to monitor possible changes during the heating to 480 °C, the annealing at 480 °C and the cooling back to 100 °C. Both, Seebeck-coefficient and electrical resistivity, are stable (YBCO 6, LCMO 5, LCMO/YBCO 2) or decreasing (YBCO/LCMO 22 to 25) during the annealing at 480 °C. A comparison of the values obtained before and after annealing shows a decrease of $S(T)$ and $\rho(T)$ for YBCO/LCMO 22 to 25. Also a clear dependence of the Seebeck-coefficient from the number of interfaces in YBCO/LCMO 22 to 25 at high temperatures was found. $S(T)$ increases with increasing number of interfaces. The samples were also investigated at low temperatures using the PPMS. The results reproduce the findings of the investigations of thin films on STO qualitatively. The origin of the differences in $S(T)$ could not be identified till now. The calculated activation energies are similar to the values examined in thin films on STO and matching with the values of E_S for single layer LCMO thin films.

5. 5. Thermoelectric properties of PrBa$_2$Cu$_3$O$_{7-\delta}$/La$_{2/3}$Ca$_{1/3}$MnO$_3$ heterostructures grown on SrTiO$_3$

The Seebeck-coefficient and the electrical resistivity of heterostrucutres consisting of PrBa$_2$Cu$_3$O$_{7-\delta}$ and La$_{2/3}$Ca$_{1/3}$MnO$_3$ were investigated to examine the influence of different contact techniques on the results of the investigations. There should be no differences in the Seebeck-coefficient and the electrical resistivity of two identical samples investigated, using different contact techniques. The results should always reflect the properties of the whole thin films and not only the top layer of a heterostructure or superlattice.

Three batches of samples, each with two samples, were deposited together in PLD 2 on single crystalline (001) - orientated SrTiO$_3$ in the same process for a comparative study. The batches differ in the thickness of the individual layers and the stacking sequence (PBCO or LCMO as first layer). The properties of the samples together with the properties of the corresponding single layer thin films (one example for PBCO and two examples for LCMO) are summarized in Table 13. The samples were deposited at 750 °C and 0.5 mbar and annealed at 530 °C for 1 hour in 1 bar oxygen. Consequently, two samples from one batch exhibit the same thickness and the same crystallographic properties as shown in Fig. 52. This figure also indicates single phase c-axis oriented growth of the samples. The in plane lattice parameters of PBCO (in average 3.893 Å) are nearly matching the lattice parameter of STO (3.905 Å) and are slightly larger compared to LCMO (3.864 Å). So mutual strain or strain induced by the substrate can nearly be rule out.
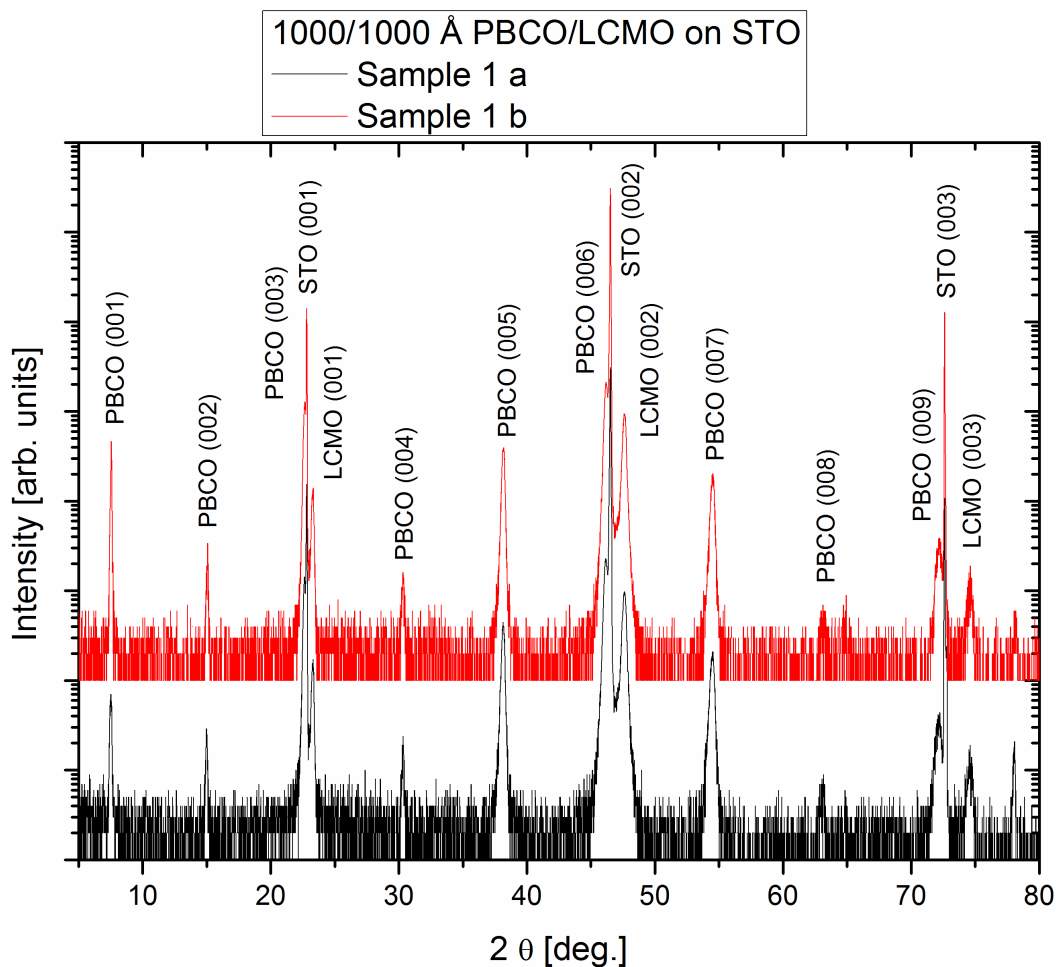
Fig. 52: XRD pattern of PBCO/LCMO 1 a and b on STO

The c-axis length of PBCO and LCMO was calculated using the positions of the Bragg reflections and the Nelson Riley function as described before. The investigated c-axis length for PBCO matches with those reported by Chryssikos et al. [57] and López-Morales et al. [60]. In contrast, the c-axis length of PBCO in the heterostructures PBCO/LCMO 1 (11.765 Å) and PBCO/LCMO 2 (11.746 Å) are much larger compared to single layer PBCO, since the c-axis length in LCMO/PBCO is similar (11.706 Å to11.723 Å) to single layer PBCO. According López-Morales et al. [60], the c-axis length of PBCO is correlated with its oxygen content. Taking López-Morales et al. as a reference, the oxygen deficiency δ amounts to 0.38 for PBCO/LCMO 1, 0.34 for PBCO/LCMO 2 and less than 0.1 for LCMO/PBCO 1. The reduced oxygen content could be caused by an insufficient annealing. A similar behavior was found for YBCO/LCMO 3 and 4 (c.f. see Chapter 5. 3. 1.). These samples could by oxygen deficient because of the relatively short annealing time.

Table 13: Sample properties and contact mechanism

Sample	Thickness [Å]	c-axis length [Å] (first column PBCO and second LCMO)	T_{Curie} [K]	Contact mode	
				On top	Etched
PBCO	2000	11.716		X	
LCMO 2	2000	3.794 ± 0.003	220	X	
LCMO 3	2000	3.814 ± 0.001	275	X	
PBCO/LCMO 1 a	1000/1000	11.765 ± 0.006 3.814 ± 0.002	240	X	
PBCO/LCMO 1 b	1000/1000	11.762 ± 0.004 3.813 ± 0.001	240		X
PBCO/LCMO 2 a	500/500	11.746 ± 0.023 3.800 ± 0.001	208	X	
PBCO/LCMO 2 b	500/500	11.746 ± 0.020 3.800 ± 0.001	210		X
LCMO/PBCO 1 a	1000/1000	11.723 ± 0.009 3.819 ± 0.002	258	X	
LCMO/PBCO 1 b	1000/1000	11.706 ± 0.006 3.819 ± 0.002	247		X

One sample from a batch was measured with contacts just deposited on top of the sample. The other sample was lithographically patterned and wet chemically etched to remove parts of the films down to the substrate. Subsequently, the etched parts were refilled with contact material. Both contact techniques are shown in Fig. 53. The contacts consisting out of chromium and gold with nominal thicknesses of 20 and 200 nm (Cr/Au 20/200 nm), respectively, were thermally evaporated. Alternatively to Cr/Au, Ti/Pt contacts with the same thicknesses were used for contacting an additional LCMO thin film. Both samples exhibit identical physical properties, independent on the contact material.
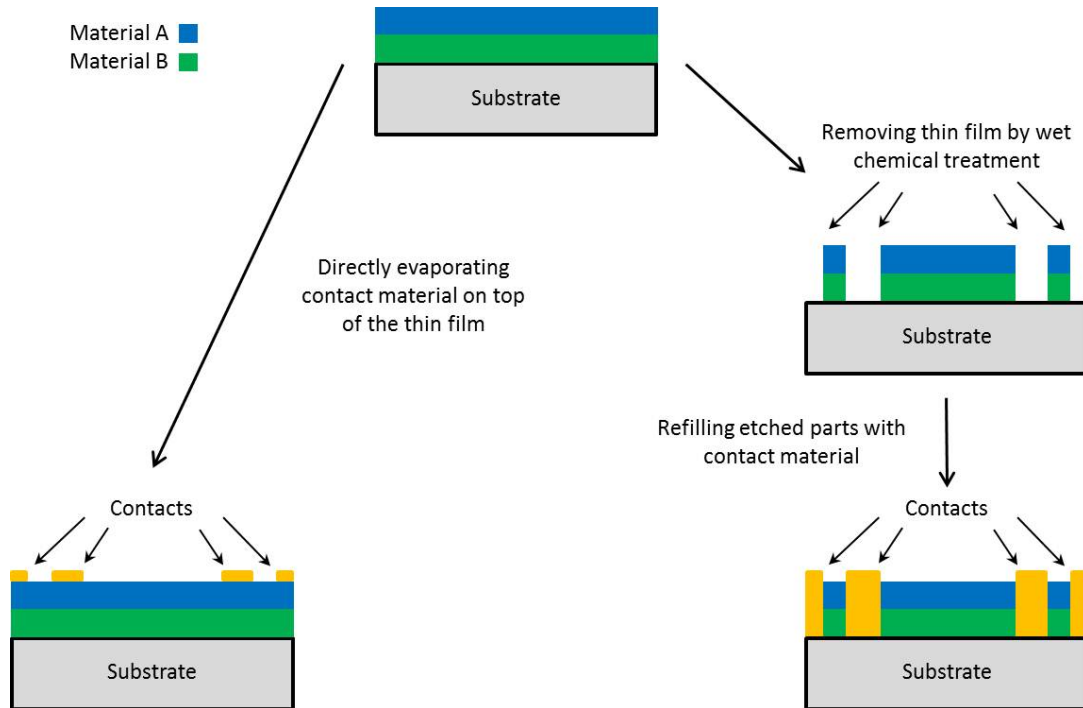
Fig. 53: Different contact mechanism for the investigations of thin film materials

The Seebeck-coefficient and the electrical resistivity of all samples were investigated in the temperature range from 20 K to 390 K. The individual samples from one batch exhibit quantitatively the same properties. So the properties of the samples from one batch are discussed together in the following paragraphs. The results are depicted in Fig. 54. The Seebeck-coefficients of all heterostructures are small and positive in the temperature range of the ferromagnetic phase of LCMO, similar to LCMO 2. $S(T)$ increases with increasing temperature and reaches a broad maximum for all heterostructures. The ferromagnetic transition temperature T_{Curie} was estimated using this maximum of $S(T)$ for the heterostructures (c.f. Table 13). The Curie temperature of all heterostructures is shifted to lower temperatures by 15 K to 65 K compared to LCMO 3. Afterwards, $S(T)$ decreases nearly linearly. The temperature dependence of the resistivity of all heterostructures is qualitatively similar to the $\rho(T)$ of pure LCMO. But the maxima in $\rho(T)$ of the heterostructures are not corresponding to T_{Curie}. The combination of the resistivity values of single layer PBCO and LCMO according to Kirchoff's law leads to a maximum that is shifted to lower temperatures compared to T_{Curie}. The absolute values of $\rho(T)$ of PBCO/LCMO 1 and especially for PBCO/LCMO 2 are much higher than expected. This could result from a higher resistivity in the LCMO and the PBCO layers. The absolute values of the resistivity of

PBCO in the heterostructures could be much higher since it is strongly dependent on the oxygen content of PBCO [60]. A reduction of the oxygen content of $\delta = 0.4$ could increase the resistivity by two orders of magnitude. An increase of the resistivity of LCMO could also be caused by an oxygen deficiency. This is indicated by the shift of T_{Curie} to lower temperatures what could be caused by a lowered oxygen content. This relation was discussed for single layer LCMO thin films in Chapter 5. 2.

The Seebeck-coefficient of the investigated heterostructures PBCO/LCMO 1 and 2 is higher than expected according to Kirchhoff's law. The Seebeck-coefficient of the heterostructures should be embedded between the Seebeck-coefficients of the individual materials. In contrast to these theoretical observations, the Seebeck-coefficients of PBCO/LCMO 1 and 2 shown in Fig. 54 are higher than the coefficients of PBCO. Again, the findings can be explained as an effect of the lowered oxygen content in the PBCO layers. $S(T)$ of PBCO can be simply shifted to values of 200 µV/K for oxygen contents $\delta > 0.04$. Only the Seebeck-coefficient of LCMO/PBCO 1 can be seen as a simple combination of the properties of single layer LCMO and PBCO, since $S(T)$ of LCMO/PBCO 1 is embedded between the Seebeck-coefficients of LCMO and PBCO.
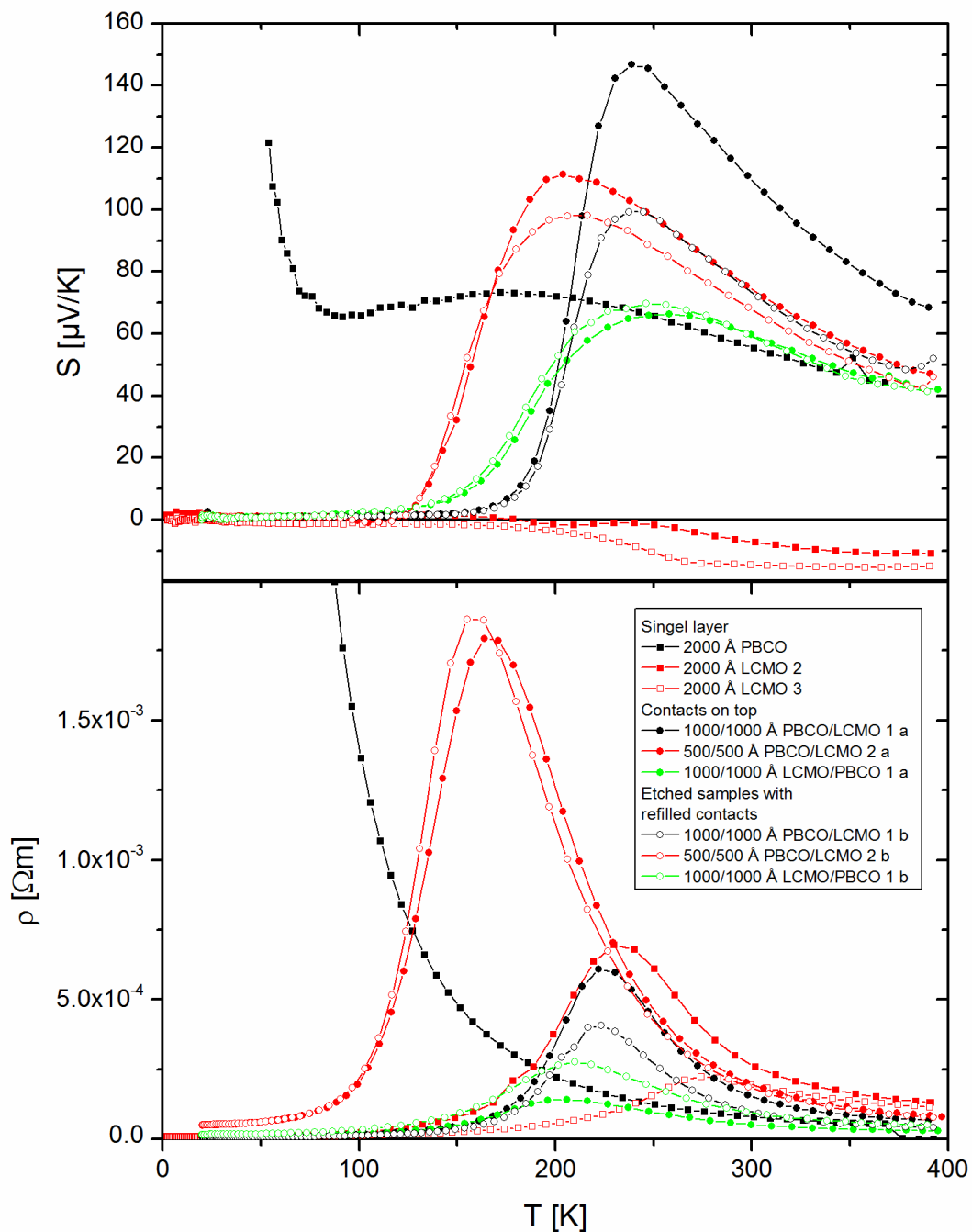
Fig. 54: Seebeck-coefficient and resistivity of PBCO and LCMO thin films as well as the corresponding heterostructures

The investigated samples fabricated in one run should exhibit identical properties. So the measured results should also match independent on the contact techniques. Samples PBCO/LCMO 1 a and b exhibits the same T_{Curie}, but differ in the absolute values from $S(T)$ and $\rho(T)$. The Seebeck-coefficient as well as the resistivity is much higher for the sample with the contacts on top of the surface, what is completely

unexpected. The differences between both samples could be caused by a electrical and thermal shortcut on the samples surface of PBCO/LCMO 1 a. In contrast, the *S(T)* of PBCO/LCMO 2 a and b only slightly differs (less than 10 % difference) and *S(T)* of LCMO/PBCO 1 a and b are nearly matching. These results confirm the expectations for parallel conductors according to Kirchhoff's law. The *ρ(T)* values of PBCO/LCMO 2 a and b are also nearly matching. For LCMO/PBCO 1 a and b the resistivity differs, but in this case, the resistivity of the sample with the contacts on top exhibits the smaller resistivity.

Summarizing the findings, the Seebeck-coefficient is not depending on the contact techniques for the measurement as shown for PBCO/LCMO 2 and LCMO/PBCO 1. The differences found between PBCO/LCMO 1 a and b could result from contact problems. The results of the resistivity are inconsistent. The resistivity is higher, smaller or the same for the different samples. So the resistivity is more sensitive on the contact quality than on the contact mechanism.

5. 6. Thermoelectric properties of YBa$_2$Cu$_3$O$_{7-\delta}$ and La$_{2/3}$Ca$_{1/3}$MnO$_3$ thin films, heterostructures and superlattices grown on 5 ° off cut (001) SrTiO$_3$

The investigation of oxide thin films, heterostructures and superlattices grown on low-index oriented single crystal substrates with an intentional miscut towards a specific low-index direction offers the possibility to measure anisotropic transport properties and the components of the Seebeck tensor. Additionally, films on miscut substrates can be used to design new types of thermoelectric sensing devices.

Since the discovery of laser induced thermoelectric voltages (LITV) in thin film YBCO samples by Chang at el. [84] in 1990, the anisotropic thermoelectric properties of YBCO thin films were studied systematically. Lengfellner et al. [11] and Renk et al. [12] made systematic studies of YBCO thin films deposited on (001) – oriented SrTiO$_3$ single crystals and described the results in terms of a thermopile effect. They proved that the LITV signals are of purely thermoelectric origin and are determined by

$$U = \frac{l}{2t}(S_{ab} - S_c)\Delta T \sin 2\alpha \qquad\qquad \textbf{Equation 20}$$

where l is the illumination length of the laser spot on the sample surface, t the thickness of the thin film, S_{ab} and S_c the in plane and out of plane Seebeck-coefficients of the sample, ΔT the temperature gradient between the thin film surface and the substrate and α the off cut angle of the substrate and the thin film. The origin of Equation 20 is described in Chapter 2. 3. in detail.

Zhang et al. investigated the thickness dependence [85, 86] and the dependence of the off cut of the substrate [86] on the LITV signal of YBCO thin films. They investigated a maximum of the LITV signal for a sample thickness of 2500 Å on 10 ° off cut STO (001) samples and an inverse proportionality of the LITV signal from the sample thickness for samples thicker 2500 Å. They also reported a linear increase of

the LITV signal with increasing off cut angle of the substrate. The same linear dependence was reported by Kwok et al. [87] and Renk et al. [12] before. The relation of the LITV signal from the incident energy was investigated by Kleinhames et al. [88], who reported a linear dependence of the LITV signal from the incident energy for different wavelength.

The influence of the oxygen content of YBCO on the LITV signal was investigated by Xiong et al. [89]. They reported a sign change of the LITV signal from positive for optimally doped YBCO to negative for underdoped YBCO with an oxygen deficiency larger than 0.25. The sign change is expected to develop from negative to positive values since the Seebeck-coefficient of optimally doped YBCO is negative in the ab-plane and positive in the c-direction [17]. A reduction of the oxygen content of YBCO leads to large positive Seebeck-coefficients in the ab-plane whereas the changes of the Seebeck-coefficients of the c-axis are small compared to the ab-plane [17]. Subsequently, the LITV signal of optimally doped YBCO should be negative and positive for underdoped YBCO.

In addition to the investigations done for YBCO, other oxide materials like manganites ($La_{1-x}Ca_xMnO_3$, $La_{0.6}Pb_{0.4}MnO_3$) and cobaltates (Na_xCoO_2, $Ca_2Co_3O_9$, $La_{0.5}Sr_{0.5}CoO_3$) were examined concerning the anisotropy of the thermoelectric properties. Habermeier et al. [90] investigated the anisotropy of thermoelectric properties in $La_{2/3}Ca_{1/3}MnO_3$ and addressed the occurrence of a LITV signal to an intrinsic anisotropy caused by the Jahn-Teller effect of the Mn^{3+} ions. Further experiments were done by Li et al. [91] who investigated thin film samples with different thicknesses on STO substrates with different off cut angles. They found a linear increase of the LITV signal with increasing off cut angle, analog to the effects reported for YBCO.

The investigations of the LITV signal in multilayered structures (heterostructures and superlattices) were focused on metallic systems till now [92-94]. So far, the LITV signals of oxide heterostructures and superlattices were only studied systematically for $YBa_2Cu_3O_{7-\delta}/La_{0.6}Pb_{0.4}MnO_3$ and $LaNiO_3/LaAlO_3$ superlattices. Zhang et al. [86] reported LITV signals of $YBa_2Cu_3O_{7-\delta}/La_{0.6}Pb_{0.4}MnO_3$ superlattices which were much

higher compared to the signals of single layer thin films with equivalent thickness and off cut angles of the substrate. Zhang et al. [86] investigated superlattices with a constant bilayer thickness and explored the influence of the number on repetitions and the off cut angle of the substrate on the LITV signal. Similar to the findings for YBCO thin films, they found an increase of the LITV signal with increasing off cut angle of the substrate. Also, they describe a decrease of the LITV signal with increasing superlattice thickness. Ding et al. [95] investigated the LITV signal of $LaNiO_3/LaAlO_3$ superlattices grown on different substrates and found that the LITV signals of $LaNiO_3/LaAlO_3$ multilayers are significantly larger than those of $LaNiO_3$ single layers.

Thin films of YBCO, LCMO as well as heterostructures and superlattices of both materials (all with a nominal thickness of 2000 Å) were deposited by Mr. Cristiani in PLD 2 on (001) orientated STO single crystals with a nominal off cut angle of 5 ° with respect to the [100] direction in the (001). All samples were deposited at 730 °C and 0.5 mbar and annealed at 530 °C and 1 bar for 30 minutes in oxygen. The substrates exhibit two cropped corners to mark the direction of the off cut in reference to the edges of the substrate. But the direction of the off cut from the surface normal (- or + 5 °) in reference to the cropped corners is not defined and was examined by XRD measurements (c.f. see Fig. 55). The results are summarized in Table 14.
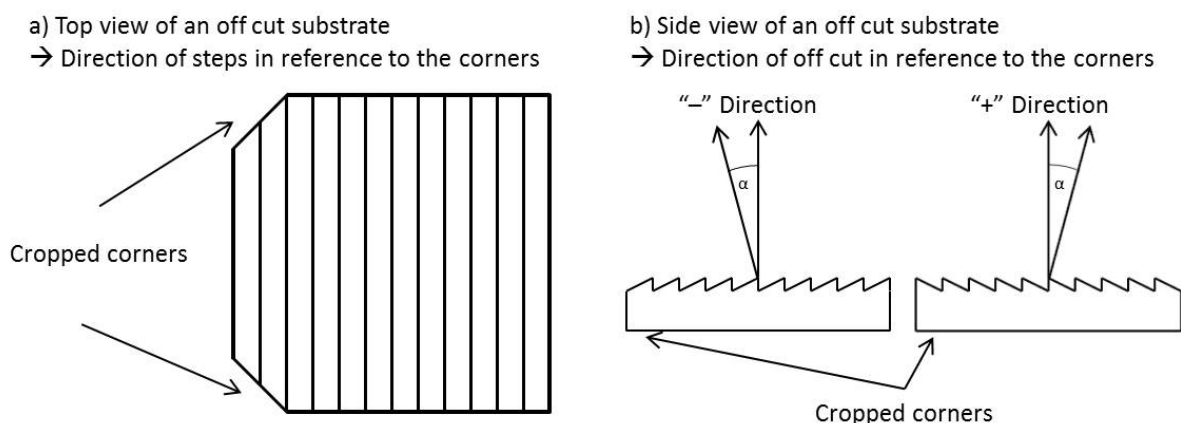

a) Top view of an off cut substrate
→ Direction of steps in reference to the corners

Cropped corners

b) Side view of an off cut substrate
→ Direction of off cut in reference to the corners

"–" Direction   "+" Direction

α   α

Cropped corners

Fig. 55: Schematic off cut substrate with a) Top view and b) Side view for different substrates

Table 14: Samples grown on 5 ° off cut STO (001)

Sample YBCO/LCMO	Thickness [Å]	off cut direction	c-axis lattice parameter [Å]	Sign of LITV signal in direction 1
YBCO 7	2000	+ 5 °	11.644 ± 0.002	Negative
LCMO 6	2000	+ 5 °	-	Negative
YBCO/LCMO 26	1000/1000	- 5 °	11.712 ± 0.004	Positive
YBCO/LCMO 27	2x 520/520	+ 5 °	11.712 ± 0.004	Negative
YBCO/LCMO 28	4x 260/260	+ 5 °	11.714 ± 0.011	Negative
YBCO/LCMO 29	8x 130/130	- 5 °	11.720 ± 0.005	Positive

XRD measurements show the c-axis oriented growth and the phase purity of the samples (c.f. see Fig. 56). The c-axis length of the samples was determined from the positions of the Bragg reflections θ from the XRD measurements and applying the Nelson Riley function [33]. Calculations of the oxygen content of YBCO using the c-axis lattice parameters were not accomplished for the samples on off cut STO. The peaks are broadened due to small variation in the off cut angle of the thin films. A rough estimation of the oxygen content using Liang et al. [54] as reference leads to a small oxygen deficiency for the investigated heterostructures and superlattices. The single layer YBCO 7 is regarded to be fully oxygenated with a superconducting transition temperature T_C of 89 K.
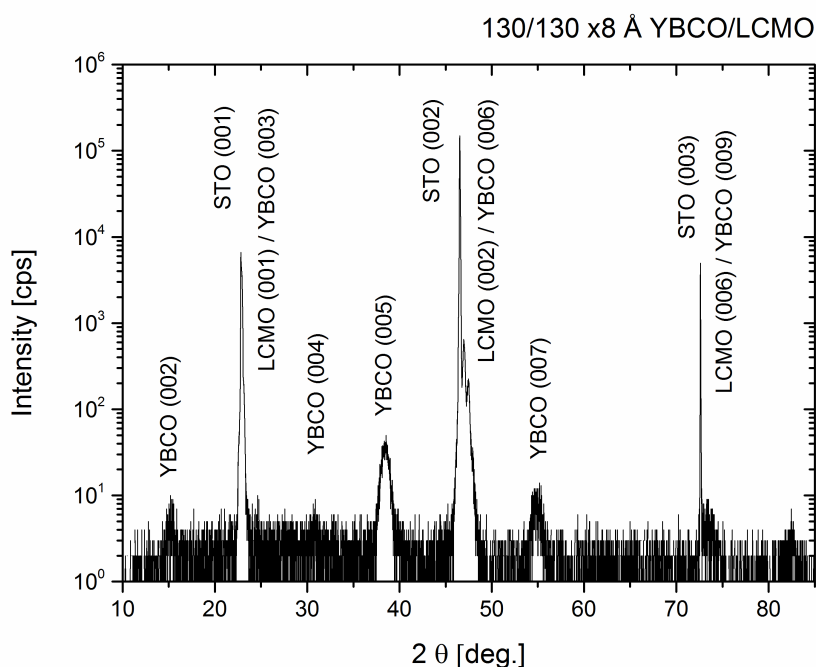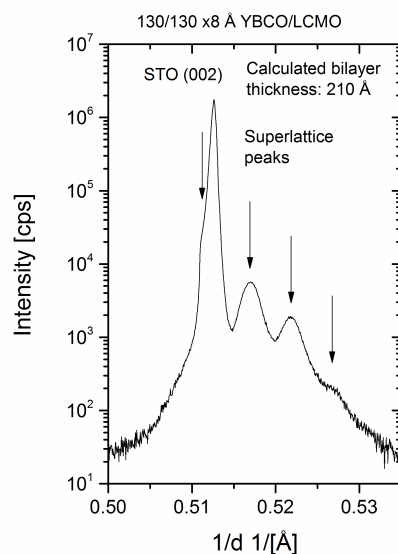

Fig. 56: XRD pattern of YBCO/LCMO 29 on STO (001) 5° off

High resolution scans (Fig. 57) were done to receive information about the samples quality and to calculate the bilayer thickness in the corresponding superlattice. The resulting thickness amounts to 210 Å, what is smaller than the designated bilayer thickness of 260 Å.


Fig. 57: Superlattice scan of YBCO/LCMO 29

The real tilting angle of the thin films is not necessarily identical to that of the substrate and can be examined using rocking curve measurements in the XRD. Therefore the samples are scanned for possible off cut positions of the thin films in a wide area. It is obvious, that the single layer LCMO 6 (c.f. see Fig. 58 a)) follows the off cut completely whereas the superlattice YBCO/LCMO 29 exhibits different off cut angles (Fig. 58 b)). Nevertheless the sample YBCO/LCMO 29 is dominated by an off cut angle of 5 ° (+/- 0.5 °). The differences might be due to the high amount of interfaces.
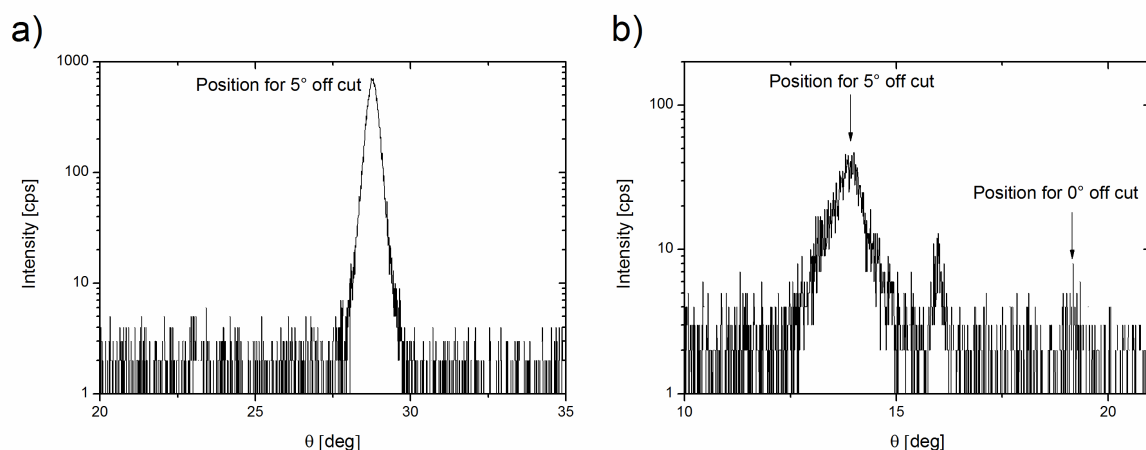
Fig. 58: a) Rocking curve of the (002) peak of LCMO 6 and b) Rocking curve of the (005) peak of YBCO/LCMO 29

The samples were wet chemical etched to a special L – shape structure, shown in Fig. 59. So it was possible to investigate at first the Seebeck-coefficient in the ZEM-3 longitudinal (properties of ab – plane) and transversal (properties of ab – plane and c-axis) to the tilt directions, second the LITV signal and third the resistance in a cryostat.
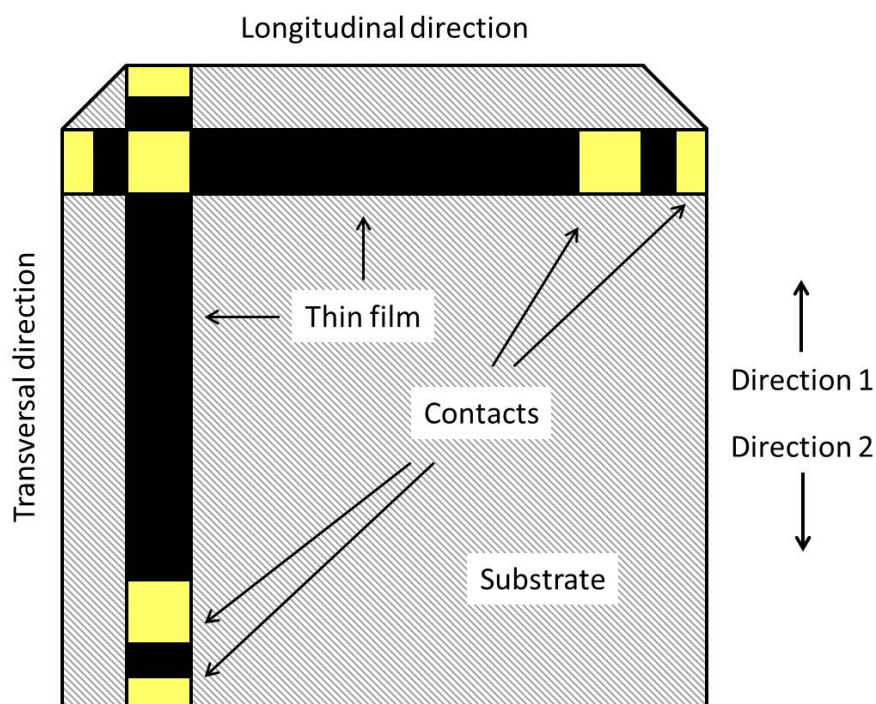
Fig. 59: L - shape structure of a thin film on STO

The first thermoelectric investigations were done in the ZEM. The Seebeck-coefficient was measured along and perpendicular to the off cut direction of the thin films and substrates. The results are illustrated in Fig. 60.
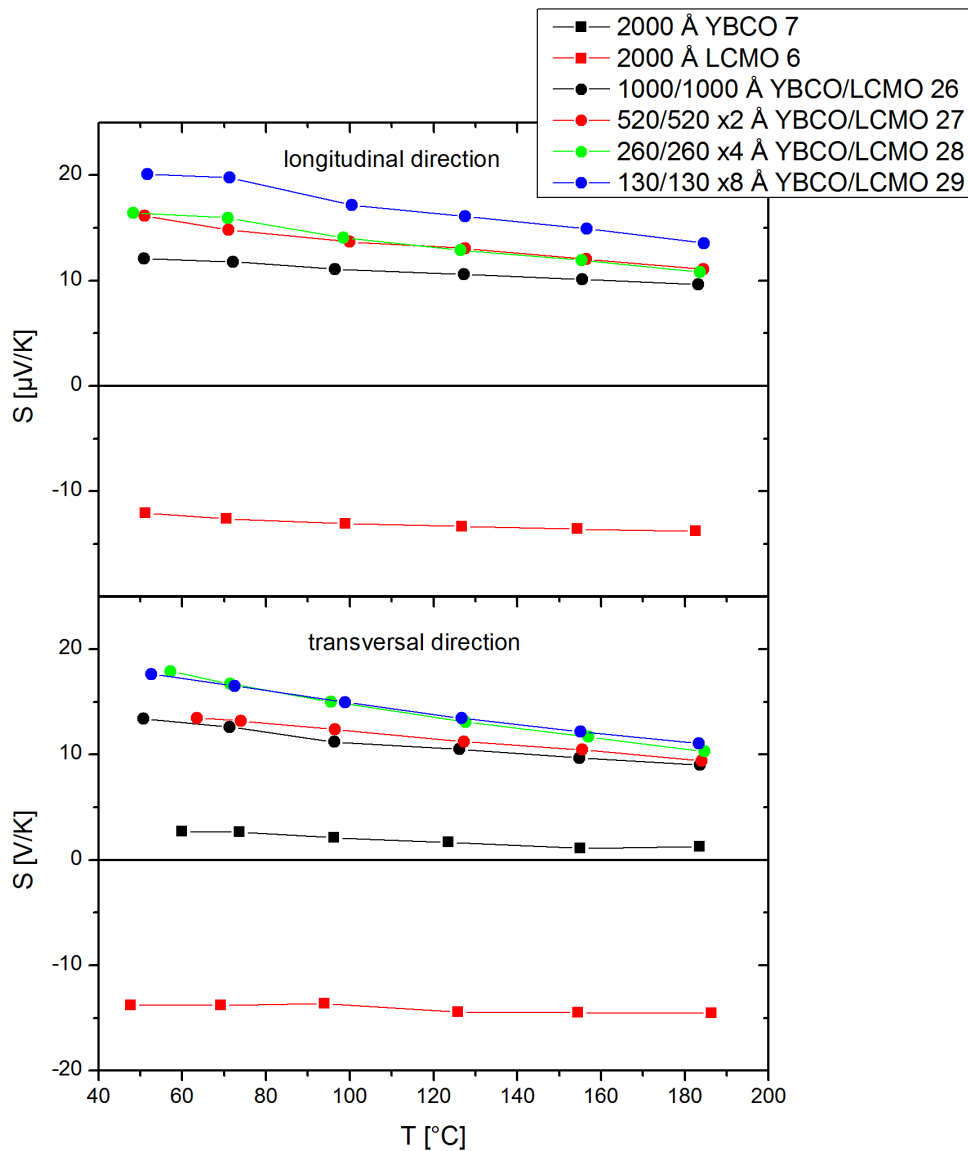

Fig. 60: Seebeck-coefficient of all samples for the longitudinal and transversal directions

The measured Seebeck-coefficient for both directions are in a good agreement with the results for planar samples. It is nearly zero for YBCO, negative for LCMO and positive for the heterostructures and superlattices. The longitudinal direction of YBCO 7 could not be determined because of contact problems. There are no obvious differences between the results of both directions larger than the error bar of

the measurement. Theoretically, there shouldn't be any differences between both directions according to Equation 35. The differences between both directions for the LCMO are maybe strain induced and very small. Measurable effects for the YBCO and the superlattices can only emerge if the Seebeck-coefficient of the c-axis ($S_c(T)$) is more than one magnitude larger than the Seebeck-coefficient of the ab-plane ($S_{ab}(T)$) according to Equation 35:

$$S = S_{ab} \times \cos^2 \alpha + S_c \times \sin^2 \alpha \ \ \text{or}$$
$$S = S_{ab} \times 0.992 + S_c \times 0.008 \ \ \text{for} \ \ \alpha = 5°$$

Equation 35

The samples were contacted to measure the anisotropic thermoelectric properties according to Fig. 59. All samples were measured using a broad range of energies in two directions. Starting with the lowest energy, it was increased to a maximum energy of 60 µJ to avoid laser induced degradations. Afterwards the scan was accomplished from the highest energy back to the lowest one. Effects resulting from possible damages of the samples due to a high energy impact could be examined by this method. For LCMO 6 it was not possible to detect a clear signal. The sample was measured up to higher energies and destroyed due to the high energy impact without detecting a clear signal. The only information that could be extracted is the sign of the LITV signal for direction 1 (negative LITV signal). This finding contrasts to previous results published by Habermeier et al. [90]. The reasons for the differences are seen in different sample microstructures, arising from different targets and deposition conditions used. To examine the signs of the signal, the samples were rotated by 180 ° after the first measurement and measured again as described. Whether a positive or negative signal appears, depends on different parameters:

1. The sign of S_{ab} and S_c (positive or negative).
2. If $|S_{ab}|$ is larger or lower than $|S_c|$.
3. The off cut and measurement direction of the sample.

The voltage signals and the energy density of the laser on the sample surface were measured and calculated as described in Chapter 4. 4. 3. Fig. 61 shows the LITV signal of sample YBCO/LCMO 29 at different energies for one direction as example.
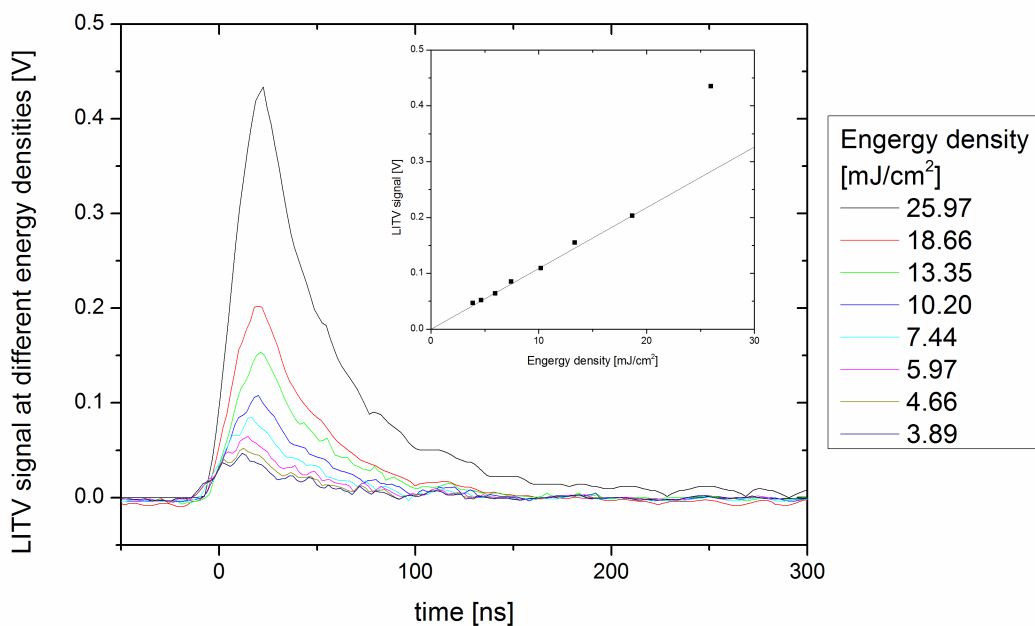
Fig. 61: LITV signal of YBCO/LCMO 29 at different energy densities; Inset shows the energy density dependence of the maximum voltage

It can be clearly seen, that the maximum voltage strongly depends on the energy density of the laser pulse. The inset in Fig. 61 shows the linear increase of the LITV signal with increasing energy density. Only the signal at higher energy density is not following the linear dependence. The same dependences were reported for single layer YBCO [86].

The reproducibility of the data for the voltage signal and the energy density is mainly determined by the stability of the photon flux of the laser used in the single shot mode. Consequently, all measurements were done five times at each energy density to reduce the influence of these fluctuations. An example for the fluctuations of the measured voltage signals and the energy densities is shown in Fig. 62 for YBCO/LCMO 29.
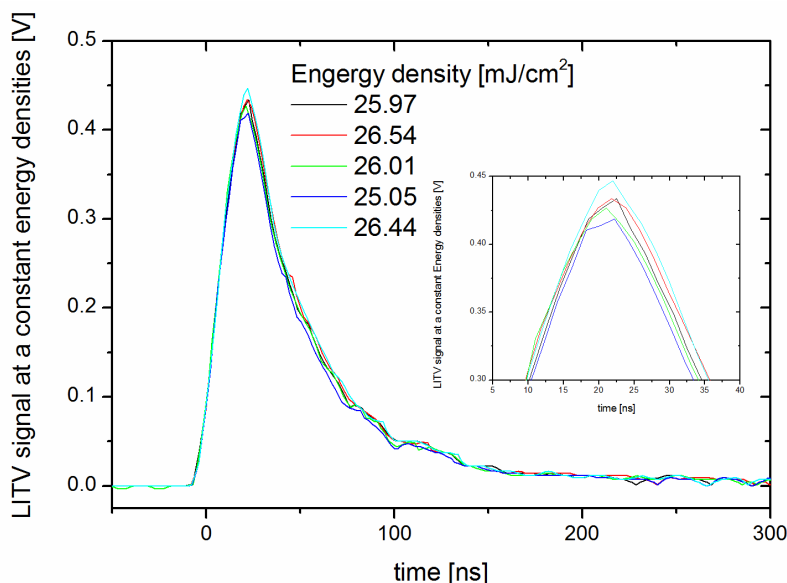
Fig. 62: LITV signal of YBCO/LCMO 29 at the same energy density with fluctuations

The measured signals were normalized by the energy density. The real signal was calculated afterwards using Equation 25 (c.f. see Chapter 4. 4. 3.) and the resistance at 295 K. Fig. 63 shows real signal normalized by the energy density of YBCO 7 and YBCO/LCMO 26 to 29 using nearly the same energy density for all samples.
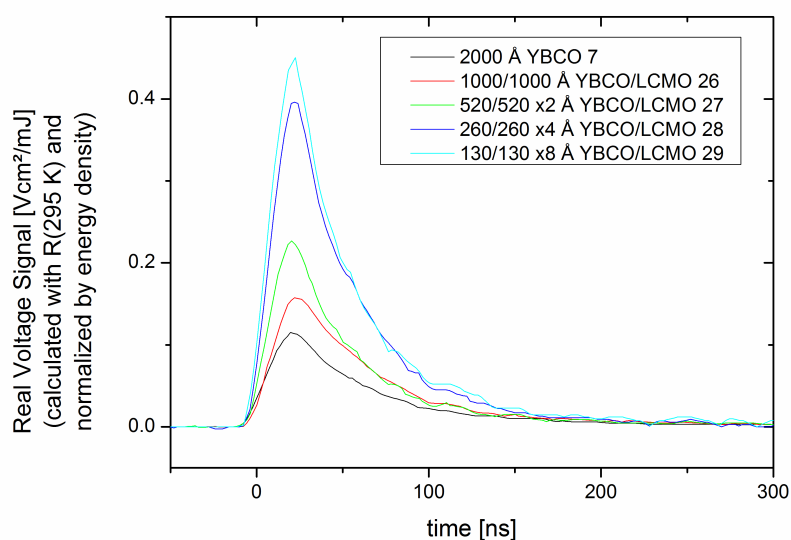

Fig. 63: Real voltage signal calculated with R (295 K) using Equation 25 and normalized by the energy density (The plotted voltage signals are representative examples for the corresponding sample)

Comparing the maxima of the normalized voltages of all samples, one realizes a clear dependence of the maximum voltages from the number of interfaces or the thickness of the single layer YBCO in the heterostructures and superlattices, respectively (Fig. 63). The normalized voltage signal increases with increasing number of interfaces (or decreasing YBCO thickness), whereas the smallest voltage was investigated for YBCO 7 and the largest one in YBCO/LCMO 29.

The maxima of the LITV signals of all samples generated with different energy densities and measured in both directions (examples shown in Fig. 61 and Fig. 62) were taken to summarize the results. The maxima were used to calculate the real voltage signal using Equation 25. The results of the calculations are shown in Fig. 64, where the real voltage signals were plotted versus the energy density. The plot includes the results measured for both directions and the results measured with increasing and decreasing energy density.
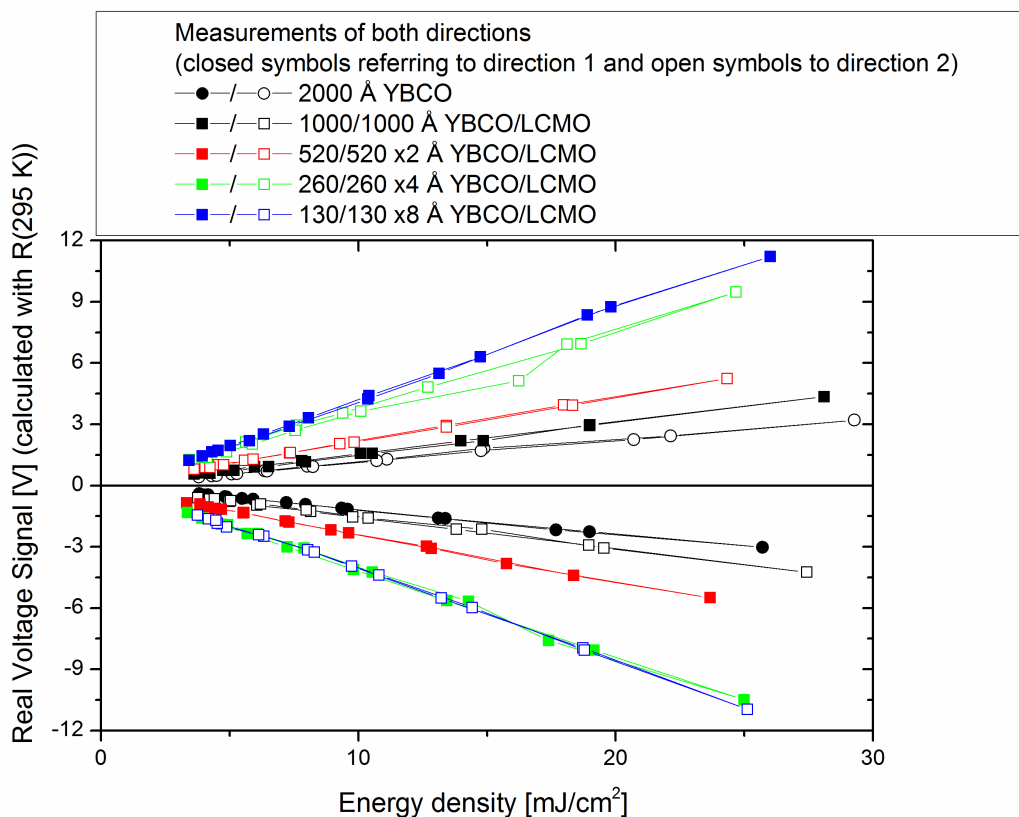

Fig. 64: Calculated voltages in dependence of the laser energies on the surface

Concerning one direction, the absolute real voltage signal increases linearly with increasing energy density for all samples. Also the real voltage signals decrease with decreasing energy density for the same direction. So the results of the measurements done with increasing and decreasing energy density overlap. Subsequent, any damage or modifications of the samples during the measurements and significant heating effects can be excluded.

As mentioned before, the sign of the LITV signal depends on different criteria. It is well known, that the LITV signal U of optimally doped single layer YBCO is negative for samples with an off cut of "+" 5 ° according to Equation 20:

$$U = \frac{l}{2t}(S_{ab} - S_c)\Delta T \sin 2\alpha$$ **Equation 20**

where $\Delta S = S_{ab} - S_c$ should be negative for optimally doped YBCO ($\delta = 0.05$) because S_{ab} exhibits a negative and S_c a positive sign [17, 18]. Even for slightly underdoped YBCO ($\delta = 0.1$) ΔS is negative because $|S_{ab}| < |S_c|$ [17, 18]. Following this argumentat, the LITV signals measured for YBCO 7 in direction 1 represent the realistic sign of the LITV signal. Subsequent, all samples with a negative LITV signal measured in direction 1 and an off cut of "+" 5 ° should exhibit a negative ΔS. The positive sign for the measurements of the samples YBCO/LCMO 26 and 29 occurs because of the off cut of "-" 5 °. Consequently, the original ΔS are negative for all samples.

The negative ΔS could result from different origins:
      1. S_{ab} and S_c are both negative and $|S_{ab}| > |S_c|$.
      2. S_{ab} and S_c are both positive and $|S_{ab}| < |S_c|$.
   3. S_{ab} is negative and S_c is positive.

Case 3 applies for single layer optimally doped YBCO as discussed before. The in plane Seebeck-coefficient S_{ab} is always positive at room temperature for YBCO/LCMO heterostructures and superlattice as discussed in the previous chapters, so case 1 can be excluded and case 2 applies. Following these results the

findings examined using the LITV measurements can only be explained by a positive S_c larger than S_{ab} in the heterostructures and superlattices. The Seebeck-coefficient S_c of YBCO/LCMO 26 to 29 arises from a combination of the Seebeck-coefficients S and the thermal conductivity κ of single layer YBCO and LCMO according to Kirchhoff's law (c.f. see Chapter 2.2.):

$$S_c = \frac{\dfrac{S_{c-YBCO} \times t_{c-YBCO}}{\kappa_{c-YBCO}} + \dfrac{S_{LCMO} \times t_{LCMO}}{\kappa_{LCMO}}}{\dfrac{t_{c-YBCO}}{\kappa_{c-YBCO}} + \dfrac{t_{LCMO}}{\kappa_{LCMO}}}$$

Equation 36

The absolute values of the c-axis Seebeck-coefficient of YBCO (10 µV/K [18]; 25 µV/K [17]) and the Seebeck-coefficient of LCMO (- 10 µV/K to - 15 µV/K) at room temperature are nearly the same. Also the thermal conductivity measured for YBCO single crystals (2.5 W/m/K [18]) and polycrystalline LCMO (1 W/m/K to 2 W/m/K [96]) are in the same order of magnitude. But a rough estimation shows a positive result for S_c what finally can be the reason for the negative LITV signal.

The calculated voltages were normalized by the energy density and plotted versus the number of interfaces in the heterostructures and superlattice (Fig. 65). One can clearly see the linear dependence of the signal from the number of interfaces. Only the sample with the highest number of interfaces (YBCO/LCMO 29 with 15 interfaces) is not following the linear behavior. This could result from a gradual change of the off cut angle in the sample from the first layer on the substrate to the last layer on the surface of the sample. Inhomogeneities of the off cut angle were shown by XRD measurements (c.f. see Fig. 58 b)). A decrease of the off cut angle in some parts of the thin films can reduce the LITV signal according to Equation 20.
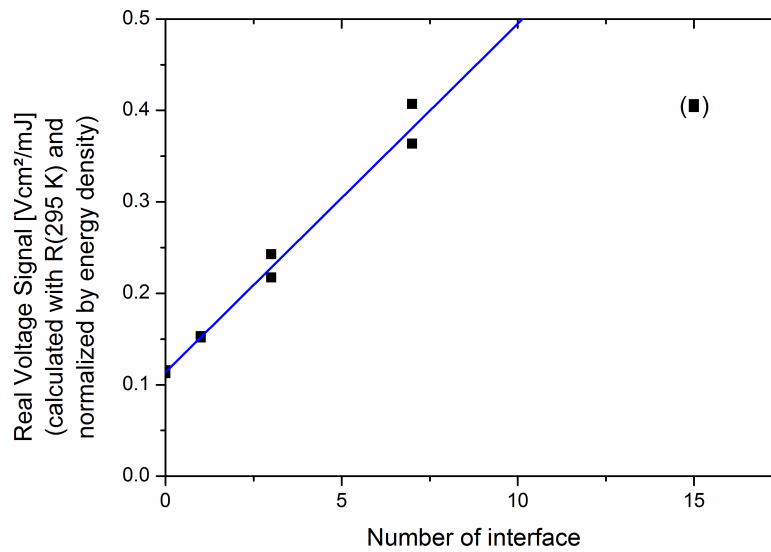
Fig. 65: Normalized voltages in dependence of the number of interfaces

Assuming all investigated samples exhibit nearly the same thicknesses and off cut angles and the length of the incident laser spot was the same for all samples, Equation 37 can be reduced to:

$$U \approx 825 \times \Delta S \Delta T$$

Equation 37

with $l = 1.9$ mm, $t = 2000$ Å and $|\alpha| = 5$ °. The increase of the voltage shown in Fig. 65 can occur from changes in ΔS or ΔT. An increase of ΔS can be possible, if S_c increases stronger than S_{ab} (increasing S_{ab} with increasing number of interfaces was investigated for superlattices on NGO). An enhancement of the temperature gradient with increasing number of interfaces can result since the phonons are scattered at the interfaces between YBCO and LCMO.

In summary, the LITV signals of YBCO, LCMO as well as heterostructures and superlattices were investigated. A linear dependences of the LITV signal from the energy density was found for all samples similar to the investigation of different groups for single layer thin films before. It turned out that only a positive Seebeck-coefficient in the c-axis direction of the samples can be responsible for a negative LITV signal. Most important, it could be shown that the LITV signal can be enhanced tremendous due to superlattice formation as compared to the single layer material, even using the same total sample thickness and energy densities.

Chapter 6

Summary

The thermoelectric properties and the electrical conductivity of $YBa_2Cu_3O_{7-\delta}$ (YBCO), $La_{2/3}Ca_{1/3}MnO_3$ (LCMO) thin films as well as heterostructures and superlattices of both materials were investigated in this thesis. The thin films were grown on different substrates ($SrTiO_3$, $(La_{0.27}Sr_{0.73})(Al_{0.65}Ta_{0.35})O_3$, $NdGaO_3$) by pulsed laser deposition techniques and studied in different temperature ranges (20 K to 390 K or 320 K to 750 K), partially with applied magnetic fields. Whereas the investigations of single layer $YBa_2Cu_3O_{7-\delta}$ and $La_{2/3}Ca_{1/3}MnO_3$ are in a good agreement with the finding reported in the literature, heterostructures and superlattices of both materials were studied the first time in this thesis. The Seebeck-coefficients of the heterostructures and superlattices are always positive between 20 K and 390 K, while the Seebeck-coefficient is small and negative for optimal doped single layer YBCO and negative for single layer LCMO, respectively. The results can not be explained by a superposition of the physical properties of single layer materials according to Kirchhoff's law. The findings are addressed to an interface which exhibits different physical properties compared to single layer material. The interface also influences the properties of both materials over a long range.

Single layer thin films of YBCO with different oxygen contents were grown on STO. The thin films were single phase grown, shown by XRD measurements. The Seebeck-coefficients found for optimal doped YBCO are small ($S(T) < \pm 2$ µV/K) and positive for underdoped YBCO, what is in a good agreement with earlier reports. Also the LCMO single layer thin films grown on different substrates were examined. According to XRD investigations, the thin films were single phase grown and c-axis oriented. The studies of the films grown on different substrates could show the independence of the thermoelectric properties from the substrate. The results are in a perfect agreement with the values reported in the literature before. In addition, the

existence of small polarons in the paramagnetic state reported by different groups could be confirmed.

Heterostructures consisting of YBCO and LCMO were grown under identical conditions like single layers of YBCO and LCMO thin films to guarantee the same growth conditions. The individual single layer thicknesses of the particular materials are ranging from 500 Å to 1000 Å. It could be shown, that the samples were partially oxygen deficient, depending on the preparation conditions. The Seebeck-coefficients investigated in these structures can not be explained by a superposition of the physical properties of single layer YBCO and LCMO thin film according to Kirchhoff's law. Only using the physical properties of underdoped YBCO for these calculations leads to results similar to the experimental findings. Elongated annealing times in oxygen atmosphere result in an optimized oxygen content for YBCO. Finally, the findings can be explained by an overlap of the physical properties of incomplete oxidized YBCO layers and the interactions between YBCO and LCMO.

Superlattices grown on STO (deposition parameters identical to YBCO and LCMO single layer thin films) show similar results compared to the heterostructures. In contrast, it could be shown by XRD, RSM and Raman investigations, that the samples were completely oxidized and grow strain free c-axis oriented. The differences in the oxygen content were addressed to the different crystallographic properties of YBCO in the heterostructures and superlattices. After ruling out strain and a lowered oxygen content of YBCO as origin for the findings, the investigated effects were addressed to long range interactions generated at the interface between YBCO and LCMO. The properties of the interface itself could not be investigated due to its high resistivity.

The thermoelectric properties of YBCO, LCMO as well as heterostructures and superlattices of both materials grown on NGO were investigated as comparative study to receive information about possible substrate induced effects. In contrast to the samples grown on STO, theses samples were treated with a second annealing step after the deposition and the Seebeck-coefficients were monitored during this procedure. The oxygen contents of all samples grown on NGO were optimized

during the annealing step. The investigations of the Seebeck-coefficient result in a clear dependence of the Seebeck-coefficient from the number of interfaces in the heterostructures and superlattices. The Seebeck-coefficients increase with increasing number of interfaces in the structures. The investigations at low temperatures result in a qualitative reproduction of the findings for the samples on STO. The origin of the differences of the absolute values could not be identified till now. Nevertheless, the results show, that the findings are not substrate related.

Investigations of heterostructures consisting of PBCO and LCMO were accomplished to receive information about the influence of the contact mechanism on the measurements at low temperatures. The investigations show, that the Seebeck-coefficients are independent on the contact mechanism and not influenced by the contacts.

The investigations of YBCO, LCMO and heterostructures and superlattices of both materials on tilted STO substrates were done to investigate the anisotropic transport properties and the components of the Seebeck tensor. It could be shown, that the normalized LITV signal increases linear with the number of interfaces in the structures. Subsequently, the LITV signal can be tremendously enhanced due to superlattice formation.

The studies done in this thesis show, that the investigations of the thermoelectric properties of superlattices are an excellent tool to study the physical properties of the superlattices. The studies can be seen as complementary to the measurements done using explorations of the electrical conductivity, the magnetic properties and Hall coefficient for the superlattices. Also, it could be shown, that a superlattice formation can lead to a strong enhancement of the Seebeck-coefficient compared to the single layer material.

Chapter 7

Zusammenfassung

Diese Arbeit befasst sich mit der Untersuchung der thermoelektrischen Eigenschaften und der elektrischen Leitfähigkeit dünner Schichten von $YBa_2Cu_3O_{7-\delta}$ (YBCO), $La_{2/3}Ca_{1/3}MnO_3$ (LCMO) sowie von Heterostrukturen und Übergittern beider Materialien. Die dünnen Schichten wurden mittels Gepulster Laser Deposition (PLD) auf verschiedenen Substraten ($SrTiO_3$ (STO), $(La_{0,27}Sr_{0,73})(Al_{0,65}Ta_{0,35})O_3$ (LSAT); $NdGaO_3$ (NGO)) abgeschieden und in verschiedenen Temperaturbereichen (20 K bis 390 K oder 320 K bis 750 K) untersucht, teilweise auch unter Einwirkung eines Magnetfeldes. Während die Ergebnisse der Untersuchungen der $YBa_2Cu_3O_{7-\delta}$ und $La_{2/3}Ca_{1/3}MnO_3$ Einzelschichten in Einklang mit bereits publizierten Werten stehen, wurden die thermoelektrischen Eigenschaften von Heterostrukturen und Übergittern beider Materialien in dieser Arbeit erstmalig untersucht. Während die Seebeck-Koeffizienten von optimal dotierten YBCO Einzelschichten sehr klein und negativ und für LCMO Einzelschichten negativ sind, zeigen die Heterostrukturen und Übergitter in einem Temperaturbereich von 20 K bis 390 K immer positive Seebeck-Koeffizienten. Diese Ergebnisse können nicht mit einer Überlagerung der physikalischen Eigenschaften der Einzelschichten unter Verwendung des Kirchhoffschen Gesetzes erklärt werden. Der Ursprung der gefundenen Effekte wurde der Grenzfläche zwischen beiden Materialien zugeschrieben. Diese weist Eigenschaften auf, die sich von denen der Einzelschichten der Materialien unterscheiden und beeinflusst die Eigenschaften beider Materialien in den Strukturen langreichweitig.

YBCO Einzelschichten mit verschiedenen Sauerstoffgehalten wurden auf STO abgeschieden. Durch Röntgenmessungen konnte gezeigt werden, dass die dünnen Schichten einphasig gewachsen sind. Die gemessenen Seebeck-Koeffizienten von optimal dotiertem YBCO sind klein ($S(T) < \pm 2 \, \mu V/K$) und bei unterdotiertem YBCO positiv, was in guter Übereinstimmung mit den bereits veröffentlichten Werten steht.

Ebenso wurden LCMO Einzelschichten, die auf verschiedenen Substraten abgeschieden wurden, untersucht. Röntgenmessungen ergaben, dass diese dünnen Schichten einphasig und c-Achsen orientiert (in kubischer Notation) gewachsen sind. Die Untersuchungen der Proben zeigen, dass die thermoelektrischen Eigenschaften unabhängig vom Substrat sind, auf dem die Proben abgeschieden wurden. Die Ergebnisse stimmen perfekt mit den von verschiedenen Gruppen publizierten Werten überein. Die Ergebnisse bestätigen auch Berichte verschiedener Gruppen über das Vorhandensein von kurzreichweitigen polaronischen Wechselwirkungen im paramagnetischen Zustand.

Um identische Wachstumsbedingungen zu gewährleisten, wurden Heterostrukturen bestehend aus YBCO und LCMO mit den selben Wachstumsparametern hergestellt, die auch für die Abscheidung der Einzelschichten verwendet wurden. Die Dicken der Einzelschichten der jeweiligen Materialien in den Heterostrukturen reichten von 500 Å bis 1000 Å. Es konnte gezeigt werden, dass die so hergestellten Proben teilweise sauerstoffdefizitär waren. Die an diesen Strukturen gemessenen Seebeck-Koeffizienten können nicht durch eine Überlagerung der physikalischen Eigenschaften der YBCO und LCMO Einzelschichten unter Benutzung des Kirchhoffschen Gesetzes erklärt werden. Nur unter Verwendung der Messwerte von unterdotiertem YBCO für diese Berechnungen konnten Werte errechnet werden, die den experimentellen Werten gleichen. Durch ein verlängertes Auslagern der Proben in einer Sauerstoffatmosphäre konnte ein optimaler Sauerstoffgehalt der YBCO Schichten in den Heterostrukturen erreicht werden. Die für die Heterostrukturen ermittelten Eigenschaften konnten somit durch eine Überlagerung der physikalischen Eigenschaften von unterdotiertem YBCO mit den Wechselwirkungen zwischen YBCO und LCMO erklärt werden.

Die Untersuchungen der Übergitter, die auf STO abgeschieden wurden (Abscheidungsparameter identisch zu den YBCO und LCMO Einzelschichten), führen zu ähnlichen Ergebnissen, wie sie bei den Heterostrukturen gefunden wurden. Auch bei diesen Strukturen konnten die ermittelten Werte nicht durch eine Überlagerung der physikalischen Eigenschaften der Einzelschichten erklärt werden. Bei den Übergittern konnte, im Gegensatz zu den Heterostrukturen, unter

Verwendung verschiedener Methoden (XRD, RSM, Raman) festgestellt werden, dass diese einen optimalen Sauerstoffgehalt aufweisen und spannungsfrei und c-Achsen orientiert gewachsen sind. Die Unterschiede im Sauerstoffgehalt resultieren aus den unterschiedlichen kristallographischen Eigenschaften der YBCO Schichten in den Heterostrukturen und Übergittern. Substratinduzierte Spannungen und ein verringerter Sauerstoffgehalt des YBCO konnten somit als Ursache der ermittelten Seebeck-Koeffizienten ausgeschlossen werden. Als Ursache der gefundenen Effekte werden langreichweitige Effekte vermutet, die in der Grenzfläche zwischen YBCO und LCMO induziert werden. Die Eigenschaften der Grenzfläche konnten auf Grund ihres hohen Widerstandes nicht aus den Messwerten ermittelt werden.

Die Untersuchungen der thermoelektrischen Eigenschaften von dünnen Schichten, die auf NGO abgeschieden wurden (Einzelschichten von YBCO, LCMO sowie von Heterostrukturen und Übergitter beider Materialien), dienten als Vergleichsstudie, um Aufschluss über mögliche substratinduzierte Effekte zu erhalten. Die auf NGO gewachsenen Proben wurden einem zusätzlichen Auslagerungsschritt unterzogen, im Gegensatz zu den auf STO abgeschiedenen Proben. Dadurch konnte eine Optimierung des Sauerstoffgehalts für alle auf NGO abgeschiedenen Proben erreicht werden. Die Untersuchungen ergaben eine klare Abhängigkeit des Seebeck-Koeffizienten von der Anzahl der Grenzflächen in den Heterostrukturen und Übergittern, wobei der Seebeck-Koeffizient mit zunehmender Anzahl an Grenzflächen ansteigt. Die Ergebnisse der Untersuchungen bei tiefen Temperaturen zeigen eine qualitative Übereinstimmung mit den Messwerten der Proben, die auf STO abgeschieden wurden. Die Ursache für die Unterschiede in den absoluten Messwerten konnte nicht abschließend ermittelt werden. Dennoch konnte durch dieses Experiment gezeigt werden, dass die gefundenen Effekte nicht substratinduziert sind.

Um Informationen über mögliche Einflüsse der Kontaktierung auf die Messergebnisse zu erhalten, wurden Untersuchungen von Heterostrukturen bestehend aus PBCO und LCMO durchgeführt. Es konnte gezeigt werden, dass die gemessenen Seebeck-Koeffizienten unabhängig vom Kontaktmechanismus

(Kontakte nur auf der obersten Schicht oder über alle Schichten) sind und auch nicht von den Kontakten beeinflusst werden.

Weitere Studien wurden durchgeführt, um Informationen über die anisotropen Eigenschaften des Seebeck-Koeffizienten und die Komponenten des Seebeck-Tensors zu erhalten. Dazu wurden dünne Schichten von YBCO, LCMO sowie Heterostrukturen und Übergitter beider Materialien auf verkippten STO Substraten abgeschieden. Die Untersuchungen erfolgten mittels der so genannten Laser induzierten thermoelektrischen Spannung (LITV). Dabei wird durch optische Anregung ein Temperaturgradient senkrecht zur Oberfläche der dünnen Schicht und dadurch Spannungspuls entlang der Probe erzeugt. Es konnte gezeigt werden, dass das normierte LITV Signal linear mit der Anzahl der Grenzflächen in den Strukturen ansteigt. Das LITV Signal kann somit durch die Erzeugung von Übergittern im Vergleich zu den Einzelschichten dramatisch erhöht werden.

Durch diese Arbeit konnte gezeigt werden, dass mit der Untersuchung der thermoelektrischen Eigenschaften von Heterostrukturen und Übergittern eine ausgezeichnete Methode zur Verfügung steht, um Informationen über die physikalischen Eigenschaften dieser Strukturen zu erhalten. Die Untersuchungen der Seebeck-Koeffizienten können als komplementäre Studien zu den Untersuchungen der elektrischen Leitfähigkeit, den magnetischen Eigenschaften und den Hall Koeffizienten betrachtet werden. Es konnte dabei gezeigt werden, dass der Seebeck-Koeffizient durch die Erzeugung von Übergittern im Vergleich zu den Einzelschichten der verwendeten Materialien enorm gesteigert werden kann.

References

1. Dresselhaus, M.S., G. Chen, M.Y. Tang, R.G. Yang, H. Lee, D.Z. Wang, Z.F. Ren, J.P. Fleurial, and P. Gogna, *New directions for low-dimensional thermoelectric materials.* Advanced Materials **19**, 1043-1053 (2007).
2. Pichanusakorn, P. and P. Bandaru, *Nanostructured thermoelectrics.* Materials Science & Engineering R-Reports **67**, 19-63 (2010).
3. Ohta, H., *Thermoelectrics based on strontium titanate.* Materials Today **10**, 44-49 (2007).
4. Gregori, G., S. Heinze, P. Lupetin, H.U. Habermeier, and J. Maier, *Seebeck coefficient and electrical conductivity of mesoscopic nanocrystalline SrTiO3.* Journal of Materials Science **48**, 2790-2796 (2013).
5. Holden, T., H.U. Habermeier, G. Cristiani, A. Golnik, A. Boris, A. Pimenov, J. Humlicek, O.I. Lebedev, G. Van Tendeloo, B. Keimer, and C. Bernhard, *Proximity induced metal-insulator transition in YBa2Cu3O7/La2/3Ca1/3MnO3 superlattices.* Physical Review B **69**, 064505 (2004).
6. Sefrioui, Z., D. Arias, V. Peña, J.E. Villegas, M. Varela, P. Prieto, C. León, J.L. Martinez, and J. Santamaria, *Ferromagnetic/superconducting proximity effect in La{0.7}Ca{0.3}MnO{3}/YBa{2}Cu{3}O{7-δ} superlattices.* Physical Review B **67**, 214511 (2003).
7. Chakhalian, J., J.W. Freeland, G. Srajer, J. Strempfer, G. Khaliullin, J.C. Cezar, T. Charlton, R. Dalgliesh, C. Bernhard, G. Cristiani, H.U. Habermeier, and B. Keimer, *Magnetism at the interface between ferromagnetic and superconducting oxides.* Nature Physics **2**, 244-248 (2006).
8. Chakhalian, J., J.W. Freeland, H.U. Habermeier, G. Cristiani, G. Khaliullin, M. van Veenendaal, and B. Keimer, *Orbital reconstruction and covalent bonding at an oxide interface.* Science **318**, 1114-1117 (2007).
9. Habermeier, H.U., G. Cristiani, R.K. Kremer, O. Lebedev, and G. van Tendeloo, *Cuprate/manganite superlattices - A model system for a bulk ferromagnetic superconductor.* Physica C **364**, 298-304 (2001).
10. Driza, N., S. Blanco-Canosa, M. Bakr, S. Soltan, M. Khalid, L. Mustafa, K. Kawashima, G. Christiani, H.U. Habermeier, G. Khaliullin, C. Ulrich, M. Le Tacon, and B. Keimer, *Long-range transfer of electron-phonon coupling in oxide superlattices.* Nature Materials **11**, 675-681 (2012).
11. Lengfellner, H., S. Zeuner, W. Prettl, and K.F. Renk, *Thermoelectric effect in normal-state YBa2Cu3O7-delta films.* Europhysics Letters **25**, 375-378 (1994).
12. Renk, K.F., J. Betz, S. Zeuner, H. Lengfellner, and W. Prettl, *Thermopile effect due to laser-radiation heating in thin-films of high-t-c materials.* Physica C **235**, 37-40 (1994).
13. LeBoeuf, D., N. Doiron-Leyraud, B. Vignolle, M. Sutherland, B.J. Ramshaw, J. Levallois, R. Daou, F. Laliberte, O. Cyr-Choiniere, J. Chang, Y.J. Jo, L. Balicas, R.X. Liang, D.A. Bonn, W.N. Hardy, C. Proust, and L. Taillefer, *Lifshitz critical point in the cuprate superconductor YBa2Cu3Oy from high-field Hall effect measurements.* Physical Review B **83**, 054506 (2011).
14. Doiron-Leyraud, N. and L. Taillefer, *Quantum critical point for stripe order: An organizing principle of cuprate superconductivity.* Physica C-Superconductivity and Its Applications **481**, 161-167 (2012).
15. Ghiringhelli, G., M. Le Tacon, M. Minola, S. Blanco-Canosa, C. Mazzoli, N.B. Brookes, G.M. De Luca, A. Frano, D.G. Hawthorn, F. He, T. Loew, M.M. Sala, D.C. Peets, M. Salluzzo, E. Schierle, R. Sutarto, G.A. Sawatzky, E. Weschke, B. Keimer, and L. Braicovich, *Long-Range Incommensurate Charge Fluctuations in (Y,Nd)Ba2Cu3O6+x.* Science **337**, 821-825 (2012).

16. Friedmann, T.A., M.W. Rabin, J. Giapintzakis, J.P. Rice, and D.M. Ginsberg, *Direct measurement of the anisotropy of the resistivity in the a-b plane of twin-free, single-crystal, superconducting YBa{2}Cu{3}O{7-δ}.* Physical Review B **42**, 6217-6221 (1990).

17. Cochrane, J.W. and G.J. Russell, *Activation energies for ultrahigh purity YBCO single crystals.* Superconductor Science & Technology **11**, 1105-1111 (1998).

18. Shams, G.A., J.W. Cochrane, and G.J. Russell, *Thermal conductivity and thermoelectric power of high-quality YBa2Cu3O7-delta crystals.* Physica C **363**, 243-250 (2001).

19. Shams, G.A., J.W. Cochrane, and G.J. Russell, *Thermal transport in polycrystalline YBa2Cu3O7-[delta], Y2BaCuO5 and melt-processed YBa2Cu3O7-[delta] materials.* Physica C: Superconductivity **351**, 449-465 (2001).

20. S.-W. Cheong, H.Y.H., *Ferromagnetism vs charge/orbital ordering in mixed-valent manganites, in: Y. Tokura (Ed.), Colossal Magnetoresistance Oxides Monographs in Condensed Matter Science, Gordon & Breach, London.* (1999).

21. Jaime, M., M.B. Salamon, M. Rubinstein, R.E. Treece, J.S. Horwitz, and D.B. Chrisey, *High-temperature thermopower in La2/3Ca1/3MnO3 films: Evidence for polaronic transport.* Physical Review B **54**, 11914-11917 (1996).

22. Hundley, M.F. and J.J. Neumeier, *Thermoelectric power of La1-xCaxMnO3+delta: Inadequacy of the nominal Mn3+/4+ valence approach.* Physical Review B **55**, 11511-11515 (1997).

23. Salamon, M.B. and M. Jaime, *The physics of manganites: Structure and transport.* Reviews of Modern Physics **73**, 583-628 (2001).

24. Palstra, T.T.M., A.P. Ramirez, S.W. Cheong, B.R. Zegarski, P. Schiffer, and J. Zaanen, *Transport mechanisms in doped LaMnO3: Evidence for polaron formation.* Physical Review B **56**, 5104-5107 (1997).

25. Stahn, J., J. Chakhalian, C. Niedermayer, J. Hoppler, T. Gutberlet, J. Voigt, F. Treubel, H.U. Habermeier, G. Cristiani, B. Keimer, and C. Bernhard, *Magnetic proximity effect in perovskite superconductor/ferromagnet multilayers.* Physical Review B **71**, 140509(R) (2005).

26. Habermeier, H.U., *Critical temperatures in ferromagnetic-superconducting all-oxide superlattices.* Journal of Superconductivity **17**, 15-20 (2004).

27. Malik, V.K., I. Marozau, S. Das, B. Doggett, D.K. Satapathy, M.A. Uribe-Laverde, N. Biskup, M. Varela, C.W. Schneider, C. Marcelot, J. Stahn, and C. Bernhard, *Pulsed laser deposition growth of heteroepitaxial YBa2Cu3O7/La0.67Ca0.33MnO3 superlattices on NdGaO3 and Sr0.7La0.3Al0.65Ta0.35O3 substrates.* Physical Review B **85**, 054514 (2012).

28. Ziese, M., H.C. Semmelhack, K.H. Han, S.P. Sena, and H.J. Blythe, *Thickness dependent magnetic and magnetotransport properties of strain-relaxed La0.7Ca0.3MnO3 films.* Journal of Applied Physics **91**, 9930-9936 (2002).

29. Hoffmann, A., S.G.E. te Velthuis, Z. Sefrioui, J. Santamaria, M.R. Fitzsimmons, S. Park, and M. Varela, *Suppressed magnetization in La0.7Ca0.3MnO3/YBa2Cu3O7-delta superlattices.* Physical Review B **72**, 140407(R) (2005).

30. Kawashima, J., Y. Yamada, and I. Hirabayashi, *Critical thickness and effective thermal expansion coefficient of YBCO crystalline film.* Physica C **306**, 114-118 (1998).

31. Shayduk, R., H. Navirian, W. Leitenberger, J. Goldshteyn, I. Vrejoiu, M. Weinelt, P. Gaal, M. Herzog, C.V. Schmising, and M. Bargheer, *Nanoscale heat transport studied by high-resolution time-resolved x-ray diffraction.* New Journal of Physics **13**, 093032 (2011).

32. *CrysTec GmbH (http://www.crystec.de/crystec-d.html).*

33. Nelson, J.B. and D.P. Riley, *An experimental investigation of extrapolation methods in the derivation of accurate unit-cell dimensions of crystals.* Proceedings of the Physical Society of London **57**, 160-177 (1945).

34. *Quantum Design; Physical Properties Measurement System; Thermal Transport Option User's Manual*

35. Cohn, J.L., E.F. Skelton, S.A. Wolf, and J.Z. Liu, *Inplane thermoelectric power of untwinned YBa2Cu3O7-DELTA.* Physical Review B **45**, 13140-13143 (1992).

36. Laliberte, F., J. Chang, N. Doiron-Leyraud, E. Hassinger, R. Daou, M. Rondeau, B.J. Ramshaw, R. Liang, D.A. Bonn, W.N. Hardy, S. Pyon, T. Takayama, H. Takagi, I. Sheikin, L. Malone, C. Proust, K. Behnia, and L. Taillefer, *Fermi-surface reconstruction by stripe order in cuprate superconductors.* Nature Communications **2**, 1-6 (2011).

37. Goncalves, A.P., I.C. Santos, E.B. Lopes, R.T. Henriques, M. Almeida, and M.O. Figueiredo, *Transport-properties of the oxides Y1-xRrxBa2Cu3O7-delta (0-less-than-or-equal-to-x-less-than-or-equal-to-1) - effects of band filling and lattice distortion on superconductivity.* Physical Review B **37**, 7476-7481 (1988).

38. Ouseph, P.J. and M.R. O'Bryan, *Thermoelectric power of YBa{2}Cu{3}O{7-δ}.* Physical Review B **41**, 4123-4125 (1990).

39. Nowotny, J., M. Rekas, and W. Weppner, *Defect equilibria and transport in YBa2Cu3O7-x at elevated-temperatures .1. Thermopower, electrical-conductivity, and galvanic cell studies.* Journal of the American Ceramic Society **73**, 1040-1047 (1990).

40. Molenda, J., A. Stoklosa, and T. Bak, *Transport properties of YBa2Cu3O7-y at high temperatures.* Physica C: Superconductivity **175**, 555-565 (1991).

41. Cooper, J.R., S.D. Obertelli, A. Carrington, and J.W. Loram, *Effect of oxygen depletion on the transport-properties of YBa2Cu3O7-delta.* Physical Review B **44**, 12086-12089 (1991).

42. Obertelli, S.D., J.R. Cooper, and J.L. Tallon, *Systematics in the thermoelectric power of high-Tc oxides.* Physical Review B **46**, 14928 (1992).

43. Cochrane, J.W., G.J. Russell, and D.N. Matthews, *Seebeck coefficient as an indicator of oxygen content in YBCO.* Physica C: Superconductivity **232**, 89-92 (1994).

44. Mosqueira, J., J.A. Veira, J. Maza, O. Cabeza, and F. Vidal, *New aspects of the thermopower peak anomaly near the superconducting transition in Y(1)Ba(2)Cu(3)O7-(delta) compounds - thermal fluctuations versus oxygen-content inhomogeneities.* Physica C **253**, 1-15 (1995).

45. Tallon, J.L., C. Bernhard, H. Shaked, R.L. Hitterman, and J.D. Jorgensen, *Generic superconducting phase-behavior in higt -Tc cuprates - Tc variation with hole concentration in YBa2Cu3O7-delta.* Physical Review B **51**, 12911-12914 (1995).

46. Tallon, J.L., J.R. Cooper, P. Desilva, G.V.M. Williams, and J.W. Loram, *Thermoelectric-power - A simple, instructive probe of high-Tc superconductors.* Physical Review Letters **75**, 4114-4117 (1995).

47. Bernhard, C. and J.L. Tallon, *Thermoelectric power of Y1-xCaxBa2Cu3O7-delta: Contributions from CuO2 planes and CuO chains.* Physical Review B **54**, 10201-10209 (1996).

48. Rodriguez, J.E., *YBCO samples as a possible thermoelectric material*, in *Physica Status Solidi C - Conference and Critical Reviews, Vol 2, No 10*, edited by M. Stutzmann. Wiley-V C H Verlag Gmbh: Weinheim. **2**, 3605-3608 (2005).

49. Rodriguez, J.E. and J. Lopez, *Thermoelectric figure of merit of oxygen-deficient YBCO perovskites.* Physica B-Condensed Matter **387**, 143-146 (2007).

50. Ma, H., G.C. Xiong, L. Wang, S.Z. Wang, H. Zhang, L.T. Tong, S.C. Liang, and S.S. Yan, *Thermopower in epitaxial YBa2Cu3O7 thin-films.* Physical Review B **40**, 9374-9377 (1989).

51. Cornejo, I.A., J.U. Trefny, and B. Yarar, *Thermoelecttic-power of YBa2Cu3O7-DELTA superconductive thin-films as a function of oxygen contents.* Journal of Materials Research **8**, 255-260 (1993).

52. Giraldo, J., A. Pulzara, P. Prieto, and M. Chacon, *Thermopower and lattice parameters of YBa2Cu3O7-delta thin films as a function of oxygen content.* Revista Mexicana De Fisica **44**, 202-207 (1998).

53. Jorgensen, J.D., B.W. Veal, A.P. Paulikas, L.J. Nowicki, G.W. Crabtree, H. Claus, and W.K. Kwok, *Structural-properties of oxygen-deficient YBa2Cu3O7-delta.* Physical Review B **41**, 1863-1877 (1990).

54. Liang, R.X., D.A. Bonn, and W.N. Hardy, *Evaluation of CuO2 plane hole doping in YBa2Cu3O6+x single crystals.* Physical Review B **73**, 180505(R) (2006).

55. Ramshaw, B.J., J. Day, B. Vignolle, D. LeBoeuf, P. Dosanjh, C. Proust, L. Taillefer, R.X. Liang, W.N. Hardy, and D.A. Bonn, *Vortex lattice melting and Hc2 in underdoped YBa(2)Cu(3)Oy.* Physical Review B **86**, 174501 (2012).

56. Ando, Y. and K. Segawa, *Magnetoresistance of untwinned YBa2Cu3Oy single crystals in a wide range of doping: Anomalous hole-doping dependence of the coherence length.* Physical Review Letters **88**, 167005 (2002).

57. Chryssikos, G.D., E.I. Kamitsos, J.A. Kapoutsis, A.P. Patsis, V. Psycharis, A. Koufoudakis, C. Mitros, G. Kallias, E. Gamariseale, and D. Niarchos, *X-ray-diffraction and infrared investigation of RBa(2)Cu(3)O(7) and R(0.5)Pr(0.5)Ba(2)Cu(3)O(7) compounds (R=Yand Lanthanides).* Physica C **254**, 44-62 (1995).

58. Fisher, B., J. Genossar, L. Patlagan, and J. Ashkenazi, *Resistivity and Thermoelectric-power measurements of Pr(x)Y(1-x)Ba2Cu3O7-DELTA up to 1200-K and an electronic-structure analysis.* Physical Review B **43**, 2821-2827 (1991).

59. Mori, N., H. Okano, and A. Furuya, *A comparative study of thermoelectric properties in (Pr,Y)Ba2Cu3O7 and PrBa2Cu3O7-Ag percolative systems.* Physica Status Solidi a-Applications and Materials Science **203**, 2828-2831 (2006).

60. Lopezmorales, M.E., D. Riosjara, J. Taguena, R. Escudero, S. Laplaca, A. Bezinge, V.Y. Lee, E.M. Engler, and P.M. Grant, *Role of oxygen in PrBa2Cu3O7-y - Effect on structural and physical-properties.* Physical Review B **41**, 6655-6667 (1990).

61. Blasco, J., J. Garcia, J.M. deTeresa, M.R. Ibarra, P.A. Algarabel, and C. Marquina, *A systematic study of structural, magnetic and electrical properties of (La1-xTbx)(2/3)Ca1/3MnO3 perovskites.* Journal of Physics-Condensed Matter **8**, 7427-7442 (1996).

62. Schiffer, P., A.P. Ramirez, W. Bao, and S.W. Cheong, *Low-temperature magnetoresistance and the magnetic phase-diagram of La1-xCaxMnO3.* Physical Review Letters **75**, 3336-3339 (1995).

63. Jaime, M., P. Lin, S.H. Chun, M.B. Salamon, P. Dorsey, and M. Rubinstein, *Coexistence of localized and itinerant carriers near T_{C} in calcium-doped manganites.* Physical Review B **60**, 1028-1032 (1999).

64. Dagotto, E., T. Hotta, and A. Moreo, *Colossal magnetoresistant materials: The key role of phase separation.* Physics Reports-Review Section of Physics Letters **344**, 1-153 (2001).

65. Jaime, M., M.B. Salamon, K. Pettit, M. Rubinstein, R.E. Treece, J.S. Horwitz, and D.B. Chrisey, *Magnetothermopower in La0.67Ca0.33MnO3 thin films.* Applied Physics Letters **68**, 1576-1578 (1996).

66. Mandal, P., *Temperature and doping dependence of the thermopower in LaMnO3.* Physical Review B **61**, 14675-14680 (2000).

67. He, Q.L., X.T. Zhang, H.S. Hao, and X. Hu, *High-temperature electronic transport properties of La1-xCaxMnO3+delta (0.0 <= x <= 1.0).* Physica B-Condensed Matter **403**, 2867-2871 (2008).

68. Mahendiran, R., S.K. Tiwary, A.K. Raychaudhuri, R. Mahesh, and C.N.R. Rao, *Thermopower and nature of the hole-doped states in LaMnO3 and related systems showing giant magnetoresistance.* Physical Review B **54**, R9604-R9607 (1996).

69. N. F. Mott, E.A.D., *Electronic Processes in Non-Crystalline Materials.* Clarendon Press Oxford, (1971).

70. N. F. Mott, E.A.D., *Conduction in non-crystalline materials* Oxford science publications (1987).

71. Buch, J.J.U., T.K. Pathak, V.K. Lakhani, N.H. Vasoya, and K.B. Modi, *High temperature thermoelectric power study on calcium substituted lanthanum manganites.* Journal of Physics D-Applied Physics **40**, 5306-5312 (2007).

72. R. R. Heikes, R.W.U., *Thermoelectricity Science and Engineering.* Interscience Publishers New York - London, (1961).

73. Sun, J.Z., D.W. Abraham, R.A. Rao, and C.B. Eom, *Thickness-dependent magnetotransport in ultrathin manganite films.* Applied Physics Letters **74**, 3017-3019 (1999).

74. Roy, M., J.F. Mitchell, A.P. Ramirez, and P. Schiffer, *A study of the magnetic and electrical crossover region of La0.5 +/-delta Ca0.5 -/+delta MnO3.* Journal of Physics-Condensed Matter **11**, 4843-4859 (1999).

75. Zhou, H.D., R.K. Zheng, G. Li, S.J. Feng, F. Liu, X.J. Fan, and X.G. Li, *Transport properties of La1-xCaxMnO3 (0.5 <= x < 1).* European Physical Journal B **26**, 467-471 (2002).

76. Habermeier, H.U. and G. Cristiani, *Ferromagnetic superconducting thin films: physics and technological aspects*, in *Superconducting and Related Oxides: Physics and Nanoengineering V*, edited by I. Bozovic and D. Pavuna. Spie-Int Soc Optical Engineering: Bellingham. **4811**, 111-119 (2002).

77. Lin, J.G., S.L. Cheng, C.R. Chang, and D.Y. Xing, *Superconducting and transport properties of YBa2Cu3O7/La0.7Sr0.3MnO3 bilayers.* Journal of Applied Physics **98**, 023910 (2005).

78. Gerdanian, P. and C. Picard, *Seebeck coefficient and electrical-resistivity measurements for semiconducting antferromagnetic YBa2Cu3Ox,up to 1000 K - Evience for phonon drag and strong electron-phonon coupling.* Physica C **246**, 145-155 (1995).

79. Benzi, P., E. Bottizzo, and N. Rizzi, *Oxygen determination from cell dimensions in YBCO superconductors.* Journal of Crystal Growth **269**, 625-629 (2004).

80. Heinze, S., H.U. Habermeier, G. Cristiani, S.B. Canosa, M. Le Tacon, and B. Keimer, *Thermoelectric properties of YBa2Cu3O7-delta-La2/3Ca1/3MnO3 superlattices.* Applied Physics Letters **101**, 131603 (2012).

81. Thomsen, C., R. Liu, M. Bauer, A. Wittlin, L. Genzel, M. Cardona, E. Schonherr, W. Bauhofer, and W. Konig, *Systematic raman and infrared studies of the superconductor YBa2Cu3O7-x as a function of oxygen concentration (o-less-than-or-equal-to-x-less-than-or-equal-to-1).* Solid State Communications **65**, 55-58 (1988).

82. Tsukui, S., M. Adachi, R. Oshima, H. Nakajima, F. Toujou, K. Tsukamoto, and T. Tabata, *Oxygen tracer diffusion in the YBa(2)Cu(3)Oy superconductor.* Physica C **351**, 357-362 (2001).

83. Michaelis, A., E.A. Irene, O. Auciello, and A.R. Krauss, *A study of oxygen diffusion in and out of YBa2Cu3O7-delta thin films.* Journal of Applied Physics **83**, 7736-7743 (1998).

84. Chang, C.L., A. Kleinhammes, W.G. Moulton, and L.R. Testardi, *Symmetry-forbidden laser-induced voltages in YBa2Cu3O7.* Physical Review B **41**, 11564-11567 (1990).

85. Zhang, P.X., U. Sticher, B. Leibold, and H.U. Habermeier, *Thickness dependence of the thermoelectric voltages in YBaCuO7-delta thin films on tilted substrate of SrTiO3.* Physica C **282**, 2551-2552 (1997).

86. Zhang, P.X. and H.U. Habermeier, *Atomic Layer Thermopile Materials: Physics and Application.* Journal of Nanomaterials **2008**, 1-12 (2008).

87. Kwok, H.S. and J.P. Zheng, *Anomalous photovoltaic response in YBa2Cu3O7.* Physical Review B **46**, 3692-3695 (1992).

88. Kleinhammes, A., C.L. Chang, W.G. Moulton, and L.R. Testardi, *Nonbolometric laser-induced voltage signals in YBa2Cu3O7-delta thin-films at room-temperature.* Physical Review B **44**, 2313-2319 (1991).

89. Xiong, X.M., Z.Q. Peng, Y.L. Zhou, Z.H. Cheng, H.B. Lu, H.S. Wang, D.F. Cui, L. Li, and G.Z. Yang, *Dependence of the laser-induced voltages on the oxygen content in normal state YBa2Cu3O7-delta films.* Physica C **280**, 266-268 (1997).

90. Habermeier, H.U., X.H. Li, P.X. Zhang, and B. Leibold, *Anisotropy of thermoelectric properties in La2/3Ca1/3MnO3 thin films studied by laser-induced transient voltages.* Solid State Communications **110**, 473-478 (1999).

91.   Li, X.H., H.U. Habermeier, and P.X. Zhang, *Laser-induced off-diagonal thermoelectric voltage in La1-xCaxMnO3 thin films.* Journal of Magnetism and Magnetic Materials **211**, 232-237 (2000).

92.   Kanno, T., S. Yotsuhashi, A. Sakai, K. Takahashi, and H. Adachi, *Enhancement of transverse thermoelectric power factor in tilted Bi/Cu multilayer.* Applied Physics Letters **94**, 061917 (2009).

93.   Kyarad, A. and H. Lengfellner, *Al-Si multilayers: A synthetic material with large thermoelectric anisotropy.* Applied Physics Letters **85**, 5613-5615 (2004).

94.   Zahner, T., R. Forg, and H. Lengfellner, *Transverse thermoelectric response of a tilted metallic multilayer structure.* Applied Physics Letters **73**, 1364-1366 (1998).

95.   Ding, X., Q.M. Chen, J. Ma, M. Theingi, Y.J. Li, and H. Zhang, *Laser Induced Thermoelectric Voltage Effect of LaNiO3/LaAlO3 Multilayer*, in *Materials for Energy Conversion and Storage*, edited by H. Zhang. Trans Tech Publications Ltd: Stafa-Zurich. **519**, 184-187 (2012).

96.   Turcaud, J.A., K. Morrison, A. Berenov, N.M. Alford, K.G. Sandeman, and L.F. Cohen, *Microstructural control and tuning of thermal conductivity in La0.67Ca0.33MnO3 +/-delta.* Scripta Materialia **68**, 510-513 (2013).

Acknowledgement

This thesis was not possible without the assistance and advice of many people inside and outside this institute. I want to acknowledge the most important ones in the following:

At first Prof. B. Keimer, who gave me the possibility to accomplish my thesis in his group and gave me the freedom to realize my own ideas. I am very thankful for his continuous substantial support during my time at the institute and the critical reading of my thesis.

I also want to acknowledge Prof. E.J. Mittemeijer for acting as second referee for this thesis and Prof. F. Gießelmann for being the head of my promotion committee.

A special thank goes to Hanns-Ulrich Habermeier, the supervisor of my thesis. He welcomed me in the Technology group and highly supported me during my stay at the institute. He always had an open ear for questions of any kind and we had many fruitful discussions. I am also very grateful for the careful reading of this thesis and his helpful comments.

I am very grateful to Michael Schulz from Prof. Keimers group, for his strong support at the PPMS and productive discussions about technical details. I also highly enjoyed our private discussions during my time. From Prof. Keimers group I also want to acknowledge Eva Benckiser and Mathieu Le Tacon from the interesting discussions, Meng Wu and Santiago Blanco-Canosa for the RSM measurements and Nadir Driza and Armin Schulz for the Raman measurements.

I want to thank Giuliano Gregori for his support and the good cooperation in the STO project.

Publication list

Heinze, S., H.U. Habermeier, G. Cristiani, S.B. Canosa, M. Le Tacon, and B. Keimer, *Thermoelectric properties of YBa2Cu3O7-delta-La2/3Ca1/3MnO3 superlattices.* Applied Physics Letters **101**, 131603 (2012)

Gregori, G., S. Heinze, P. Lupetin, H.U. Habermeier, and J. Maier, *Seebeck coefficient and electrical conductivity of mesoscopic nanocrystalline SrTiO3.* Journal of Materials Science **48**, 2790-2796 (2013)
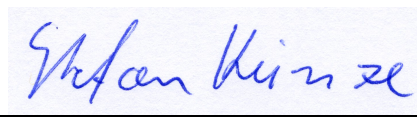
Declaration of Authorship

I hereby certify that the dissertation entitled

"Thermoelectric properties of oxide heterostructures"

is entirely my own work except where otherwise indicated. Passages and ideas from other sources have been clearly indicated.

Esslingen, July 17, 2013

Stefan Heinze